The Role of KIF3B in Cancer Cell Migration and Metastasis

by

Srijan Raha

A thesis submitted in partial fulfillment of the requirements for the degree of

Master of Science

in

Cancer Sciences

Department of Oncology

University of Alberta

Abstract

Metastasis is the leading cause of cancer-related deaths, yet there are no therapies that directly target this process. To identify potential therapeutic targets of metastatic dissemination, we recently completed the first whole human genome shRNA screen using a novel avian embryo intravital imaging platform developed by our group. Nine genes not previously linked to metastasis were identified, including KIF3B, which we determined is required for both *in vivo* cell migration and metastasis of human cancer cells in avian embryo and mouse models.

KIF3B, a member of the kinesin family, is a (+)-end directed microtubule motor that targets the delivery of molecules from the cell interior to the cell periphery. Using an intravital imaging approach, we observed that cancer cells depleted of KIF3B form long cytoplasmic extensions but are unable to productively migrate. We hypothesized that this could be due to loss of key functions in focal adhesions and invadopodia, cellular structures that respectively link the actin cytoskeleton to the extracellular matrix and mediate matrix degradation through enrichment of MT1-MMP. Here we show that KIF3B knockdown by siRNA did not alter the size or number of focal adhesions and did not reduce invadopodia-mediated matrix degradation or extravasation. To increase depletion of KIF3B, we created KIF3B CRISPR knockouts and show that KIF3B is required for motility of human fibrosarcoma (HT1080) cells *in vivo* and is required for the trafficking of MT1-MMP to the cell surface where it is active. Therefore, the lack of a phenotype in our molecular mechanism experiments may have been due to low levels of KIF3B knockdown achieved with siRNA. Additionally, we show that targeting of KIF3B with custom-designed siRNA blocks human epidermoid carcinoma (HEp3) cell motility *in vivo.* Ultimately, continuation of this study may identify the molecular mechanisms of

KIF3B in cancer cell migration and metastasis and lead to the development of specific

anti-metastatic therapies.

Preface

All animals were housed, maintained and treated by procedures approved by University of Alberta Institutional Animal Care and Use Committees (IACUC).

The quantitative *in vivo* whole genome motility screen described in Chapter 1 has been submitted for publication. Srijan Raha was a co-author, validating screen hits *in vivo* and preparing metastatic colony images for Compactness Index analysis. All experiments in Chapter 3 are original work by Srijan Raha.

Dedication

I dedicate my thesis to my parents. My parents have supported me in all my endeavours, in graduate school and in all other areas of my life. I would not have been able to make it through the challenging times without their love and support. Ma & Baba, I cannot thank you enough!

Acknowledgements

I learned more these past three years than I could have ever imagined. There are many people I would like to thank for teaching me experimental techniques, helping me conduct my experiments, and making graduate school a thoroughly enjoyable experience.

First of all, I would like to thank my supervisor Dr. John D. Lewis for letting me choose an exciting and challenging project to work on as a graduate student. Dr. Lewis gave me the independence to develop and test my own hypotheses while always providing helpful feedback when I ran into problems. I will always be grateful for the analytical way of thinking I gained from these experiences. Furthermore, I was always inspired after talking with Dr. Lewis. Through his mentorship I have become confident as a scientist and excited for all the possibilities that lie ahead in translational research.

I would also like to thank my supervisory committee members Dr. Kristi Baker and Dr. Paul Melançon for supporting me through graduate school. Their patience, constructive criticisms, and enthusiasm helped me immensely when I faced obstacles with my project. I am thankful for the unique perspectives they both provided to my project.

I am grateful to the following funding agencies for generously supporting me over the course of my graduate studies: Alberta Cancer Foundation, Building Trades of Alberta Charitable Foundation, Prostate Cancer Canada, Canadian Institutes of Health Research, University of Alberta Faculty of Graduate Studies and Research, Government of Alberta. The work I accomplished would not have been possible without their support.

I will always have fond memories of working in the lab thanks to my colleagues in the Lewis group. Everyone was always willing to help and the unique mix of personalities and training backgrounds made the lab a fun and stimulating place to learn. I want to

Table of Contents

List of Figures

List of Appendices

1 Chapter One – Introduction

1.1 Metastasis

Metastasis is the spread of a primary cancer to a distal site in the body and is responsible for 90% of cancer-related deaths (1). This complex process is comprised of several distinct steps. Cells within the primary tumour that mutate and gain the ability to invade into the local stroma can then intravasate into blood or lymphatic vessels. Cancer cells that survive the shear forces of the circulatory system are then carried to distant sites in the body where they arrest in small vessels. Those cancer cells that extravasate out of the vessels into the parenchyma of distant tissues and proliferate in these new microenvironments give rise to metastases (2). While it is estimated that less than 0.01% of cancer cells that enter the systemic circulation will form into clinically detectable macrometastases (3), metastases that do form can cause patient death by cachexia or by invading into healthy tissues leading to hemorrhaging and organ failure (4).

Metastasis is of special clinical interest because there are currently no therapies available that specifically target this process (5). While many locally confined cancers can be successfully treated with surgical resection and adjuvant chemotherapy or radiotherapy, these treatments ultimately cannot control widely disseminated disease (6). Therefore, there is a great need for therapies that prevent the development of metastases. To date, the development of anti-metastatic therapies has been impeded because the complete set of genes controlling metastasis is unknown. Furthermore, there has been a lack of pre-clinical models that can be used to study the dynamics of the metastatic cascade at high spatio-temporal resolution. To this end, our group has

used the avian embryo to visualize cancer cell motility *in vivo* and to screen for ways to block metastasis.

1.2 The shell-less avian embryo as a model for human cancer cell migration

The shell-less or, *ex-ovo* avian embryo has several traits that make it attractive to use for the study of human cancer cell migration *in vivo* (7). Avian embryos are naturally immunodeficient hosts that accept xenografts of human cancer cell lines. Additionally, they are easily housed and inexpensive compared to murine models. Avian embryos develop normally at 37°C and 60% humidity, requiring minimal user maintenance. A noteworthy trait of the avian embryo is the highly vascularized, transparent chorioallantoic membrane (CAM), an extra-embryonic tissue within the eggshell that facilitates gas exchange for the developing embryo. The CAM is a thin structure that is 100μm across its three layers (8). The uppermost layer, the ectoderm, is a one- or two-cell epithelial layer. By developmental day 10 the ectoderm capillary plexus is fully developed, which is a network of capillaries that connects the arterial and venous blood vessels. The mesoderm layer below the ectoderm contains stromal cells, collagen fibers, capillaries and blood vessels of larger diameter. The lowermost endoderm is a one-cell layer that borders the allantoic cavity. The ectoderm capillary plexus is one of the most important attributes of the avian embryo as it supports the grafting of cancer tissues for the study of angiogenesis and metastasis (8). Removal of the embryo from its shell on development day 4 and culturing in sterilized containers provides vastly improved access to the CAM for experimental manipulation (9).

1.2.1 Spontaneous and experimental models of metastasis using the avian embryo

Spontaneous metastasis refers to the ability of cancer cells to disseminate from an established tumour and is commonly initiated by injection of cancer cells into the organ type the cancer originated from (orthotopic injection) (10). In comparison, experimental metastasis refers to the intravenous injection of cancer cells into the systemic circulation (11). In the spontaneous metastasis model, cancer cells must complete all steps of the metastatic cascade in order to reach a distant site in the model organism. Conversely, experimental metastasis bypasses the early metastasis steps including local invasion and intravasation. Therefore, this must be taken into consideration when selecting a metastasis assay. Spontaneous metastasis assays inherently select for those cancer cells that are able to escape the primary tumour to reach distant sites (11) but may be limited by the length of time required for metastases to form. The animal may succumb to the primary tumour before significant metastases form (12) . Experimental metastasis assays on the other hand progress rapidly and allow the user to control the type and number of cancer cells that enter the circulation (11).

Using the avian embryo, spontaneous metastasis can be assayed by topical application of cancer cells to the ectoderm or by direct injection of cells into the mesoderm, forming a bolus (8). Experimental metastasis is assayed by intravenous injection of cancer cells into the capillary plexus of the CAM ectoderm. Owing to the thin and transparent nature of the CAM, fluorescently-labelled cancer cells can be imaged non-invasively in live embryos (intravital imaging). In the experimental metastasis assay, cancer cells are injected into the CAM of developmental day 10 avian embryos where the cells rapidly arrest and extravasate into the stroma as single cells. Within 5 days, these single cancer cells proliferate into diffuse colonies (50 to 100 cells) as the daughter cells migrate away

from the parent cell. The impact of pharmacological agents or genetic manipulations on the behavior of highly motile cancer cells can be readily captured using intravital fluorescence microscopy (7, 13-22).

1.2.2   Compact colony phenotype in avian embryo CAM predicts inhibition of spontaneous metastasis

The tetraspanin CD151 had previously been demonstrated to be required for spontaneous metastasis of the HEp3 human epidermoid carcinoma cell line in avian embryos (23). In this study, intravenous injection of the anti-CD151 monoclonal antibody 1A5 into avian embryos blocked spontaneous metastasis out of the primary tumour by an undefined mechanism. Extending this study, our group showed in an avian embryo experimental metastasis assay that intravenous injection of monoclonal antibody 1A5 failed to block tumor cell arrest and extravasation into the stroma. However, 1A5 injection blocked subsequent migration of HEp3 and HT1080 cells within the stroma, forming a cluster of cells or a 'compact colony' phenotype. Furthermore, it was found in the avian embryo spontaneous metastasis assay that monoclonal antibody 1A5 blocks intravasation and subsequent metastasis by blocking the ability of HEp3 tumor cells to detach at the rear of the cell body. Treatment with intravenous 1A5 also inhibited spontaneous metastasis of HEp3 cells in a SCID mouse model. Taken together, this showed that the compact colony phenotype in the CAM predicts an inhibition of spontaneous metastasis. The same mechanisms that blocked cell motility in the upper CAM also blocked spontaneous metastasis in avian embryos and mice (24). Based on these findings, our group hypothesized that we can use the shell-less avian embryo model to screen for genes that are required for *in vivo* cancer cell motility and spontaneous metastasis.

1.3 Quantitative *in vivo* whole genome motility screen reveals novel targets to block cancer metastasis

Recently our group completed the first *in vivo* whole human genome shRNA screen to identify potential therapeutic targets of metastatic dissemination. Briefly, the highly metastatic HEp3 human epidermoid carcinoma cell line was infected with a GIPZ microRNA-adapted shRNA lentiviral library (Open Biosystems). shRNAs in this library are based on the native miR-30 primary transcript to enable processing by the endogenous RNAi pathway while minimizing cellular toxicity. This library encodes 79,805 sequenced-verified shRNAs targeting 30,728 human genes along with TurboGFP to verify successful expression of shRNAs. HEp3 cells were transduced at low multiplicity of infection (0.2) to favour integration of a single shRNA per cell according to Poisson distribution. After intravenous injection into the CAM, fluorescently-labelled cancer cells arrest and extravasate to form metastatic colonies. Approximately 10% of injected cells are visible and accessible in the upper CAM. Injection of low cell numbers (25,000) ensures that well isolated colonies can be extracted from the upper CAM (Figure 1-1A). To ensure three times coverage of all 79,805 shRNA clones with 99% confidence, 100 embryos were required for the screen. Transduced GFP-expressing cells were injected into *ex ovo* embryos on developmental day 10. At this developmental time point the sub-endothelial basement membrane has not formed fully and thus intravenously injected cells readily extravasate out of the CAM capillary plexus. On developmental day 15, more than 200,000 metastatic colonies in the CAMs of the 100 embryos were examined using intravital fluorescent microscopy. 67 morphologically compact colonies ('hits') were identified, excised, dissociated and cultured under puromycin selection. 50 clones were successfully expanded in culture.
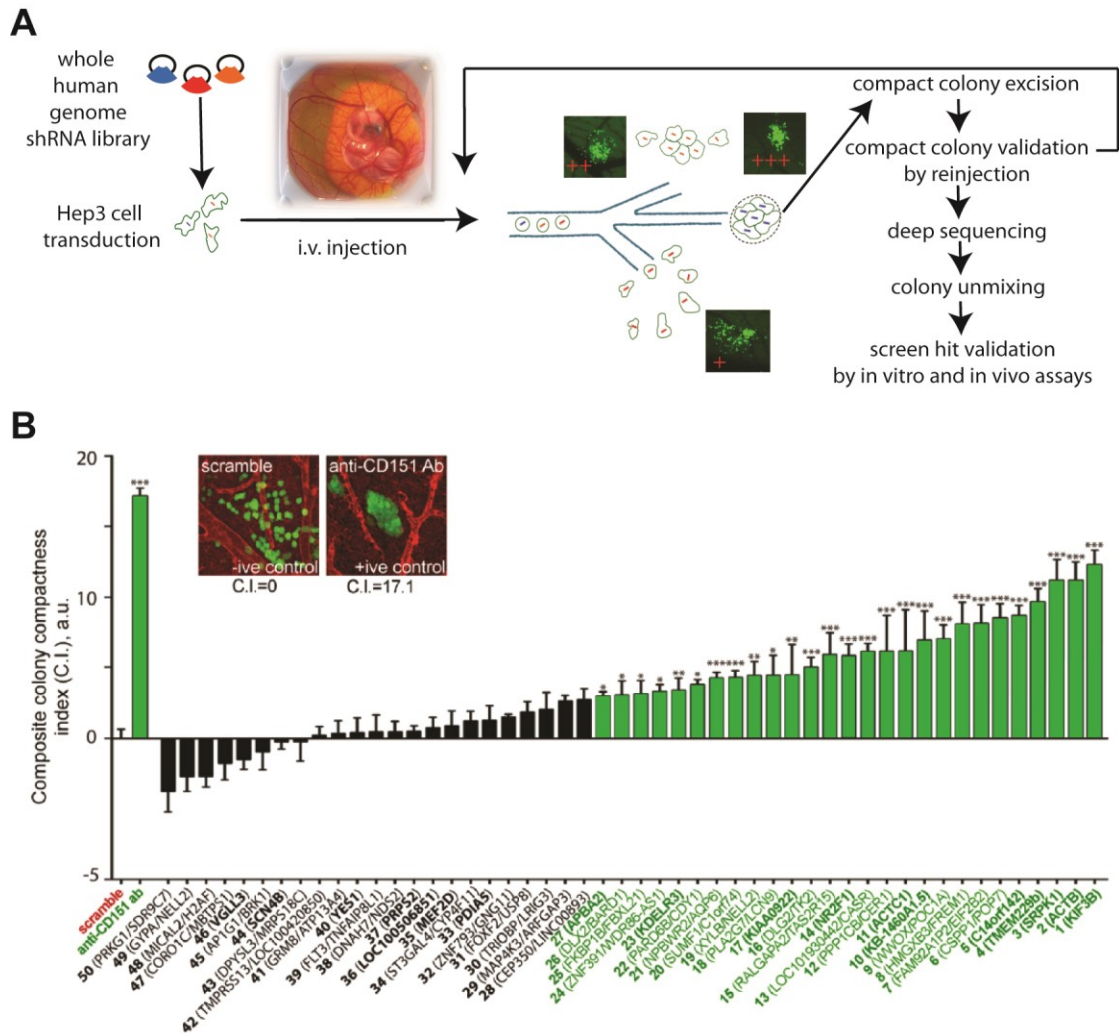
Figure 1-1. Quantitative *in vivo* whole genome screen for genes that are required for cancer cell motility.

(A) Overview of screen. (B) Composite compactness index (C.I.) distribution of screen hits relative to positive (anti-CD151) and negative (scramble shRNA) controls. Screen hits that are significantly more compact than negative control are indicated in green. Clones containing a single shRNA species are in bold. For clones containing multiple shRNAs, the two most predominant shRNAs are shown. Statistical significance was determined using one-way ANOVA with Fisher's LSD test (* $p<0.05$, ** $p<0.01$, *** $p<0.001$).

To identify the genes whose shRNA knockdown produced a compact colony phenotype, genomic DNA was purified from all compact clones. shRNA-encoding DNA inserts were then amplified by PCR using common flanking primers and the resultant DNA sequences were determined by Illumina deep sequencing. The DNA sequences were then subjected to human nucleotide BLAST analysis and ranked according to abundance within each clone. We found that single shRNAs were present in 17 of the 50 clones while more than one shRNA was present in the remaining 33 clones. All clones that were successfully expanded *in vitro* were validated using an experimental metastasis approach. Clones were intravenously injected into shell-less avian embryos and the resulting metastatic colonies were imaged using fluorescent microscopy.

1.3.1 Compactness index (C.I.) to quantify inhibition of cell motility and rank gene targets from screen

The degree of colony compactness produced by screen hits was used as a readout for their impact on cancer cell motility *in vivo.* While we did not observed significant differences in the rate of proliferation from clones *in vitro,* we observed that several clones grew at different rates *in vivo.* Therefore, to account for differences in *in vivo* proliferation rate between individual colonies and to get an accurate assessment of *in vivo* cancer cell motility, we developed a custom MATLAB based program to analyze the compactness of each individual metastatic colony. The program uses three algorithms to analyze distinct parameters of each individual colony (Appendix A). The first algorithm (linear index) quantifies the remoteness of cancer cells from the colony centroid. Briefly, this algorithm creates a mask using fluorescence to demarcate the cancer cells and produces a 360º line scan around the centroid to build an average line plot fitted to a Gaussian distribution. The standard deviation in Gaussian radial line-scan intensity

distribution between screen hit colonies and control shRNA colonies is used to generate the linear index. The second and third algorithms use the fluorescence mask to measure the area of individual colonies (area index) and calculate the density of cells within the colonies (density index). A minimum of 10 individual colonies were analyzed per clone then the clones were ranked. While each index produced a similar ranking of the clones identified in the screen, each method misidentified a number of visually compact clones when used alone. For this reason, the three algorithms were combined to create a composite colony compactness index (C.I.). The hits were stratified and compared to the anti-CD151 antibody-treated positive control and scrambled shRNA negative control. The C.I. was calculated from the Z-scores ($\frac{experimental-\overline{control}}{SD\ control}$) for each index where

$$C.I. = Z_{density\ index} - Z_{linear\ index} - Z_{area\ index} .$$

Statistical testing revealed 27 clones whose compactness index differed significantly ($p \leq 0.05$) from that of the negative control. 11 of these 27 clones contained single shRNAs (KIF3B, ACTB, SRPK1, TMEM229B, C14orf142, KB-1460A1.5, ACTC1, NR2F1, KIAA0922, KDELR3 and APBA2) (Figure 1-1B). From these analyses it was revealed that KIF3B was our top screen hit. Out of all the hits, knockdown of KIF3B produced the most potent inhibition of cancer cell motility *in vivo*.

1.3.2 Characterization of KIF3B as a driver of metastasis

To determine if the compact colony phenotype observed in the screen clone was due to specific depletion of KIF3B and not an off-target effect of lentiviral transduction, a new HEp3 stable KIF3B knockdown cell line was created using an independent shRNA. The newly created cell line was then validated using the avian embryo metastatic colony

formation assay. The CI value for the new clone was similar to that of the original screen clone.

To further study the cellular mechanisms that produced the compact colony phenotype in KIF3B knockdown cells, our group performed high-resolution *in vivo* timelapse imaging of individual metastatic colonies and the invasive front of primary tumors derived from HEp3 shControl or shKIF3B cells (Figure 1-2A). We observed that KIF3B knockdown significantly reduced speed and productive migration in metastatic colonies. In contrast, while there was no significant reduction in the average speed of shKIF3B cells at the invasive front of the primary tumour, productive migration was reduced by greater than 75%. This correlates well with the significant reduction in the number of invasive cancer cells in the invasive zone surrounding shKIF3B primary tumours compared to shControl tumours. Individual HEp3 shControl cells at the invasive tumour front tended to form a single dominant protrusion in the direction of motility while shKIF3B cells formed multiple uncoordinated protrusions extending in all directions. This suggests that KIF3B is required for direction cell migration *in vivo.*

To test the hypothesis that genes required for cancer cell motility in the avian embryo CAM are also required for spontaneous metastasis, we evaluated the KIF3B clones in a xenograft murine model of human cancer metastasis (Figure 1-2B). HEp3 shControl or shKIF3B cells were subcutaneously injected into the flank of nude mice and the mice were sacrificed when the primary tumours reached 1500mm^3. The lungs were then examined for the presence of metastases using whole mount fluorescent microscopy. By fluorescence microscopy, metastatic lesions to the lungs were readily observed in animals bearing shControl tumours whereas metastatic lesions were rarely observed in animals bearing shKIF3B tumours. Next the metastatic burden of human cancer cells in the mouse lungs was quantified using human-specific *alu* qPCR and compared to a

standard curve generated from HEp3 cells (25). Mice bearing shControl tumours had an average of 2.4 million disseminated HEp3 cells per lung. In contrast, animals bearing KIF3Bsh1/sh2 tumours had a 99.55% and 99.67% reduction in tumour burden. There was no significant difference in weight of primary tumors of the different groups at the time of sacrifice. These results confirm our hypothesis that genes required for *in vivo* cancer cell motility are also required for spontaneous metastasis and that KIF3B is a promising target to block metastasis.

Next we examined patient datasets to determine the relevance of KIF3B to human cancer progression and metastasis. Using the Oncomine gene expression database, we found that KIF3B is significantly upregulated in metastases compared to primary tumours in patient-matched samples of melanoma, prostate cancer, and head and neck cancer (Figure 1-2C). Furthermore, a survey by a pathologist of immunohistochemical staining of melanoma and head and neck cancers indicates that KIF3B is significantly upregulated in the invasive zone of the primary tumours of these cancers.

Overall, we found that the compact colony phenotype in the avian embryo CAM that resulted from inhibition of HEp3 motility correlated with the inhibition of spontaneous metastasis in the mouse xenograft model. Furthermore, our survey of patient datasets and tumour samples indicates that KIF3B is involved in the metastasis of several human cancers.

Our next step was to determine the mechanism(s) by which KIF3B controls cancer cell migration and metastasis. To determine if the role of KIF3B can be studied *in vitro*, we asked if KIF3B is required for cell migration *in vitro.* Using the magnetically attachable stencil assay, cells were seeded around a magnetic stencil and allowed to form a monolayer overnight (26). The stencil was then removed, leaving a void. Cells were

allowed to migrate for 12 to 16 hours into the void. Cell migration was calculated as percent closure of the initial void. It was found that KIF3B knockdown reduced the void closure in HEp3, PC3, and MDA-MB-231 cancer cell lines (Figure 1-2D).
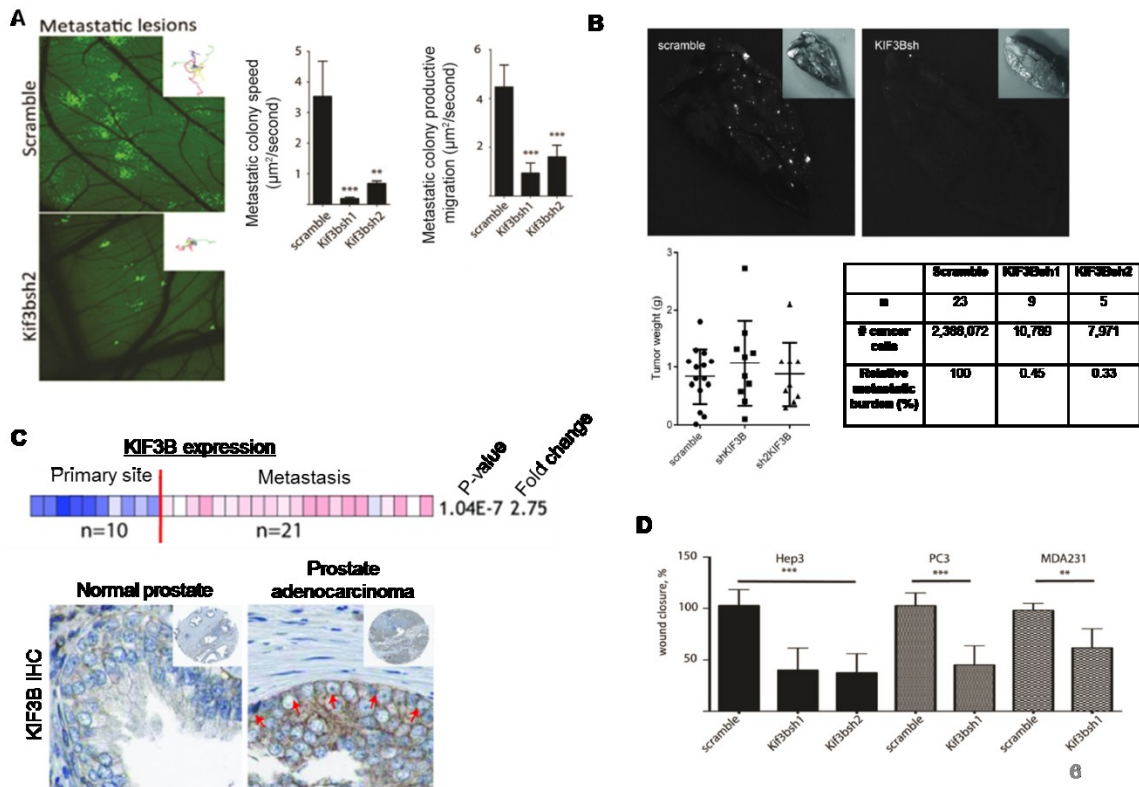
Figure 1-2. Characterization of KIF3B as a driver of metastasis
(A) Intravital imaging of cancer cells in metastatic colonies and primary tumors over 7 or more hours. (B) Fluorescence stereomicroscopic images of lungs from mice bearing subcutaneous tumors derived from HEp3 cancer cells and quantification of HEp3 cancer cells metastasized to lung as determined by human alu q-PCR. (C) Upper panel: KIF3B expression is significantly elevated in bone metastases compared to primary prostate tumours in patient-matched samples. CodeLink mRNA Bioarray, Chandran dataset (Oncomine). Lower panel: KIF3B expression is significantly upregulated in the invasive zone of primary prostate tumours compared to normal prostate tissue (The Human Protein Atlas). (D) MAtS (magnetically attachable stencils) *in vitro* migration assay of control and KIF3Bsh/sh2 cell lines. Data from panels A and D are representative of three independent experiments. **p<0.01, ***p<0.001, one way ANOVA of mean±SEM and Fisher's LSD test.

1.4 Intracellular transport by microtubule motor proteins

1.4.1 Microtubule structure and formation

Eukaryotic cells compartmentalize cellular functions into organelles to increase efficiency of reactions while isolating harmful compounds from the rest of the cell (27). As a result of compartmentalization, an active intracellular transport network (as opposed to passive diffusion) is required for the targeted delivery of membrane bound vesicles to distant locations in the cell (28). The microtubule network and associated motor proteins mediate this intracellular vesicle transport as well as several key cellular processes including mitosis, positioning of membranous organelles, and determination of cell shape and motility (29).

The basic unit of the microtubule is the α/β-tubulin heterodimer. As the dimers polymerize end-to-end into a linear protofilament, the parallel association of 13 protofilaments leads to the formation of a hollow microtubule (30). Microtubules are highly dynamic and can rapidly switch between phases of growth and shrinkage in a process known as dynamic instability (31). Dynamic instability significantly reduces the amount of time required to find a target, such as a chromosome during mitosis and allows the microtubule network to quickly adapt to changes in the environment (32, 33). Furthermore, microtubules are considered polar because their ends differ chemically and structurally (34). α-tubulin is exposed on the minus end of the microtubule while β-tubulin is exposed on the plus end. This polarity is significant because faster microtubule growth occurs at the plus end (30).

Microtubules are nucleated from structures called microtubule organizing centres (MTOCs) which are the centrosome in animal cells and the spindle pole body in yeast (35). Centrosomes are typically composed of two cylindrical centrioles that are oriented

perpendicular to each other. While it has been observed that the mitotic spindle composed of tubulin can form in eukaryotes that lack centrioles (36), it has been shown that the centrosomal protein γ-tubulin is required for microtubule nucleation (37). Specifically, γ-tubulin and associated proteins that form the γ-tubulin ring complex (γTuRC) cap the minus end of microtubules, preventing depolymerisation and thereby stabilizing microtubules.

1.4.2 Microtubule motor proteins

<u>**Kinesin superfamily**</u>

Kinesins and dyneins are the two types of microtubule motors responsible for long-range transport in many cell types. Kinesins generally move cargo toward the microtubule plus-end, from the cell interior to the cell periphery. In contrast, dyneins generally move cargo toward the microtubule minus-end, from the cell periphery to the cell interior (38). Currently, 45 mammalian kinesin superfamily (KIF) genes have been identified and grouped into 15 families on the basis of homology between the motor domains (39). The kinesin families can be further grouped into N-kinesins, M-kinesins, and C-kinesins based on the position of the motor domain at the N-terminus, middle, or C-terminus of the protein, respectively. N-kinesins transport cargo to microtubule plus-ends, C-kinesins transport cargo to microtubule minus-ends, and M-kinesins depolymerize microtubules (40). All kinesins have a coiled-coil domain that facilitates dimerization between motor subunits. The motor domain in each motor subunit has a binding site for microtubules and a catalytic site for ATP hydrolysis (41, 42).

Kinesin movement along microtubules is processive and requires ATP

Kinesins move processively, meaning they can take several consecutive steps along microtubules without dissociating (43). This processive movement requires coordination between the two motor subunits. ATP hydrolysis in the motor domain of the trailing motor subunit causes it to detach from and walk forward along the microtubule while the other motor subunit remains bound to the microtubule. ATP is then hydrolyzed in the motor domain of the new trailing motor subunit and the cycle continues (44). After energy is released from ATP hydrolysis, movement towards the microtubule plus-end is specified by the conformational change that occurs in a small region of the motor domain called the neck (43).

Cargo binding and regulation of release

The motor subunits of kinesins may bind to their cargo directly, have an adaptor protein bind to the cargo, or require large scaffolding complexes to bind to the cargo (45). When cargoes arrive at their destination, they must be released from the kinesin. Phosphorylation, calcium signalling, and small G proteins regulate cargo unloading. Phosphorylation of motor subunits or the adaptor proteins of kinesins has been shown to regulate unloading of cargo in KIF5 and KIF17 respectively (45). KIF5 transports mitochondria through interaction with the Milton-Miro complex. Upon encountering areas of the cell with high regional calcium, Milton-Miro inhibits KIF5 motor activity (46). In the case of KIF1 that transports Rab3-postitive vesicles, the inactivation of Rab3 by GTPase activating proteins (GAPs) leads KIF1 to release its vesicles (47). Finally, when kinesins like KIF5 are not bound to cargo, they can exist in a folded auto-inhibitory state (48).

Unanswered questions about cargo transport by microtubule motors

It has been recognized that kinesins and dyneins can bind to the same vesicle (49). However, the complete mechanisms that control the direction the vesicle is ultimately transported are still unknown. Some motors transport multiple different cargos. How a single motor prioritizes which cargo to bind and how to subsequently switch to binding a different cargo is still unclear (45). Additionally, it is unknown how far a single motor can transport its cargo *in vivo* and whether multiple motors take turns transporting the cargo to its final destination (45). Quick-freeze deep-etch electron microscopy of organelles transported by motors bound to axons, and biophysical data suggest that multiple motors may simultaneously transport a single vesicle, achieving greater transport speeds possible than with a single motor (45, 50). The fate of kinesins after traveling long distances was until recently unknown. Blasius et al. showed that KIF5 (conventional kinesin, also known as kinesin-1) is not degraded at nerve terminals after transport along axons, is not transported back to the cell body by retrograde motors, but can diffuse back to the cell body (51). The fate of other kinesins after delivering their cargo and how they re-associate with microtubules is currently undefined.

1.4.3   Kinesin KIF3B mediates diverse cellular functions

Nomenclature

The description of kinesin families and specific family members was confusing in the early literature as several naming schemes were used. A standardized kinesin nomenclature was thus put forward in 2004 to reduce further confusion (52). Families bear the name *kinesin* while individual motors within the family are represented by the gene name *KIF* and Arabic numerals. The kinesin-2 family consists of the motors KIF3

and KIF17. KIF17 is a homodimer that directly binds to cargo through its C-terminal domain (53). The KIF3 motor is a heterotrimer consisting of two motor subunits (KIF3A, KIF3B or KIF3C) and an adapter protein. Only KIF3A/B and KIF3A/C have been observed to dimerize (54). In the literature, KIF3 typically refers to a kinesin composed of the KIF3A/B motor subunits.

Known functions of KIF3B

Kinesin superfamily member 3B (KIF3B) was first described by Nobutaka Hirokawa and his group in 1995. They showed that KIF3B is a plus-end directed microtubule motor that targets the delivery of molecules from the cell interior to the cell periphery (55). Specifically, KIF3B is part of the KIF3 motor complex, a heterotrimer composed of the two motor subunits KIF3A and KIF3B, and the adaptor protein KAP3 (kinesin-associated protein 3) (39). KIF3A and KIF3B exhibit opposite charge in a small segment of the coiled coil domain, facilitating their dimerization (39). KAP3, also known as KIFAP3 and SMAP, binds to the tail domain of KIF3A/3B, linking the motor subunits of KIF3 to their cargo (56-58). Specifically, the positively charged grooves in KAP3's 9 Armadillo repeats mediate electrostatic interactions with KIF3A/3B and cargo (41, 59).

As of March 2017, the PubMed search engine returns 245 entries on KIF3A, 72 entries on KIF3B and 29 entries on KIF3C. However, only a handful of these studies have investigated the molecular mechanisms of these proteins in normal cell physiology. KIF3A/B has been shown to be involved in a wide range of processes including mitosis, endosomal trafficking, maintenance and assembly of cilia, and left-right determination. A biophysical study in a cell-free system has shown that KIF3A mediates the processivity of the KIF3 motor while KIF3B mediates its speed (60).

KIF3A homolog FLA10 has been reported to localize near centrosomes and the mitotic

spindle during mitosis in *Chlamydomonas* and the KIF3 homolog kinesin II has been

observed at the mitotic apparatus of dividing sea urchin embryos (61, 62). Based on this

information, Haraguchi et al. explored the role of the KIF3 motor in mitosis of human cell

lines. Creating a C-terminal mutant of KIF3B that is unable to bind to KAP3 but is still

able to associate with KIF3A, they found that rates of aneuploidy was three times higher

in HeLa cells expressing mutant KIF3B. This suggested KIF3B is required for proper

segregation of daughter chromosomes during mitosis (63).

Extracellular materials, ligands and plasma membrane proteins and lipids are

internalized by endocytosis. Much of the endocytosed proteins and lipids are returned

back to the plasma membrane through endosomal recycling (64). Endocytic recycling is

an important mechanism for regulating levels of cell surface proteins in response to

extracellular stimuli (e.g. increased cell surface localization of glucose transporters in

response to insulin) (65). The balance of endosomal update and recycling is critical to

diverse cellular processes including nutrient uptake, signal transduction, cell adhesion,

cell polarity, and cell migration (64). The findings from several studies have now shown

that KIF3 transports cargo between several components of the endosomal pathway (see

(66) for a depiction of the endosome-lysosome system). Imamura et al. showed that

KIF3 physically interacts with Rab4 for the transport of GLUT4 glucose transporter to

early endosomes in response to insulin (67). Rab GTPases regulate distinct steps in

membrane trafficking including vesicle formation, actin- and tubulin-dependent vesicle

movement, and membrane fusion (68). In a later study Brown et al. demonstrated that

KIF3A interacts with Rab7, a marker for late endosomes and that KIF3A is required for

proper distribution of lysosomes and late endosomes (69). Most recently, Schonteich et

al. showed KIF3B interacts with Rip11 (a Rab11-binding protein) and directs

endocytosed proteins to recycling endosomes (70). Counterintuitively, KIF3 was also shown to be required for plus-end directed *retrograde* transport from the Golgi to the endoplasmic reticulum (ER). Stauber et al. showed that the knockdown of KIF3A or KAP3 leads to fragmentation of the Golgi, an organelle that feeds into the endosome system. The knockdown of KIF3A or KAP3 also altered the distribution of the KDEL receptor that retrieves soluble cargo from the Golgi and returns it to the ER (71).

Cilia and flagella are specialized structures composed of microtubule bundles and are present in many tissue types. Their functions include generation of cell motility, fluid flow and mechanochemical sensation (41). Ciliary precursors are transported on microtubules from the base of the cilia to the distal tip where they are incorporated. By observing the movement of fluorescently labelled motors and ciliary cargo in *Caenorhabditis elegans,* it was determined that the homologs of kinesin-2 family microtubule motors KIF3 and KIF17 are required for the maintenance and assembly of cilia (72). Similarly, from studies in *Chlamydomonas reinhardtii* it was postulated that KIF3 motors are required for assembly and maintenance of flagella in all eukaryotic cells (73). To study the role of KIF3B in embryonic development and its role in cilia in a complex *in vivo* environment, Nonaka et al. generated homozygous KIF3B knockout mice (74). The KIF3B knockout embryos exhibited morphological abnormalities including randomized left-right asymmetry, pericardial sac ballooning, and growth retardation. All KIF3B knockout mice subsequently died mid-gestation. Focusing on the left-right asymmetry, the authors observed that the KIF3B knockout mice lost nodal cilia, resulting in loss of leftward flow of extraembryonic fluid at the node. The node is a transient structure that forms during gastrulation and is important for left-right determination (74). Notably, 16 out of 46 knockout mice had reversed heart L loops which was a result of the loss of 'nodal flow'. Left-right asymmetry is present throughout the normal body. For

example, the heart is offset to the left of the body. In humans, patients with Kartagener's syndrome have their organs in the reversed orientation due to a genetic defect (75). These patients have immotile sperm and defective airway cilia. Thus, cilia have been suggested to control left-right asymmetry in humans. The potential role for KIF3B in Kartagener's syndrome has yet to be investigated.

To date, no study has explored the direct role of KIF3B in cancer cell migration, invasion and metastasis. In the following sections I will introduce cellular structures (focal adhesions, invadopodia) that I hypothesize KIF3B regulates and describe the feasibility of therapeutically targeting KIF3B with RNA interference to block metastasis.

1.5 Mechanisms of cancer cell migration

1.5.1 Protease-dependent and protease-independent modes of cancer cell migration

Active cell migration is an evolutionarily conserved mechanism that is critical to several physiological processes (76). Cells must reorganize into the different germ layers during gastrulation, and migrate to sites of inflammation during wound healing and immune responses (77-79). Perplexingly, cancer cells spread within tissues using similar if not identical mechanisms as non-neoplastic cells (80).

Individual cancer cells can migrate using protease-dependent (mesenchymal) or protease-independent (amoeboid) mechanisms (80). Epithelial cells that become mutated can undergo a reversible epithelial-mesenchymal transition to gain the properties of mesenchymal cells. In this process, polarized epithelial cells that normally grow in clusters lose their cell to cell junctions while retaining adhesive molecules such as integrins and upregulating pro-invasive molecules such as MT1-MMP (81, 82). Cells that have undergone EMT have a spindle, fibroblast-like morphology and are highly motile (83). Cancer cells using a mesenchymal mode of migration use matrix metalloproteases to degrade barriers such as the basement membrane faced by cells invading out of a primary tumour (84). In contrast, cancer cells using an amoeboid mode of migration are highly deformable and can bypass ECM barriers by changing shape and squeezing through gaps in the ECM (80). The amoeboid mode of migration was first studied in the single cell amoeba *Dictyostelium discoideum.* This mode of migration is characterized by low adhesion (low integrin expression) and lack of focalized proteolytic activity (80). Amoeboid cells have a rounded or elliptical morphology and can migrate up to 20 times faster than mesenchymal cells (20µm/min versus 1µm/min) (80).

Cancer cells can switch between mesenchymal and amoeboid modes of migration by changing gene expression through mesenchymal–amoeboid transition (MAT) or amoeboid–mesenchymal transition (AMT) (85). The mode of migration used by cancer cells is likely a product of the microenvironment. For example, mesenchymal HT1080 and MDA-MB-231 cells that were treated with a protease inhibitor cocktail and embedded in a 3D matrix adopted amoeboid migration as a compensatory mechanism (86). In a later study, Sabeh et al. demonstrated that HT1080 cells require matrix metalloproteases (specifically MT1-MMP) to invade out of a highly cross-linked type I collagen matrix analogous to the tissue interstitium present in several locations in the body (87). Since MT1-MMP has been shown in several reports to be required for invasion through basement membranes *in vivo* (such as that of the avian embyo CAM), the discussion hereafter will focus on the mesenchymal mode of migration (82).

Steps in mesenchymal (protease-dependent) cell migration

The mesenchymal mode of cancer cell migration can be conceptualized as a five step cycle (80). 1) Initial protrusion of the cell at its leading edge is driven by actin polymerization and assembly into actin filaments. 2) Growing cell protrusions contact underlying extracellular matrix (ECM) using cell adhesion molecules, predominantly with integrin-mediated structures called focal adhesions. 3) The adhesion to the ECM using integrins leads to the recruitment of proteases that degrade the barrier posed by the ECM. 4) Contraction of actin filaments by myosin II propels the cell forward into the gap in the degraded ECM. 5) Cell-ECM adhesions disassemble at the trailing edge of the cell, enabling the whole cell to move forward relative to its initial position. The cycle can then repeat. Underlying this cycle are two distinct components of mesenchymal cell motility. First, to migrate cells must be able to remodel their actin cytoskeleton. Second, to bypass tissue barriers cells must be able to degrade ECM. These two processes are

respectively mediated by cell structures called focal adhesions and invadopodia which are discussed below.

1.5.2 Structure and function of focal adhesions

While cells express various cell surface adhesion receptors (including integrins, syndecans and other proteoglycans, cadherins, and cell adhesion molecules (CAMs)), the best studied family of receptors in cell migration are the integrins (88). Integrins are transmembrane heterodimers formed from one α subunit and one β subunit. A total of 24 integrins are known to form from combinations of eighteen α subunits and eight β subunits (88). Individual integrins recognize multiple ligands in the extracellular milieu such as fibronectin, laminin and collagen (89).

Focal adhesions are integrin-mediated multi-protein structures that link the extracellular matrix to the actin cytoskeleton (90). Traction forces generated at focal adhesions are transmitted to the ECM, and are used by the cell to pull itself forward after the initial cell protrusion has formed (91). Focal adhesion assembly begins at the leading edge of the cell when integrins bind to their extracellular ligands (Figure 1-3a) (91). This induces a conformational change in integrins that exposes their cytoplasmic tail, promoting linkage to the actin cytoskeleton through multiprotein complexes (Figure 1-3b). Actin polymerization at focal adhesions leads to formation of actin stress fibers that extend to the rear of the cell (92). Myosin II contracts actin stress fibres, moving antiparallel actin filaments past each other (91). Contraction of stress fibres pulls on the cell rear and moves the cell forward while promoting disassembly of focal adhesions at the cell rear (93).
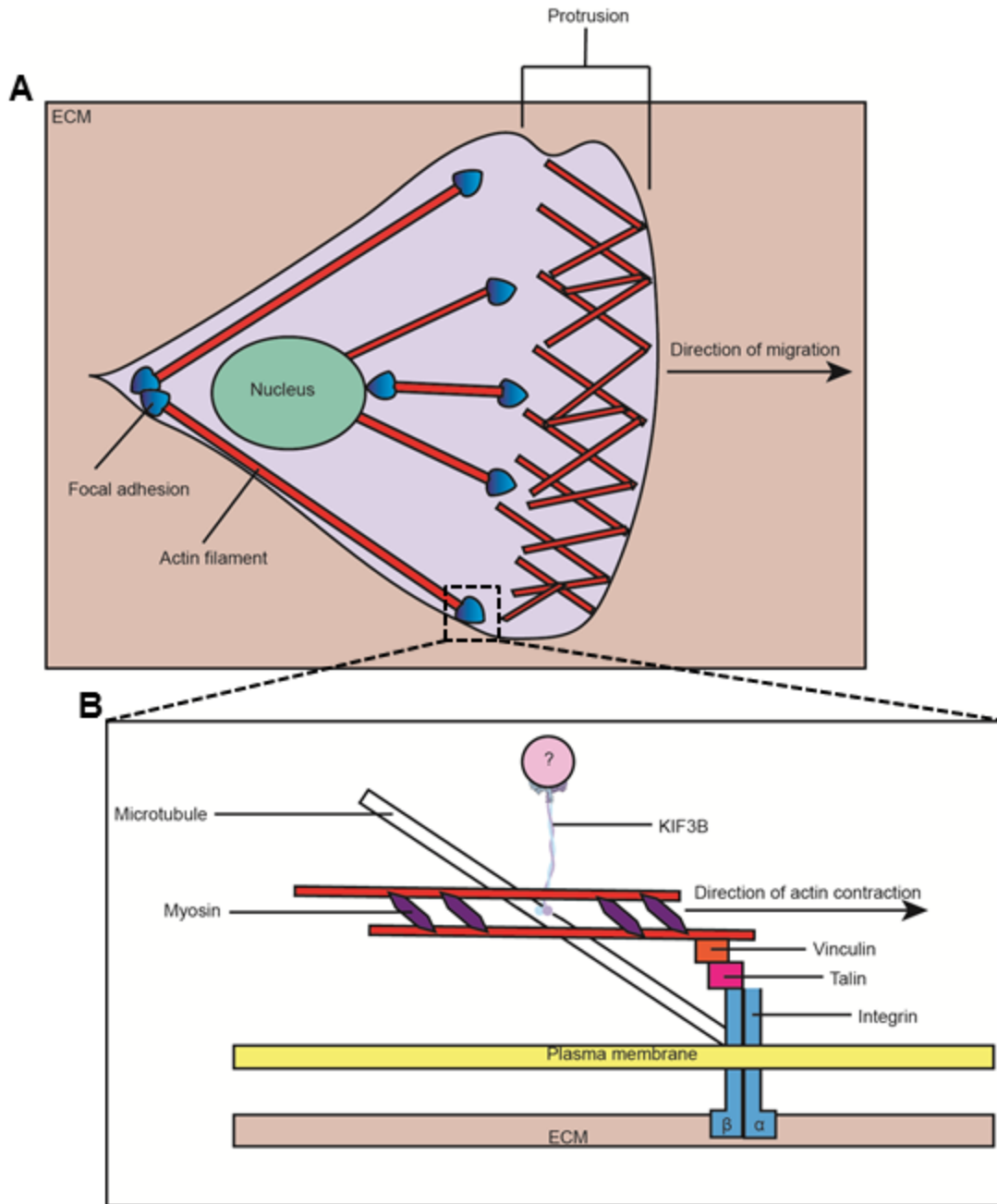
Figure 1-3. Structure and function of focal adhesions
(A) Focal adhesions are assembled at the leading edge of the cell behind the initial cell protrusion and are disassembled at the cell rear. (B) Focal adhesions are integrin-mediated multi-protein complexes that link the extracellular matrix to the actin cytoskeleton. Traction forces generated at focal adhesions coupled with actomyosin contraction pull the cell forward.

The nature of focal adhesions depends on the cell type and composition and mechanical properties of the underlying ECM (91). Round amoeboid cells (lymphocytes, cancer cells in some environments) on one extreme use few or no focal adhesions while highly spread mesenchymal cells (fibroblasts, transformed endothelial cells) on the other extreme have many large adhesions. For cells grown in culture, larger and more stable focal adhesions form from higher concentrations of underlying ECM or stiffer substrates. These conditions respectively increase availability of ligands for integrin-binding and focal adhesion formation, and enhance cytoskeletal contraction. Furthermore, the relation between size of focal adhesions and speed of migration follows a normal distribution (94). In mouse embryonic fibroblasts and HT1080 cells, cells with median sized focal adhesions moved the fastest in 2D culture. Cells with very large focal adhesions moved significantly slower because of decreased focal adhesion turnover.

Over 200 different proteins are involved in linking integrins to the actin cytoskeleton, highlighting the complexity of focal adhesions (95). One critical protein linking integrins to the actin cytoskeleton is vinculin. Vinculin binds to F-actin on its carboxy-terminus and binds to talin on its amino-terminus, while talin binds directly to β-integrin subunits (96, 97). Vinculin is required for formation and enlargement of focal adhesions and is required for invasion in 3D cultures (98, 99). A recent study has described a new role for β1 integrins in focal adhesions. Theisen et al. showed that stabilized cell tails promote directional (non-random) cell migration in human retinal pigment epithelial RPE1 cells and human osteosarcoma U2OS cells (100). Paxillin staining showed that focal adhesions accumulate in these cell tails. Furthermore, the kinesin KIF1C was required for transport of α5β1 integrin to trailing focal adhesions within the cell tails. Trailing adhesions are proposed to act as a rudder for cells, providing physical drag while prescribing the direction of movement (100, 101).

1.5.3 Invadopodia: structure, function, and regulation

Invadopodia are adhesive, cancer cell-specific structures that concentrate MT1-MMP for ECM degradation. Invadopodia allow cancer cells to coordinate ECM degradation with cell migration to facilitate movement through tissue microenvironments (102). It is hypothesized that rather than creating their own ECM degradation mechanisms, cancer cells have co-opted the mechanisms of podosomes, structures analogous to invadopodia that are found in normal cells (102). Podosomes are used by osteoclasts to remodel bone during development, growth, and repair of the skeleton and are used by macrophages to extravasate to sites of injury or infection (103, 104). Podosomes are absent in macrophages of patients with Wiskott–Aldrich Syndrome, indicating an import physiological role for these structures (105). While podosomes and invadopodia are similar in structure and function, differences have been noted. For example, studies have shown that invadopodia protrude further into ECM than podosomes and that invadopodia are stable for hours compared to minutes for podosomes (106). These differences may account for the higher degradative ability of cancer cells.

<u>Stages of invadopodium formation</u>

Invadopodium formation can be broken down into 3 stages, with the key proteins highlighted (Figure 1-4b) (102). In the first stage, invadopodium formation is initiated by the binding of growth factors to their cognate growth factor receptors. EGF, TGF-β, VEGF, and HGF signalling all activate Src family of tyrosine kinases (107). Scr then phosphorylates Tyr kinase substrate with five SH3 domains (TKS5) (108). Phospho-Tks5 is required for the recruitment of cortactin to the plasma membrane at sites of invadopodia formation (109). In the second stage, invadopodia are assembled by the activity of cortactin. Cortactin, also a Src substrate, is the master regulator of several

actin-regulatory proteins (102, 110, 111). Phospho-cortactin binds via its SH3 domain directly to N-WASp and via its NTA domain directly to Arp2/3 (111). N-WASp activates Arp2/3 which nucleates new actin filaments while it is bound to existing filaments, thus creating a branched network of actin filaments (112). Actin polymerization pushes the nascent invadopodium in contact with the ECM (111). In the third stage, invadopodia mature by the presentation of matrix metalloproteinase MT1-MMP to the tip of the protruding invadopodium, enabling focal degradation of the ECM (102). Tyrosine kinase substrate with four SH3 domains (TKS4) has been shown to be required for recruitment of MT1-MMP to podosomes and for ECM degradation to take place (113).

Identification of invadopodia

Focal adhesions and invadopodia share many proteins including F-actin, Arp2/3, and cortactin. Therefore, presence of these proteins by immunostaining is not sufficient to identify invadopodia. Focal adhesions are present at the leading edge of the cell while podosomes are often found at the ventral (underside) cell surface behind the leading edge of the cell and invadopodia are found at the ventral cell surface often under the nucleus (Figure 1-4a) (102, 114). Confocal or TIRF microscopy must be used to confirm that these structural proteins are present at the ventral (underside) of the cells in order to identify podosomes or invadopodia in 2D culture. Alternatively, F-actin can be co-localized with TKS5 to mark invadopodia. TKS5 does not localize to other actin-based structures and is exclusively found in podosomes and invadopodia (115). TKS5 has also been shown to be sufficient for the formation of invadopodia. Its expression was sufficient to form invadopodia in T47D metastatic breast cancer cells that normally have low baseline expression of TKS5 and do not form invadopodia (116). The ideal way of identifying invadopodia is to co-localize a structural component (F-actin, cortactin, TKS4, TKS5) with a functional component (MMP2, MMP9, MT1-MMP, matrix degradation).

Invadopodia are classically identified in 2D culture by the co-localization of F-actin with degradation of a thin underlying layer of fluorescently-labelled matrix protein (such as gelatin, collagen, or fibronectin). The presence of matrix degradation is a useful way to differentiate invadopodia from focal adhesions.
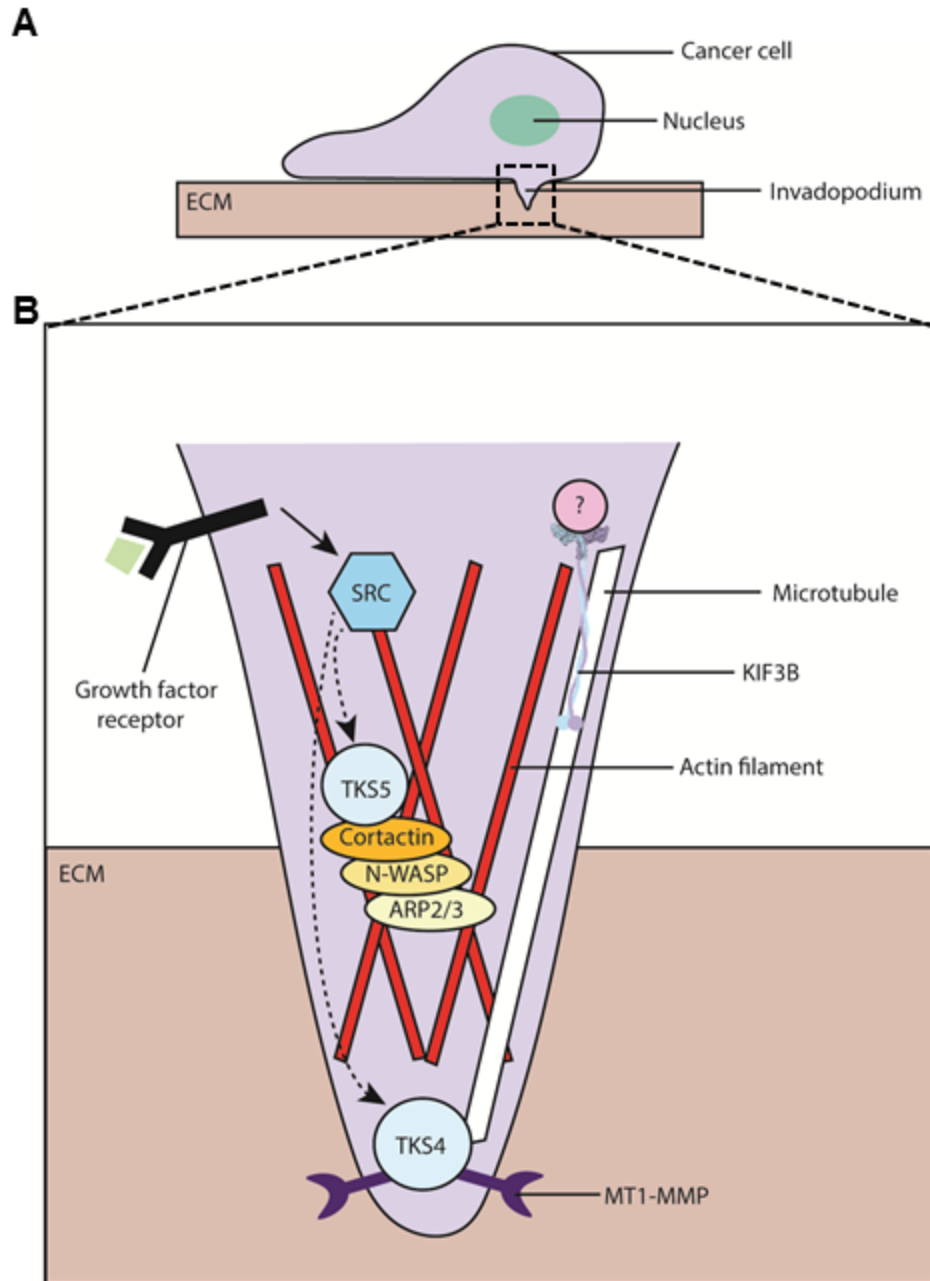
Figure 1-4. Structure and function of invadopodia
(A) Invadopodia are adhesive, cancer cell-specific structures that concentrate matrix metalloprotease MT1-MMP (also known as MMP14) for extracellular matrix degradation. Invadopodia are found on the ventral (underside) cell surface, often under the nucleus. (B) Growth factor signaling stimulates the formation of invadopodia through the activation of Src family of tyrosine kinases. Actin polymerization and branching causes the plasma membrane to protrude into the underlying matrix and is mediated by TKS5. MT1-MMP is recruited to the plasma membrane for ECM degradation by TKS4.

Evidence for invadopodia formation *in vivo*

The term invadopodia was coined in 1989 by Wen-Tien Chen and since that time invadopodia have been demonstrated to form in 2D culture in numerous human cancer cell lines (117). However, identifying a role for invadopodia *in vivo* has been elusive because of the difficulty in visualizing tumour cell interactions with basement membrane (118). The basement membrane is a barrier cancer cells must degrade and traverse in order to metastasize. Gligorijevic et al. have provided indirect evidence for the role of invadopodia in invasion and intravasation *in vivo* (119). Using an allograft rat mammary tumor model, they showed that knockdown of invadopodia component N-WASp led to less collagen-I degradation around the primary tumour and in areas surrounding blood vessels. While visualization of invadopodia markers was not undertaken at these sites, these findings suggested that invadopodia may be required for local invasion out of the primary tumour and for intravasation into blood vessels *in vivo.* Recently, our group provided the first direct evidence for the role of invadopodia *in vivo*, showing that they are required for extravasation out of the avian embryo CAM (120). Using a panel of cancer cell lines (HEp3 epidermoid carcinoma, HT1080 fibrosarcoma, B16F10 melanoma, MDA-MB-231LN breast, T24 bladder), our group showed that cancer cells follow a single protrusion to extravasate out of the CAM plexus. All cells examined reached the extravascular stroma by displacing two adjacent endothelial cells with no evidence of trans-cellular migration through a single endothelial cell. The enrichment of cortactin, TKS4, TKS5, and MT1-MMP in these protrusions provided evidence that they are indeed invadopodia. shRNA knockdown of TKS4 and TKS5 significantly reduced the number of cancer cells that extravasated in the avian CAM and the number of cells that could colonize the lungs of nude mice following intravenous injection. Overall, these data

showed that invadopodia are required for extravasation and that invadopodia can be targeted to block metastasis.

Matrix metalloproteases in invadopodia

Proteases, also known as proteinases and peptidases, are enzymes that catalyze the degradation of protein substrates. They are grouped into seven families based on the residues used to catalyze the reaction: serine proteases, cysteine proteases, threonine proteases, aspartic proteases, glutamic proteases, metalloproteases, and asparagine peptide lyases (121). Metalloproteases are proteases that require metal ions to catalyze protein degradation (122). The metalloprotease family is further divided into metalloexopeptidases and metalloendopeptidases (EC numbers 3.4.17 and 3.4.24, respectively) (123), with a disintegrin and metalloproteases (ADAMs) and matrix metalloproteases (MMPs) as notable metalloendopeptidases. As of 2010, 25 different MMPs have been identified in vertebrates. 24 of these MMPs are present in humans including two identical forms of MMP-23 that are encoded by duplicated genes (124).

The hallmark of a mature invadopodium is the enrichment of MT1-MMP at the tip of the protruding structure (102). MT1-MMP (membrane-type-1 MMP, also known as MMP14) is a matrix metalloprotease that is required for invasion through tightly cross-linked collagen that is characteristically found in the stromal ECM around normal tissues (87, 125). MT1-MMP is composed of a signal peptide, a propeptide, and a catalytic domain (126). Synthesized as a zymogen, MT1-MMP is converted to a catalytically active enzyme by proteolytic cleavage of the propeptide by furin in the trans-Golgi network (126). The signal peptide targets MT1-MMP to the plasma membrane where it is active as a trans-membrane protein. MT1-MMP directly cleaves ECM components including type-I, -II, -III (and possibly type-IV) collagen, gelatin, laminins 1 and 5, fibronectin,

vitronectin, aggrecan, and fibrin (127, 128). Furthermore, MT1-MMP activates the secreted gelatinases MMP2 and MMP9 (129, 130).

Regulation of MT1-MMP trafficking

The cell surface localization of MT1-MMP is regulated by endocytic and exocytic mechanisms. In HT1080 fibrosarcoma cells, MT1-MMP is internalised by a combination of clathrin-mediated endocytosis and caveolar endocytosis (131). Recent observations have shown that extracellular type-I collagen interferes with clathrin-mediated uptake of MT1-MMP, suggesting that environmental cues increase the level of the MT1-MMP at the cell-matrix interface (132). Furthermore, rigidity of gelatin (hydrolyzed collagen) matrices induces invadopodia formation and activity, suggesting invadopodia are used by cancer cells in response to ECM barriers (133). Studies have shown that MT1-MMP localizes to caveolar detergent-resistant membranes, suggesting a role for the caveolae in the cell surface localization of MT1-MMP as well (134). Newly synthesized MT1-MMP has been shown to be transported to the plasma membrane by a Rab8-dependent exocytic pathway (135). Interestingly, internalized MT1-MMP is recycled to the plasma membrane both by a Rab4-recycling endosome pathway and through the trans-Golgi network (131, 136). A pool of pre-synthesized MT1-MMP that can be recycled to the cell surface may represent a rapid mechanism for localization of MT1-MMP to the leading edge in migrating cells (131). Separate studies have also shown that exocyst protein Sec8 and SNARE protein VAMP-7 are required for delivery of MT1-MMP to the plasma membrane in invadopodia, suggesting MT1-MMP trafficking is regulated at several levels (137, 138).

As discussed above, MT1-MMP trafficking between different cell compartments is a highly regulated process. The physical transport of cargoes between these different cell

compartments requires motor proteins. Recently, Wiesner et al. demonstrated that

kinesins KIF3A, KIF3B and KIF5B are required for proper cell surface localization of

MT1-MMP in primary human macrophages as assessed by confocal microscopy and

flow cytometry (139). Furthermore, they showed that KIF3A, KIF3B and KIF5B are all

required for podosome-mediated degradation of fibronectin, collagen I, and gelatin

matrices. The kinesin(s) transporting MT1-MMP to invadopodia in cancer cells have yet

to be identified.

1.6 Lipid nanoparticle-mediated RNA interference as an anti-metastatic therapy

1.6.1 RNA interference pathway: miRNAs and siRNAs

RNA interference (RNAi) is an endogenous pathway in eukaryotic cells where sequence-specific non-coding microRNAs (miRNA) silence the expression of mRNA (140, 141). Mature miRNAs are produced in a multi-step process in the cell (142). miRNA genes are first transcribed in the nucleus by RNA polymerase II or RNA polymerase III into primary miRNA (pri-miRNA) transcripts that can be several kilobases long (143, 144). Next, the pri-miRNA is cleaved by the Drosha/DGCR8 microprocessor complex. Drosha is an RNase III that is guided to its target by the double-stranded RNA binding protein DGCR8 (145). The product of the microprocessor complex is termed pre-miRNA, an approximately 65 nucleotide hairpin intermediate. pre-miRNAs are then recognized by exportin-5 and exported from the nucleus into the cytoplasm (146). TRBP stabilizes the RNase III called Dicer that cleaves the loop off of the pre-miRNA, generating a roughly 22-nucleotide miRNA duplex with two nucleotides protruding as overhangs at each 3' end (147, 148). The duplex is then unwound by the RNA-induced silencing complex (RISC) with the passenger strand degraded by Ago2 (149). The mature single-stranded miRNA then guides the RISC to its target mRNA for silencing of gene expression (150).

Small interfering RNAs (siRNAs) are 19-29 nucleotide synthetic analogues of miRNAs that can be exogenously introduced into cells (151). Designed as two complementary strands lacking a connecting loop, siRNAs bypass processing by Drosha and Dicer for direct integration into RISC for silencing of a single mRNA (140). A major difference between siRNAs and miRNAs is the mechanisms by which they silence gene expression. The siRNA guide strand must be completely complementary to the mRNA

target in order to elicit RNA interference (152). siRNAs induce endonucleolytic cleavage by Ago2 between bases 10 and 11 from the 3' end of the mRNA (153). The mRNA fragments are then degraded by exonucleases (154). In contrast, a miRNA needs to only be partially complementary to its target mRNA. Only the 'seed sequence' in a miRNA (nucleotides 2 to 7 from the 5' end of the mature miRNA) must be identical to the target mRNA to facilitate RNA interference (155). This has two functional consequences. First, due to partially complementary base pairing between miRNA and mRNA, silencing of mRNA targets by miRNA predominantly occurs through repression of translation or through degradation by deadenylation, decapping or exonuclease action (156). In rare cases of high levels of complementarity between miRNA and mRNA, miRNA may induce mRNA to undergo endonucleolytic cleavage (157). Second, because partial base pairing between a miRNA and an mRNA is often sufficient for RNAi, a single miRNA can regulate several target mRNAs (158).

1.6.2   siRNAs for anti-cancer treatment

For treating diseases, some protein targets are considered 'non-druggable' because these proteins lack enzymatic function or are inaccessible to conventional small molecule drugs (159). Even for biologic agents like monoclonal antibodies that are highly specific, their targets are mainly limited to cell-surface proteins or circulating proteins (152). These limitations can be overcome by siRNA and miRNA because they can downregulate virtually any gene by preventing expression of mRNA transcripts. As uncontrolled cell division in cancer results from overexpression of normal or mutated genes, siRNAs and miRNAs have great potential as anti-cancer agents. The high specificity of siRNAs combined with the heterogeneity of mutations in cancer make

siRNAs a possible future platform for personalized medicine (159). In comparison, because a single miRNA can target multiple genes, there is a higher potential for unknown off-targets effects. These concerns have made siRNAs the favoured molecules for use in RNA interference clinical trials.

1.6.3 Lipid nanoparticles for siRNA delivery

Intravenous delivery of siRNA is used when local delivery would be invasive (for example to reach an internal organ) (160). However, unmodified siRNAs face several barriers when delivered systemically *in vivo.* They are vulnerable to degradation by serum nucleases and may bind to serum proteins or non-target cells (140). Furthermore, unmodified siRNAs are hydrophilic and negatively charged, preventing them from readily crossing cell membranes (160). While chemical modifications can resolve issues with delivery of naked siRNAs such as degradation by serum nucleases and stimulation of the innate immune system, these modifications may alter the specificity and functionality of the siRNAs (152, 161). Therefore, alternative delivery systems are being actively explored to overcome these challenges.

The two broad categories of delivery systems for nucleic acids are viral and non-viral vectors. Viral vectors have been used for the delivery of shRNA or miRNA to facilitate RNA interference (162) but are not used to deliver siRNA. Compared to viral vectors, non-viral vectors have relatively good safety profiles, cost less to produce, and are highly versatile (152). Non-viral vectors are grouped into polymer-based and lipid-based systems. Polymers include cationic molecules like polyethylenimine (PEI) that can form polyplexes with negatively charged RNA through electrostatic interactions (163). They also include cyclodextrins (cyclic oligomers of glucose) like the Food and Drug

Administration-approved poly(lactic-co-glycolic acid) (PLGA) that can be formed into nanoparticles or microparticles that can be loaded with RNA (164).

Most lipid nanoparticles are taken up in the cell by endocytosis which subjects cargo to the endosome-lysosome pathway. Cargo must be stable in the low pH environment of endosomes and be able to escape into the cytoplasm to mediate RNAi (165). To circumvent potential loss of cargo by endosomal uptake, our group uses the Fusogenix liposome platform developed by Innovascreen Inc. The cornerstone of this highly tunable platform is the p14 fusion-associated small transmembrane (FAST) protein. Inserted into the lipid nanoparticle membrane, p14 mediates membrane fusion between the LNP and plasma membrane, bypassing the endosome-lysosome pathway and delivering cargo directly to the cytoplasm (166-168). Fusogenix liposomes can be made tissue-selective by conjugating cancer-targeting peptides to the C-terminal domain of p14. For example, prostate cancer overexpresses gastrin releasing peptide receptor (GRPR) (169). Our group conjugated p14 to bombesin (a GRPR ligand) and showed that p14-bombesin Fusogenix liposomes preferentially target prostate cancer cells (PC3) over non-cancerous prostate cells (benign prostatic hyperplasia, BPH). Finally, to prolong blood circulation Fusogenix liposomes are coated with polyethylene glycol (PEG) to minimize non-specific interactions with serum proteins, innate immune cells, and non-target tissues (160). Our group now uses Precision Nanosystems' Nanoassemblr™ for the production of nanoparticles. The Nanoassemblr™ is a scalable system that uses microfluidic mixing to provide superior batch-to-batch consistency of generated particles compared to manual syntheses.

1.6.4 siRNAs in clinical trials

As of February 2017, 70 clinical trials have been initiated for 31 siRNA drug candidates by companies or academic institutions (170). Three of these trials have reached Phase III. The clinical trials have concerned 18 different diseases in the fields of cancer, ocular, infection, metabolic and genetic diseases. Sustained cell signaling and angiogenesis promote tumour growth and survival. Cell-cycle protein kinesin spindle protein (KSP) and vascular endothelial growth factor (VEGF) have been shown to mediate these respective processes (171, 172). To this end, ALN-VSP02, a lipid nanoparticle containing siRNAs against both KSP and VEGF was used in a phase I clinical trial to treat patients with advanced solid tumours (173). The LNP treatment was well tolerated in 40 of 41 patients. Disease was stabilized in two patients with renal cell carcinoma with extrahepatic disease and a complete response was observed in a patient with endometrial cancer, eliminating her primary tumour, and liver and lymph node metastases. To prove that these effects were mediated by RNAi, the authors demonstrated that VEGF siRNA was present within the liver tumours and detected cleaved VEGF mRNA in the tumours. In a separate phase I/II clinical trial, Atu027, a liposomal siRNA targeting PNK3 was used to treat patients with advanced solid tumours (174). This nanoparticle was also well tolerated and stabilized disease in 41% of patients (14 out of 34).

In the future, an siRNA-based anti-metastatic therapy could be offered to those patients at high risk of developing metastatic disease while treatment for low risk patients can focus on targeting the primary tumour (175). Prevention of metastasis would ultimately reduce suffering and death in patients with cancer.

1.7 Hypothesis and Objectives

From our intravital imaging experiments, we observed that metastatic HEp3 colonies depleted of KIF3B form long cytoplasmic extensions but are unable to productively migrate. We postulate that this could be due to loss of key functions at the leading and trailing edges of the cancer cells. Focal adhesions are integrin-mediated multi-protein structures that link the extracellular matrix to the actin cytoskeleton (90). Traction forces generated at focal adhesions are transmitted to the ECM and are used by cells to move forward (91). Recently, it was shown that focal adhesions accumulate in and stabilize cell tails, promoting directional (non-random) cell migration in human retinal pigment epithelial RPE1 cells and human osteosarcoma U2OS cells. The kinesin KIF1C was required for transport of α5β1 integrin to trailing focal adhesions within the cell tails (100). I hypothesize that KIF3B, a related kinesin transports key molecule(s) necessary for focal adhesion assembly at the trailing cell edge.

In primary human macrophages, KIF3B is required for proper cell surface exposure of the matrix metalloproteinase MT1-MMP and is required for podosome-mediated degradation of fibronectin, collagen-I, and gelatin matrices (139). MT1-MMP is enriched in cancer cell-specific adhesive structures known as invadopodia and is required for extracellular matrix degradation and cell invasion (87). Furthermore, our group showed that invadopodia are required for extravasation (120). Therefore, I hypothesize that KIF3B transports MT1-MMP to invadopodia to mediate cancer cell motility.

Our group has shown through an RNA interference strategy that KIF3B is required for cancer cell motility in avian embryos and spontaneous metastasis in nude mice. Recent clinical trials have shown that siRNAs can mediate specific gene knockdown in cancer tissues and that lipid nanoparticle siRNA formulations are well tolerated by patients (173,

174). Therefore, I hypothesize that targeting of KIF3B with a lipid nanoparticle containing siRNA against KIF3B can specifically block cancer metastasis.

My hypotheses and objectives on the role of KIF3B in cancer cell motility and targeting of KIF3B to block metastasis are summarized below.

Hypothesis 1: KIF3B transports key molecule(s) necessary for focal adhesion assembly

- Objective 1: Determine if KIF3B knockdown reduces the size and number of focal adhesions marked by vinculin

Hypothesis 2: KIF3B transports MT1-MMP to invadopodia to mediate cancer cell motility

- Objective 1: Determine if KIF3B is required for gelatin degradation
- Objective 2: Determine if KIF3B is required for extravasation
- Objective 3: Determine if KIF3B is required for MT1-MMP cell surface exposure

Hypothesis 3: KIF3B can be targeted to block metastasis

- Objective 1: Select custom KIF3B siRNAs and test their potency *in vitro*
- Objective 2: Determine if KIF3B siRNA transfection blocks cancer cell motility *in vivo*
- Objective 3: Develop RNAi lipid nanoparticle for anti-metastasis therapy

2 Chapter Two – Materials & Methods

2.1 Cells, antibodies, and stains

The human epidermoid carcinoma cell line HEp3, human fibrosarcoma cell line HT1080, and human prostate adenocarcinoma cell line PC3 were purchased from American Type Culture Collection (ATCC). All cell lines were cultured in DMEM high glucose supplemented with 10% fetal bovine serum and 1% penicillin-streptomycin, at 37°C and 5% CO_2, hereafter described as complete media.

Primary antibodies used for Western blots include KIF3A (mouse monoclonal, Santa Cruz, 1:500), KIF3B (rabbit polyclonal, Santa Cruz, 1:1000), MT1-MMP (mouse monoclonal, EMD Millipore, 1:1000), β-tubulin (mouse monoclonal, Invitrogen, 1:5000) and actin (rabbit polyclonal, Sigma-Aldrich, 1:5000). AlexaFluor secondary antibodies (AF680 goat-anti-rabbit and AF750 goat-anti-mouse, Invitrogen) were used at 1:10,000 for Western blots.

For focal adhesion immunostaining, cells were stained with vinculin primary antibody (mouse monoclonal, Sigma,1:500) and AlexaFluor-488 goat-anti-mouse secondary antibody (Invitrogen, 1:1000). To stain F-actin in FITC-gelatin degradation assay, cells were incubated with phalloidin-647 (Invitrogen, 1:100) for 1 hour. All immunostained samples were stained with 10µg/mL Hoechst 33342/1X PBS (Invitrogen) for 1 hour.

For flow cytometry, cells were stained with MT1-MMP (mouse monoclonal, LEM-2/15.8, EMD Millipore, 1µg/mL in 0.5% BSA/1X PBS) or isotype control (mouse anti-IgG1-k, EMD Millipore, 1µg/mL in 0.5% BSA/1X PBS) primary antibodies. Cells were then stained with AlexaFluor secondary antibody (AF647 goat-anti-mouse, Invitrogen, 1:200 in 0.5% BSA/1X PBS).

2.2 KIF3B siRNA transfection

A pool of three lyophilized target-specific KIF3B siRNAs were purchased from Santa Cruz (sc-43376) and resuspended in RNAse-free H_2O to make a 10µM solution.

Cells were seeded to achieve 70% confluency within 16 hours. 40,000 HT1080 wild-type cells (or 55,000 HEp3 wild-type cells) were seeded dropwise into wells of a 12 well plate at 4pm. **Critical step**: plates were rocked to evenly distribute cells across the wells. Plates were tilted forward and back four times, tiltied left and right four times, then while keeping plate parallel to floor media was 'pushed' forward and back four times, and pushed left and right four times. Finally, plates were placed in a 37°C/5% CO_2 incubator overnight.

The following day, 8µL of 10µM KIF3B siRNA was added to 100µL of warm (37°C) OptiMEM (Gibco) in a 1.5mL Eppendorf tube for each 12 well to be transfected. RNAse–free H_2O was substituted for KIF3B siRNA in the mock transfected group. The Eppendorf tube was gently vortexed and incubated at room temperature for 5 minutes. Concurrently, 3.5µL of lipofectamine 2000 (Invitrogen) was added to 100µL of warm OptiMEM in a 1.5mL Eppendorf tube. The Eppendorf tube was gently vortexed and incubated at room temperature for 5 minutes. The siRNA-containing OptiMEM was then added to the lipofectamine 2000-containing OptiMEM. The tube was gently vortexed and incubated at room temperature for 20 minutes. During this incubation period, media was removed from the cells. The wells were then gently washed twice with 1000µL PBS. **Critical step:** care was taken to minimize the amount of time that the cells were dry and wherever possible, solutions were aspirated and gently added to cells using a micropipette rather than a vacuum to minimize disruption to cells. 800µL of antibiotic-free DMEM high glucose/10% FBS was added to the side of the well. After the 20 minute

incubation, the siRNA-lipofectamine 2000 complexes were added dropwise to the wells using a p200 micropipette. Complexes were added to the wells by 9am and distributed evenly across the well by rocking the plates as described above. Cells were transfected with a final concentration of 80nM KIF3B siRNA. Four hours post-transfection the cells were gently washed twice with PBS. 1 mL complete media was added to each well.

24 hours post-transfection, the cells were split for Western blot. Each well was washed once with 1000μL PBS. 200μL of TrypLE Express (ThermoFisher) was added to the cells. The cells were then placed in a 37°C/5% CO_2 incubator for 5 minutes. The TrypLE Express was then neutralized with 800μL complete media. The detached cells were then pipetted up and down to dissociate clumps. 667μL of the cell suspension was seeded into a 6 well plate containing 2mL of complete media. The remaining 333μL of cell suspension was retained in the original 12 well plate for Western blot.

48 hours post-transfection cell lysates were collected from the 12 well plates to verify KIF3B knockdown by Western blot (as described below) and cells in the 6 well plates were used for the respective experiments. All experiments using siKIF3B transfected cells were commenced at 48 hours post-transfection, when maximum KIF3B knockdown was present.

2.3 Western blot

Culture plates were placed on ice. Cells were washed with ice cold PBS. 1X protease inhibitor cocktail/RIPA buffer was added to cells and they were scraped off the plate and transferred to a 1.5mL Eppendorf tube. Cells were then incubated at 4°C while rocking for 30 minutes. Resulting cell lysates were centrifuged at 16,000g, 4°C for 15 minutes.

Supernatant was transferred to a new tube and protein concentration was determined using the Pierce™ BCA Protein Assay Kit (ThermoFisher). Laemmli sample buffer (6X) was then diluted in cell lysates to a final concentration of 2X. Samples blotted for KIF3A or KIF3B were heated at 95°C for 10 minutes and samples blotted for MT1-MMP were heated at 70°C for 10 minutes then briefly centrifuged. 10µg of protein per sample was loaded into polyacrylamide gels and electrophoresed under reducing conditions.

KIF3A and KIF3B were resolved using 8% polyacrylamide gels for 30 minutes at 90V followed by 90minutes at 120V. MT1-MMP was resolved using 15% polyacrylamide gels for 20 minutes at 90V followed by 70 minutes at 150V. Proteins were transferred onto nitrocellulose membranes using 1X Towbin buffer, at 4°C for 2 hours at 80V. Membranes were blocked for 1 hour at room temperature using Rockland blocking buffer (MB-070). Membranes were incubated in primary antibody against KIF3A, KIF3B or MT1-MMP overnight at 4°C. Membranes were then washed with 0.1% Tween-20/TBS for 30 minutes. Membranes were incubated with AlexaFluor secondary antibodies for 1 hour at room temperature, protected from light then washed with 0.1% Tween-20/TBS for 30 minutes. Membranes were scanned for target protein using LI-COR Odyssey® Imaging System. Membranes were incubated in primary antibody against housekeeping protein (β-tubulin or actin) plus respective secondary antibody for 1 hour at room temperature, protected from light. Membranes were then washed with 0.1% Tween-20/TBS for 30 minutes and scanned for housekeeping protein using LI-COR Odyssey® Imaging System.

To quantify relative protein expression, protein of interest level was normalized to housekeeping protein level in each sample. Protein bands were quantified using densitometry function in Odyssey Version 3.0.29 (LI-COR), applying the same size frame to each band.

2.4 Immunofluorescence

Immunofluorescence protocols were adapted from (176) and (177). 24 hours post-transfection, 18mm #1.5 borosilicate glass coverslips were submerged and sterilized in isopropanol for 5 minutes, washed two times with PBS, placed in the wells of a 12-well plate, and coated with 1000µL of 10µg/mL fibronectin (Thermo RP-43130) for 1 hour at 37°C/5% CO_2. The coated coverslips were washed three times with PBS. In 1mL complete media, 10,000 cells were seeded onto fibronectin-coated coverslips and placed in a 37°C/5% CO_2 incubator overnight.

48 hours post-transfection, the media was gently removed from each individual well and 500µL of freshly thawed 4% paraformaldehyde was added to each well for 15 minutes to fix the cells. Cells were washed three times with 1000µL PBS, 5 minutes for each wash. The cells were then permeabilized and blocked in 0.3% TritonX100/5% normal goat serum/1X PBS for 1 hour.

A humid chamber was prepared for immunostaining as follows. Filter paper was cut to fit the interior diameter of a 150mm petri dish, soaked in ddH_2O, and placed into the petri dish. Parafilm was laid on the filter paper. 30µL of the primary antibody dilution was piptetted onto the parafilm and the coverslips were inverted cell-side down onto the solution. The dish was covered with its lid and the coverslips were incubated at room temperature for 1 hour. The coverslips were then placed cell-side up into the 12-well plate and washed gently 3 times with 1000µL PBS. The used piece of parafilm was discarded and replaced with a new piece on top of the filter paper. 30µL of the secondary antibody dilution was pipetted onto the parafilm and the coverslips were inverted cell-side down onto the solution. The dish was covered with its lid and the

coverslips were incubated at room temperature for 1 hour, protected from light. The coverslips were then placed cell-side up into the 12-well plate and washed gently 3 times with 1000μL PBS. The coverslips were briefly dipped in ddH$_2$O to remove salts and dried by touching their edge to a KimWipe. Coverslips were mounted onto glass slides using ProLong® Gold Antifade (ThermoFisher). Mountant was allowed to cure overnight at room temperature, protected from light. Coverslips were then sealed onto the slides using clear nail polish. 30 minutes later, coverslips were gently cleaned using a cotton swab wet with ddH$_2$O. Coverslips were then imaged immediately.

2.5 Vinculin focal adhesion quantifications with imageJ

The Z-slice capturing the focal plane of each field was exported as a TIFF. A representative image was thresholded using ImageJ (National Institutes of Health) to remove background in the vinculin channel. These thresholding parameters were then recorded in a macro to expedite thresholding of all images. The macro is listed below.

```
run("8-bit");
setAutoThreshold("Default");
//run("Threshold...");
setThreshold(30, 255);
setOption("BlackBackground", false);
run("Convert to Mask");
```

The cross-sectional area of the focal adhesions in each cell was then measured using the wand (tracing) tool and the number of analyzed focal adhesions was tracked in the results pane. The average number of focal adhesions per cell and average cross-sectional area of focal adhesions was compiled in Excel (Microsoft).

2.6 FITC-gelatin degradation assay

The protocol for coating coverslips was adapted from Artym, Yamada & Mueller (178).

<u>Acid washing coverslips</u>

18mm #1.5 borosilicate glass coverslips were washed in 20% nitric acid for 2 hours, and the acid was swirled every 30 minutes. The acid was removed and the coverslips were washed in ddH_2O for 2 hours, changing the water every 30 minutes. The coverslips were then dried by passing through a flame and stored in a sterile, sealed beaker.

<u>Coating coverslips in FITC-gelatin</u>

The following steps were done sterilely in a biosafety cabinet. Acid washed coverslips were placed into a 12 well plate and covered in chilled, 50 µg/mL poly-L-lysine for 20 minutes at room temperature. The poly-L-lysine was aspirated and the coverslips were washed three times in 1mL of PBS. 1mL of 0.5% glutaraldehyde/1X PBS was applied to the coverslips for 15 minutes at room temperature. The glutaraldehyde was aspirated and the coverslips were washed three times in 1mL PBS. The following steps were performed in the dark. 40µL of preheated (37ºC) diluted fluorescent gelatin (1 part 0.1% FITC-conjugated gelatin (ThermoFisher) to 19 parts 0.2% unconjugated porcine gelatin (Sigma)) was deposited onto a sheet of parafilm for each coverslip. The coverslips were inverted onto the diluted fluorescent gelatin, activated side down. The coverslips were then incubated at room temperature for 10 minutes. The coverslips were inverted again, coated side up, and placed into the 12 well plates and gently washed three times with 1mL PBS. 5 mg/mL sodium borohydride ($NaBH_4$) was then applied to the coverslips for 15 minutes at room temperature. The coverslips were washed ≥3 times with 1mL PBS to

wash away all bubbles. 1mL complete media was added to the coverslips and the coverslips were stored in a 37°C/5% CO_2 incubator and used the following day.

Gelatin degradation assay

A 10,000 cell/mL suspension was prepared (as described above). Media was aspirated from the FITC-gelatin coated coverslips and 1mL of the prepared cell suspension was seeded onto each coverslip, 48 hours post siKIF3B transfection. Each group was seeded in triplicate. Plates were placed in a 37°C/5% CO_2 incubator for 12 hours.

Cells were then fixed-permeabilized, stained for F-actin, mounted onto slides, cured, and sealed with nail polish as described above.

Quantification of FITC-gelatin degradation

The Z-slice capturing the focal plane was exported as TIFFs for the separate fluorescent channels. Degradation of FITC-gelatin was then quantified using software developed by Dr. Robert Paproski. To eliminate vignetting of corners, images were cropped to the largest circle to fit in the square image field. A confocal micrograph for a blank FITC-gelatin field was acquired to determine the signal intensity of a field that has no cells. Next, the areas lacking FITC signal on a field with cells was subtracted from the blank field to determine the total area of gelatin degradation. Total cell area on the gelatin field was quantified from phalloidin staining in AlexaFluor-647 channel. Finally, total gelatin degradation area was normalized to total cell area on the field. Each imaged field was treated as one data point.

2.7 Metastatic colony formation assay

Each cell line of interest was grown to 70% confluence in a T75cm^2 flask. Media was aspirated from the cells and they were washed twice with 10mL PBS. 2mL TrypLE Express was added to the flask and cells were incubated at 37°C/5% CO$_2$ for 5 minutes. TrypLE Express was neutralized with 8mL complete media. Detached cells were transferred to a 15mL conical and centrifuged at 200 x g for 5 minutes. The supernatant was aspirated and the cells were resuspended in 5mL PBS. The cells were centrifuged at 200 x g for 5 minutes, supernatant aspirated, and the cells were resuspended in PBS and placed on ice.

25,000 cancer cells were intravenously injected into developmental day 10 avian embryos. Intravital imaging was performed on developmental day 15 as described elsewhere (13, 24). At least 3 embryos were imaged per group, with at least 10 colonies imaged per embryo.

2.8 Extravasation assay

KIF3B siRNA transfections (as described above) were scaled up for this assay. 750,000 HT1080 tdTomato cells in 10mL media were seeded into T75cm^2 flasks. Two T75cm^2 flasks were prepared per group. 16 hours later, cells were transfected with 10mL of 80nM KIF3B siRNA. 24 hours post-transfection, 40,000 cells per group were seeded into 12 well plates for Western blotting. The remaining transfected cells were expanded into T175 cm^2 flasks.

To prepare cells for injection, media was aspirated from the flasks and cells were washed two times with 15mL PBS. 5mL of TrypLE™ Express was then added to each T175 cm^2 flask and the flasks were incubated at 37°C/5% CO$_2$ for 5 minutes. 20 mL of

complete media was added to the cells to neutralize the TrypLE™ Express and the cells were transferred to 50mL conicals. The cells were centrifuged at 200 x g for 5 minutes. Supernatant was aspirated. Cell pellets were then resuspended in 5mL PBS and centrifuged again at 200 x g for 5 minutes. The supernatant was aspirated. The cells were resuspended in PBS to form a 1 million cells/mL suspension then kept on ice.

Shell-less avian embryos were cultured as described elsewhere (9). Developmental day 14 avian embryos were intravenously injected with HT1080 tdTomato cells 48 hours post-transfection. 200,000 HT1080 tdTomato cells were injected per avian embryo, alternating between injection of mock and siKIF3B groups. At least 5 avian embryos were injected per group. Intravital imaging was commenced when 50% of cells in the mock transfected group had extravasated (~8 hours post-injection). 30µm Z-stacks of the CAM capillary plexus and extravascular stroma were acquired using Nyquist sampling. To label the luminal surface of the vasculature, 50µL of 1:50 lens culinaris DyLight649 was injected into each avian embryo 5 minutes before imaging. 4 embryos were imaged per group. >100 cancer cells were imaged per embryo. Extravasation efficiency was quantified per embryo as number of extravascular cells divided by total number of cells imaged.

2.9 Fluorescence microscopy

Metastatic colony formation assays for HT1080 shKIF3B cells and HEp3 siKIF3B cells were imaged using widefield microscopy. Images were acquired using a Zeiss Examiner Z1 upright microscope, with an X-Cite 120 fluorescent lamp (Excelitas Technologies), XY stage controller (Ludl Inc.), a Hamamatsu 1000x1000 EMCCD camera (Hamamatsu Inc.), fitted with a custom enclosure to maintain temperature at 37°C (Plastics Inc.), and

Zeiss objective lenses. Volocity 6.1 (PerkinElmer) was used to control the microscope and capture all images.

Images for all other experiments were captured using confocal microscopy. Imaging was performed with a Nikon A1R MP+ confocal microscope equipped with 405, 488, 561, and 640nm lasers, a Mai Tai InSight DS+ two photon laser, Galvano and resonant scanners capable of spectral and NDD detection modes, XY stage and Z objective lens controller (Prior), a custom enclosure to maintain temperature at 37°C (okolab), and Nikon objective lenses. NIS Elements 4.30 was used to control the microscope and capture all images. All images within the same experiment were acquired with the same laser intensity and PMT voltage. Random fields were chosen for imaging and Z-stacks were acquired using Nyquist sampling. Immunofluorescence and FITC-gelatin degradation images were acquired using a 60X oil immersion objective lens. Extravasation images were acquired using a 25X water immersion objective lens. Metastatic colony images of KIF3B CRISPR knockouts were acquired using a 10X air immersion objective lens.

2.10 MT1-MMP flow cytometry

Cells were transfected as described above. 48 hours post-transfection, media was removed from the 6-well plates with a p1000 micropipette. Cells were washed twice in 1mL 10mM EDTA/10% FBS/DMEM high glucose. 1mL 10mM EDTA/10% FBS/DMEM high glucose was then added to the wells and the cells were incubated at 37°C for 15min. Detached cells were transferred to a 1.5mL Eppendorf tube and centrifuged at 200 x *g* for 5 minutes. The supernatant was aspirated and the cells were washed and centrifuged twice in PBS. Cells for the isotype control group were stained in 100µL

mouse isotype antibody for 30 minutes at 4°C. All other groups (mock, siKIF3B, siMT1-MMP, MT1-MMP over-expression) were stained in 100μL mouse anti-MT1-MMP monoclonal antibody for 30 minutes at 4°C. All groups were washed twice by centrifuging at 200 x *g* for 5 minutes with 500μL antibody buffer (0.5% BSA/1X PBS). All groups were then stained with 100μL secondary antibody for 30 minutes at 4°C. All groups were washed twice by centrifuging at 200 x *g* for 5 minutes with 500μL antibody buffer. All groups were then re-suspended in 300μL chilled PBS and immediately analyzed on a FACS Canto II flow cytometer (BD) controlled with FACSDiva software (BD).

2.11 Selection of custom KIF3B siRNAs

Curated non-redundant KIF3B mRNA sequence was obtained from NCBI Reference Sequence (RefSeq) database as a cDNA. This cDNA sequence was input into the top 11 online siRNA design softwares available as of 2016: siDirect, siDESIGN Center, Genscript, Asi designer, BLOCK-iT RNAi Designer, RNAi explorer, RNAi codex, SiRNA at Whitehead, Oligowalk, SiRNA Design (IDT), and RNA wizard (151). The top KIF3B siRNA sequences from each software were then analyzed by NCBI Basic Local Alignment Search Tool (BLAST) to rule out significant homology to other mRNA sequences. siRNAs with greater than 15 out of 19 nucleotides matching other mRNA sequences were then eliminated because of likelihood for off-target effects (179). siRNAs that were predicted to have high on-target effects, no off-target effects, and targeted different exons in the KIF3B transcript were selected for purchase from Sigma.

2.12 Generation and assessment of KIF3B CRISPR knockouts

Guide RNAs were selected using the Benchling "Design CRISPR guides" tool
(https://benchling.com/). The Benchling platform annotates the target gene with putative
guide RNAs and allows the user to browse through the whole annotated gene.
Additionally, on-target and off-target scores are provided for each guide RNA, where on-
target score represents the cleavage efficiency of Cas9 (180) and off-target score
represents the probability that Cas9 will bind to off-targets (181). Two guide RNAs with
the highest on-target and off-target scores were selected to target the first protein-coding
exon (exon 2) in the KIF3B gene. Oligonucleotides encoding the guide RNAs and their
reverse complements were purchased from IDT and annealed in a thermocycler. The
backbone CRISPR-Cas9 plasmid PX459 (pSpCas9(BB)-2A-Puro V2.0) was a gift from
Feng Zhang (Addgene plasmid # 62988) and his protocol was followed to generate
plasmids for KIF3B knockout (182). PX459 was double-digested with BbsI and the
annealed oligos were ligated into the plasmid. Competent *E. coli* (Stbl3) were then
transformed with the generated plasmids. 3 transformed colonies for each KIF3B
CRISPR-Cas9 plasmid were sequenced to confirm that the correct KIF3B sequences
would be targeted. A kill-curve was then generated to determine the minimum puromycin
concentration required to select HT1080 cells. HT1080 cells in 12 well plates were
transfected with 0.5, 1.0 or 2.0 µg of the CRISPR-Cas9 plasmids targeting the different
KIF3B sequences. 48 hours after transfection, the HT1080 cells were selected in 1µg/mL
puromycin for 72 hours. The surviving clones were expanded and frozen back.

CRISPR-Cas9 editing of KIF3B at the genomic level was confirmed using droplet digital
PCR (ddPCR) and KIF3B knockout at the protein level was confirmed by Western blot.
Primers and probes for ddPCR were designed using Primer3plus web tool and
purchased from Integrated DNA Technologies (Appendix B). Genomic DNA from bulk

CRISPR-Cas9 edited populations was extracted using DNeasy Blood & Tissue Kit

(Qiagen) and eluted into RNase-free H_2O. A 20µL reaction for ddPCR was prepared with

10µL of ddPCR supermix with no dUTP (Bio-Rad), 1.8µL forward primer (10µM

solution), 1.8µL reverse primer (10µM solution), 1.0µL reference probe (5µM solution),

1.0µL NHEJ probe (5µM solution), 0.4µL AluI restriction endonuclease (NEB), 3µL PCR

grade H_2O, and 1.0µL genomic DNA. Each sample was then partitioned into droplets

with QX200™ Droplet Generator (Bio-Rad) and run in a T100 thermal cycler (Bio-Rad).

Droplets were analyzed for editing efficiency at the KIF3B locus using QX200™ Droplet

Reader (Bio-Rad).

2.13 Statistical Analysis

All statistical analyses were performed with GraphPad Prism® 5.0. Statistical test used

is indicated in the figure legend.

3 Chapter Three – Results

3.1 KIF3B is required for HT1080 cell motility *in vivo*

While KIF3B was identified as a driver of cancer metastasis in our shRNA screen using the HEp3 human epidermoid carcinoma cell line, we have observed that the HEp3 cell line can adopt an amoeboid mode of migration (unpublished data) that does not require the use of focal adhesions or MT1-MMP (183). Conversely, the HT1080 human fibrosarcoma cell line has been reported to have characteristics ideal for testing my hypotheses that KIF3B transports key proteins to focal adhesions and that KIF3B transports MT1-MMP to invadopodia; HT1080 cells are known to form focal adhesions and require MT1-MMP for invasion (184, 185).

To determine if KIF3B is required for HT1080 cell motility *in vivo,* I used the metastatic colony formation assay that was used to identify KIF3B as a driver of metastasis in HEp3 cells. Developmental day 10 avian embryos were injected intravenously with fluorescently labelled HT1080 shControl or shKIF3B cells and allowed to form metastatic colonies for 5 days whereupon the colonies were intravitally imaged. 30 colonies were analyzed per group with the Compactness Index (C.I.) software previously developed for our shRNA screen. We found that shRNA knockdown of KIF3B in HT1080 cells produced colonies that are significantly more compact than the shRNA control ($p < 0.0001$) (Figure 3-1).
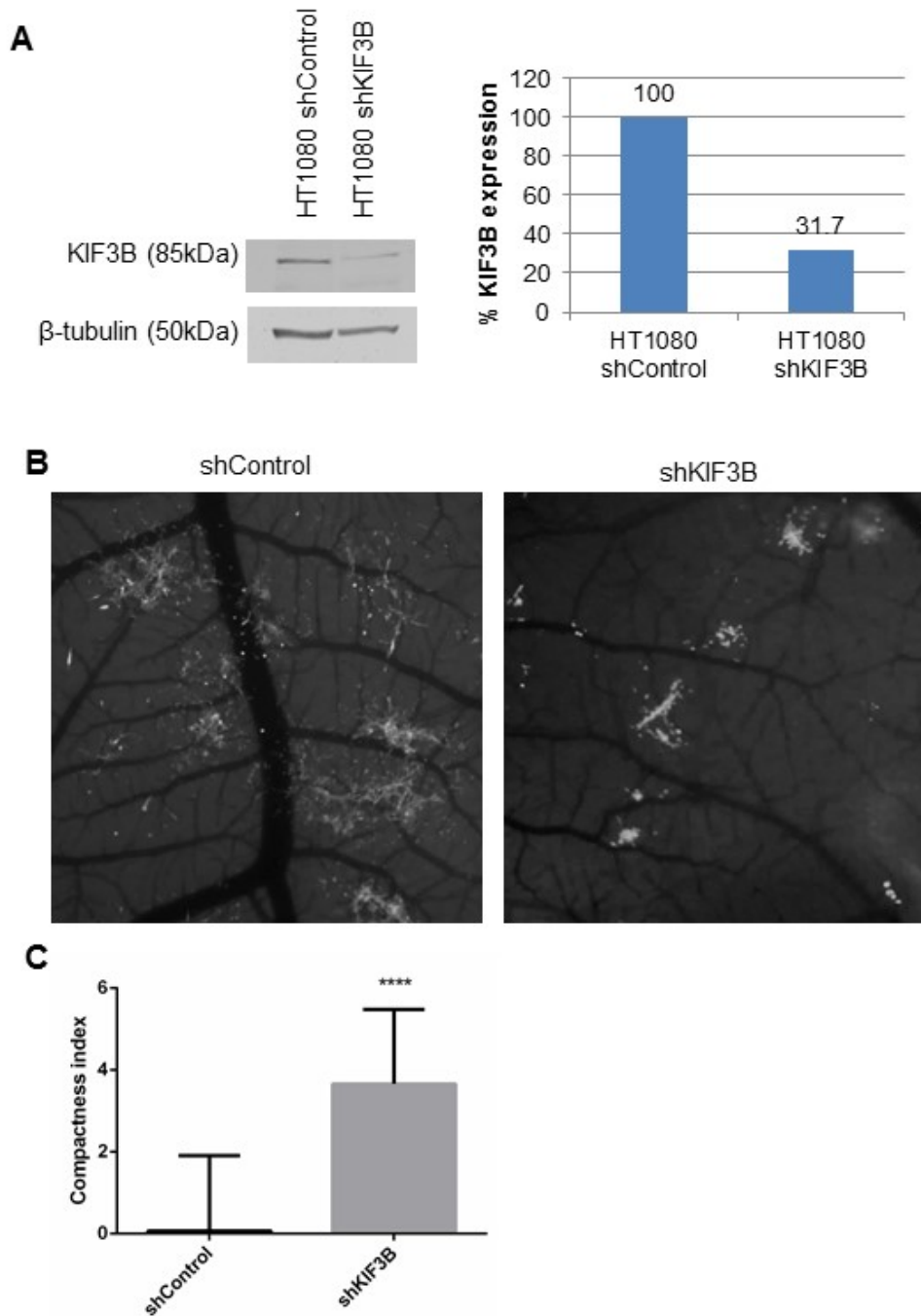
Figure 3-1. KIF3B is required for HT1080 cell motility *in vivo*
(A) Western blot of KIF3B expression in HT1080 cell lines used in metastatic colony formation assay. (B) Representative images of metastatic colonies formed in avian embryos 5 days post-injection (developmental day 15). (C) Compactness Index quantifications show that compared to control cells, HT1080 cells depleted of KIF3B form significantly more compact metastatic colonies. Data are from one experiment. 3 embryos per group, N=30 colonies per group. ****p<0.0001, two-tailed t-test of mean±SD.

3.2 KIF3B knockdown does not reduce size or number of focal adhesions

To test the hypothesis that KIF3B transports key molecule(s) necessary for focal

adhesion assembly at the trailing cell edge, I measured the cross-sectional area of focal

adhesions marked by vinculin that formed in HT1080 mock and siKIF3B cells. Vinculin is

a protein critical for focal adhesions that links integrins to the actin cytoskeleton and has

been shown to be required for invasion in 3D cultures (98). Cells were seeded onto

fibronectin coated coverslips and allowed to adhere overnight while incubated at 37°C.

The cells were then fixed and immunostained. Using a confocal microscope, 30 random

fields were imaged per group yielding >135 cells per group. The data were blinded, and

then I expedited image thresholding by creating and applying a 6-step imageJ macro to

all images. The sizes of the individual focal adhesions on the thresholded images were

measured using the imageJ wand (tracing) tool. After all the data was compiled, we

found that transient KIF3B knockdown by siRNA does not reduce the average size or

number of focal adhesions per HT1080 cell (p>0.05) (Figure 3-2).
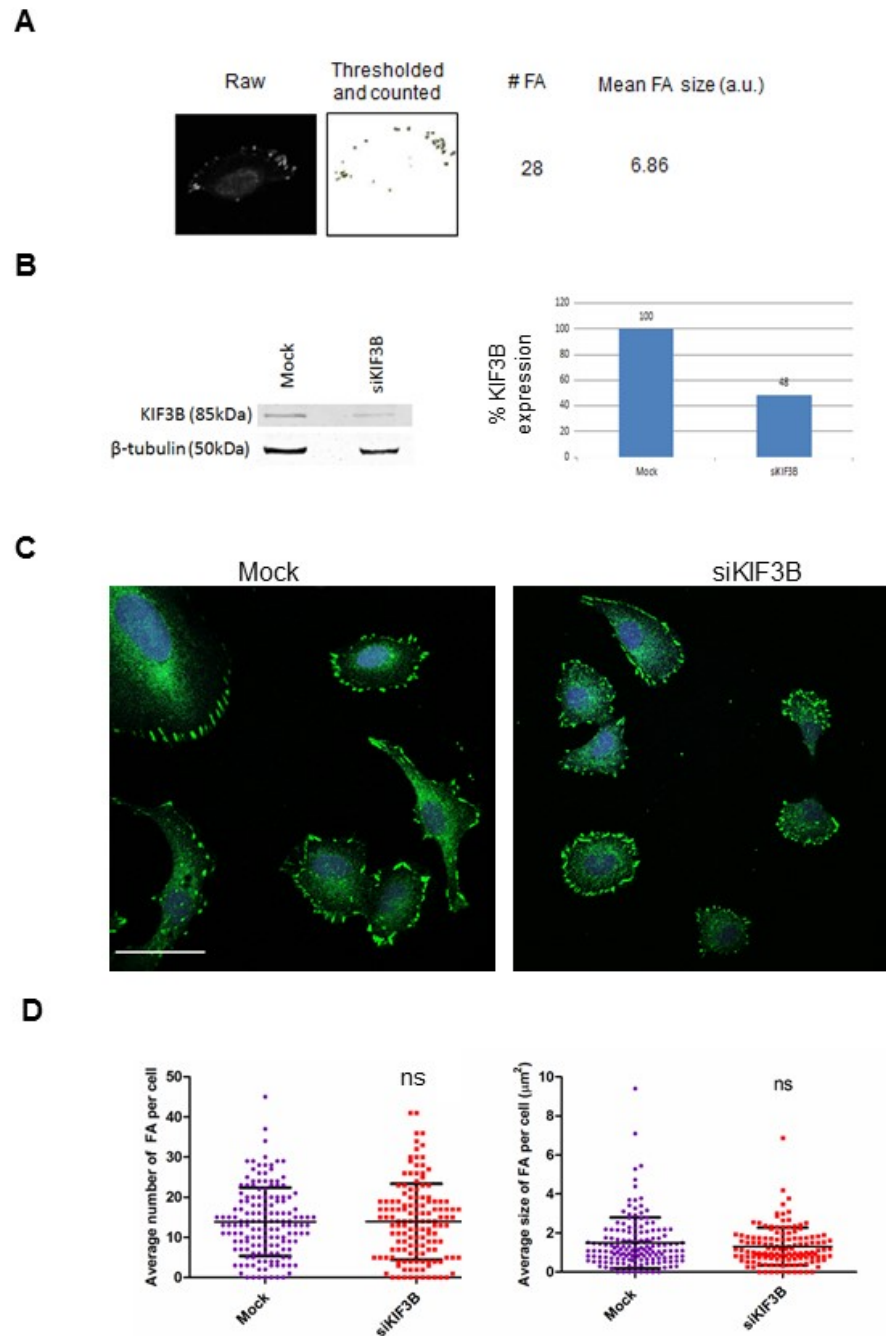
Figure 3-2. KIF3B knockdown does not reduce size or number of focal adhesions

(A) Thresholding with imageJ macro reduces background fluorescence, enabling focal adhesion quantification using ImageJ wand (tracing) tool. (B) Western blot and quantification of KIF3B knockdown of HT1080 cells used for the assay. (C) Representative images of cells immunostained for vinculin. Scale bar represents 50μm. (D) The average number or cross-sectional area of focal adhesions per cell is not reduced by KIF3B knockdown. Data are from one experiment. N>135 cells per group. p>0.05, Two-tailed t-test of mean±SD.

3.3 KIF3B knockdown does not reduce gelatin degradation

To assess the *in vitro* role of KIF3B in invadopodia, a FITC-gelatin degradation assay was used. FITC-conjugated gelatin (a hydrolyzed form of collagen) was deposited onto glass coverslips and cells were seeded on these coverslips for 12 hours. At the end of this time-point, cells were fixed, permeabilized and stained with phalloidin-647 to label F-actin and Hoechst 33342 to label nuclei. Using a confocal microscope, 20 random fields were imaged per group for a total of >110 cells imaged per group. In this assay, degraded gelatin is visualized as black spots on a uniform fluorescent field. Invadopodia are demarcated by the co-localization of their structural (F-actin) and functional components (spots of gelatin degradation) on the FITC-gelatin coverslip.

Gelatin degradation was quantified using software designed in-house. With this software, the area of gelatin degradation is quantified from the FITC channel and is expressed as a function of the cell area in the AlexaFluor-647 channel. After quantifying the 20 fields per group, no statistically significant difference was found between groups ($p > 0.05$), indicating that transient KIF3B knockdown does not reduce gelatin degradation by HT1080 cells (Figure 3-3).
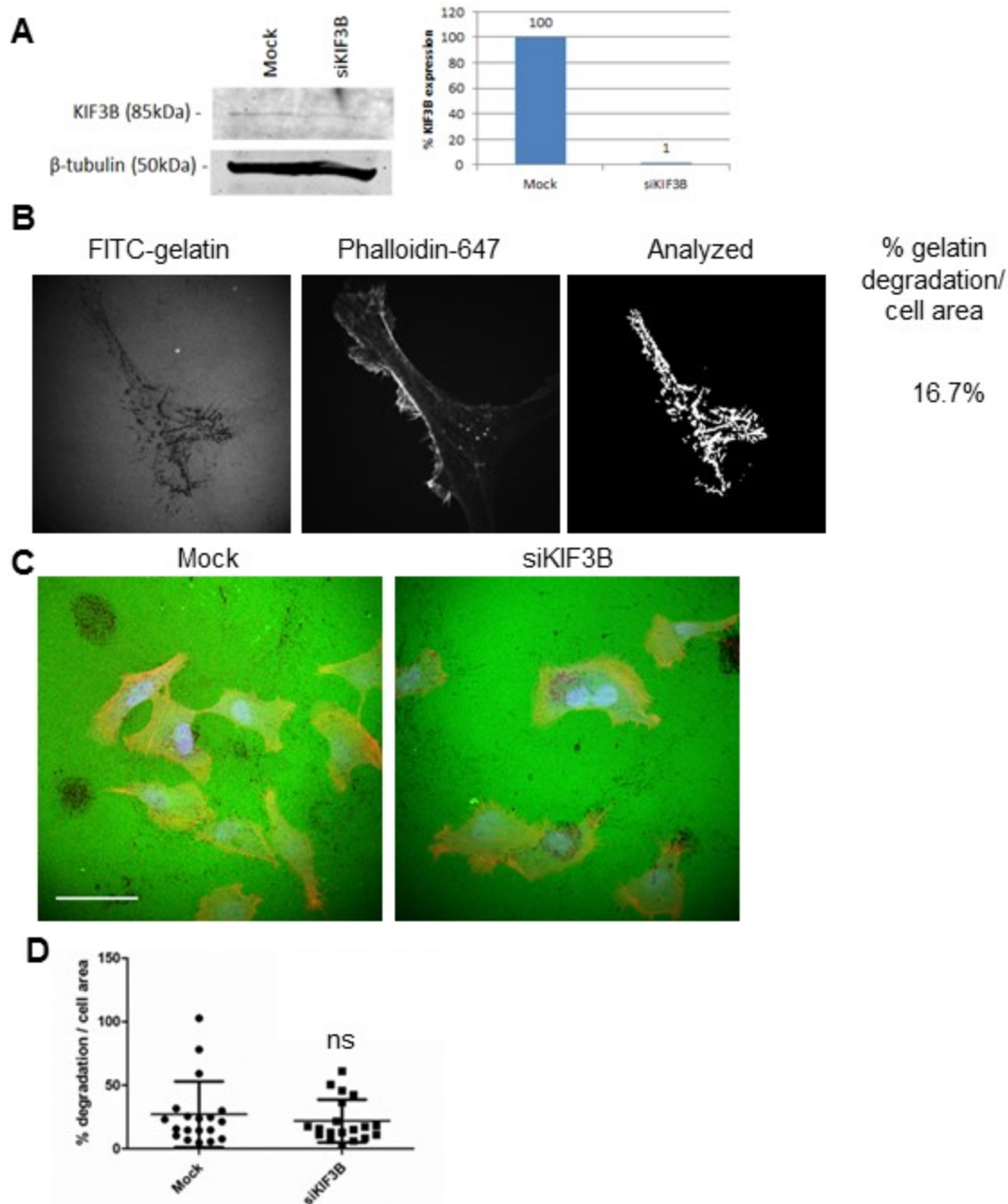
Figure 3-3. KIF3B knockdown does not reduce gelatin degradation
(A) Western blot and quantifications of KIF3B knockdown in HT1080 cells used for the assay. (B) Gelatin degradation is quantified as a function of cell area using custom-designed software. (C) Cells were seeded onto FITC-gelatin coated coverslips for 12 hours, fixed, and stained for F-actin and nuclei. Dark spots on the fluorescent field are areas of degraded gelatin. Scale bar = 50μm. (D) Gelatin degradation expressed as a function of cell area was not reduced following KIF3B knockdown. N=20 fields per group (>110 cells per group). p>0.05, Two-tailed t-test of mean±SD. 3 independent experiments were completed with data from a single representative experiment shown.

3.4 KIF3B knockdown does not reduce cancer cell extravasation in avian embryos

To test the *in vivo* role of KIF3B in invadopodia, I performed an extravasation assay using our shell-less avian embryo model. 14 day-old avian embryos were injected intravenously with HT1080^{Mock} or HT1080^{siKIF3B} cells 48 hours post-transfection. 8 hours later, the embryos were intravenously injected with fluorescent lectin (DyLight 649 lens culinaris agglutinin) to label the vasculature and intravital imaging was performed. Using a confocal microscope, the chorioallantoic membranes of 4 avian embryos were imaged per group. Greater than 125 cells were imaged per embryo. By examining the Z-stack, cells are marked as intravascular or extravascular by determining their position relative to the fluorescently labelled vasculature. After the raw images were blinded I found that while greater than 50 percent of the cancer cells extravasated per group, there was no statistically significant difference between the groups (p>0.05) (Figure 3-4). Taken together, I conclude that transient KIF3B knockdown by siRNA does not inhibit extravasation of HT1080 cells in avian embryos.
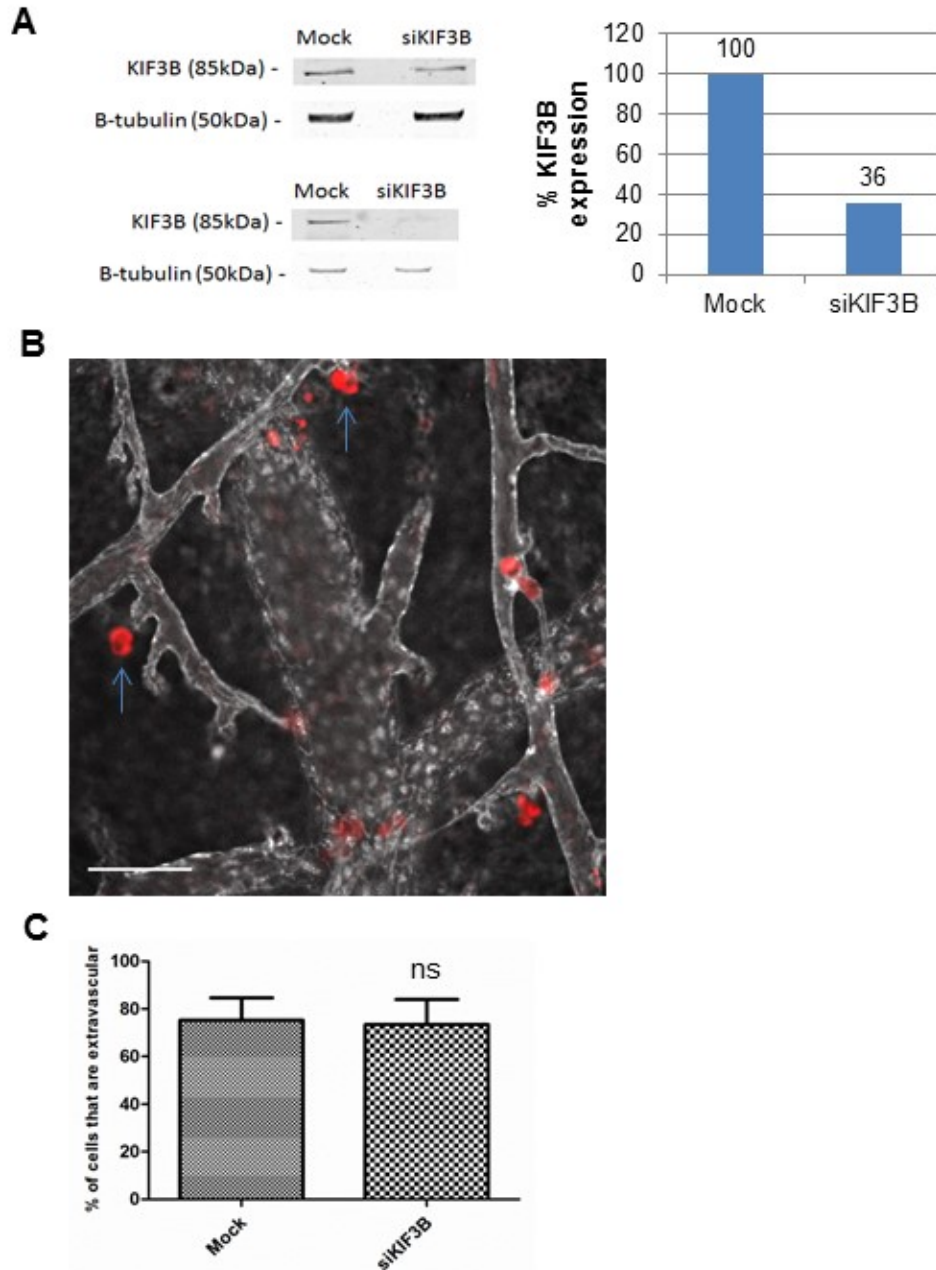
Figure 3-4. KIF3B knockdown does not reduce cancer cell extravasation in avian embryos
(A) Western blot of KIF3B knockdown in HT1080 cells used for the assay. Quantifications represent the average KIF3B knockdown from two separate T175cm² flasks. (B) This representative confocal micrograph shows HT1080 cells (red) that are within the vasculature (white) or in the extravascular stroma (blue arrows). Scale bar represents 100µm. (C) Extravasation efficiency was quantified per embryo as number of extravascular cells divided by total number of cells imaged. KIF3B knockdown did not reduce the percentage of cells that were extravascular. p>0.05, two-tailed t-test of mean±SD. 4 independent experiments were completed with data from a single representative experiment shown.

3.5 KIF3B knockdown does not reduce cell surface localization of MT1-MMP in HT1080 or HEp3 cells

MT1-MMP mediates extracellular matrix degradation when it is present at the cell surface (186). As we found no effect from KIF3B knockdown in our functional MT1-MMP assays, we directly investigated if MT1-MMP cell surface localization is altered in KIF3B knockdown cells. Briefly, cells were seeded into 12 well plates overnight. Cells were then transfected with KIF3B siRNA and collected for western blot and flow cytometry 48 hours post-transfection. Cells were stained with mouse monoclonal anti-MT1-MMP antibody and AlexaFluor secondary antibodies. Cells were then immediately analyzed on a flow cytometer. After gating with the isotype control group, 10,000 single cell events were recorded per sample. In both HEp3 and HT1080 cell lines, detached with TrypLE or 10mM EDTA, it was found that KIF3B knockdown by siRNA did not reduce the cell surface localization of MT1-MMP (data from cells detached with TrypLE shown in Figure 3-5 and Appendix C).
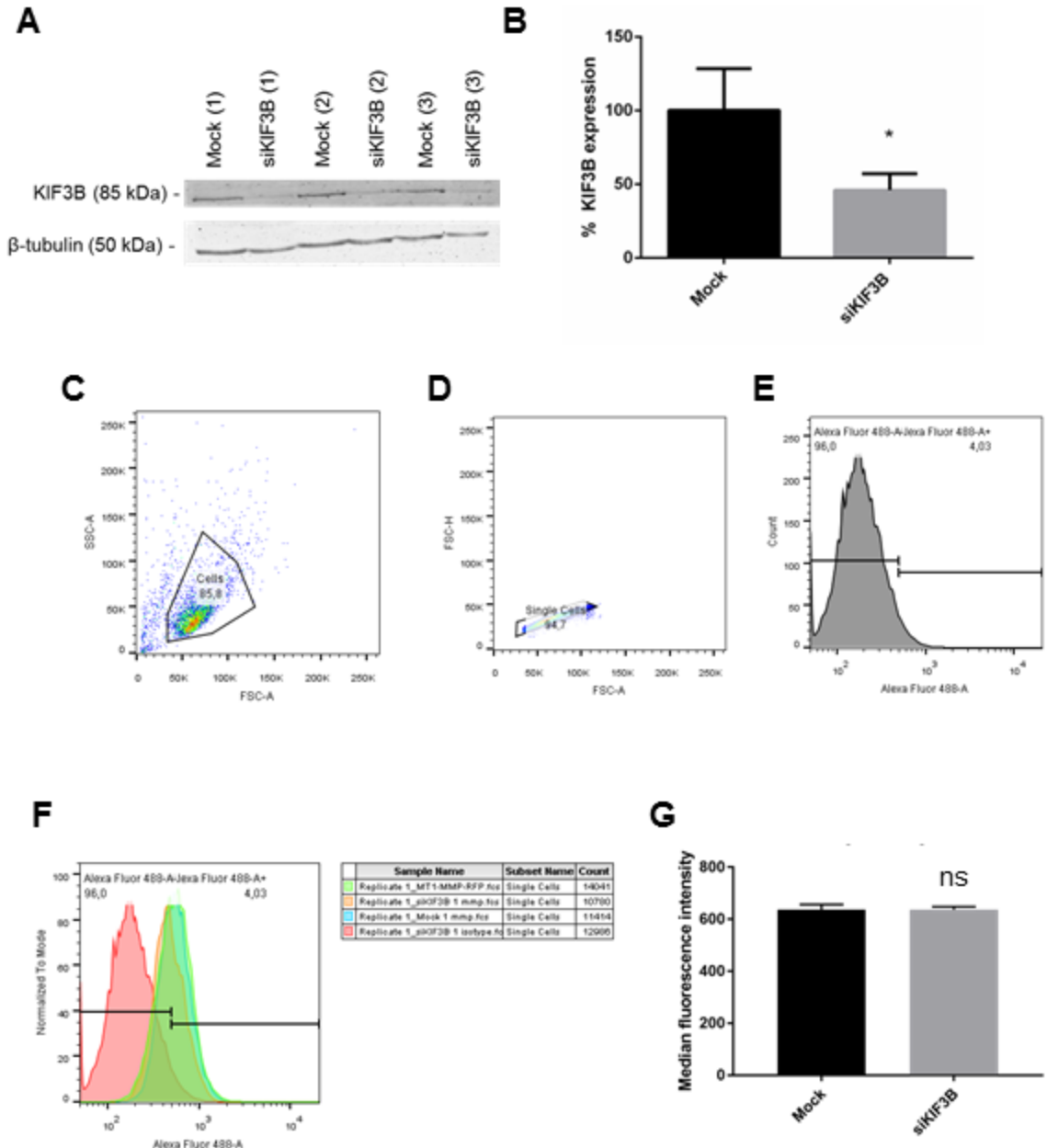
Figure 3-5. KIF3B knockdown by siRNA does not reduce cell surface localization of MT1-MMP in HT1080 cells

(A, B) Western blot and quantifications of KIF3B knockdown in HT1080 cells used for the assay. (C-E) Gating for single cells was completed using unstained cells and PMT voltage was determined using cells stained with isotype control antibody. (F) Histogram of counts versus fluorescence intensity for MT1-MMP staining. (G) Compared to mock transfected cells, KIF3B knockdown did not reduce the median fluorescence intensity for MT1-MMP staining. p>0.05, two-tailed t-test of mean±SD. 2 independent experiments were completed with data from a single representative experiment shown.

3.6 Generation of KIF3B knockout in HT1080 cells using CRISPR-Cas9

To improve upon the moderate levels of KIF3B knockdown we achieved using shRNAs or siRNAs and to create cell lines with stable depletion of KIF3B, we targeted KIF3B for knockout from genomic DNA using the CRISPR-Cas9 system. CRISPR-Cas9 editing creates insertion-deletion (indel) mutations and leads to formation of early stop codons in the target gene, resulting in protein knockout (182). CRISPR-Cas9 plasmids targeting KIF3B for knockout at two different loci were generated and each plasmid was transfected into HT1080 cells. After puromycin selection and expansion of selected cells, genomic DNA and protein lysates were collected from the CRISPR-edited cells for droplet digital PCR and Western blotting, respectively.

In ddPCR, the sample is partitioned into tens of thousands of droplets and each droplet is individually analyzed (187). While qPCR can detect 2-fold changes in gene expression, ddPCR can detect alleles occurring at a frequency of one in thousands within a population (188). Therefore, ddPCR is more sensitive than qPCR for detecting potentially rare gene editing events. ddPCR was performed to determine the frequency of Cas9 editing events in the bulk population of HT1080 cells transfected with pKIF3Bsg2. A fluorescent reference probe was selected to bind outside the Cas9 cut-site to quantify amplification of the KIF3B locus. A fluorescent drop-off probe was selected to bind to the Cas9 target cut site to quantify editing efficiency (Figure 3-6A). In samples where the target sequence is cut and repaired by non-homologous end joining (NHEJ), the drop-off probe will be unable to bind and the sample will be recorded as negative for fluorescence from the drop-off probe (Figure 3-6B). In a clonal population of cells where monoallelic KIF3B knockout is present, half the droplets will be negative for

drop-off probe fluorescence. In a clonal population of cells where biallelic KIF3B

knockout is present, all droplets will be negative for drop-off probe fluorescence.

On the ddPCR plots, a gate (pink) was applied to both groups based on the position of

the droplets from the CRISPR control group. All droplets in the pKIF3Bsg2 group that

were positive for reference probe fluoresce were negative for drop-off probe

fluorescence, based on the applied gate. Therefore, CRISPR-Cas9-editing occurred in

all droplets of genomic DNA from puromycin-selected pKIF3Bsg2-transfected cells

(Figure 3-6C).

To confirm that high levels of Cas9-mediated editing events at the genomic level

correlate with loss of KIF3B at the protein level, Western blotting was performed. No

KIF3B bands were detected in the KIF3Bsg1 and KIF3Bsg2 lanes, suggesting high

levels of knockout were attained in the edited bulk cell populations (Figure 3-6D).
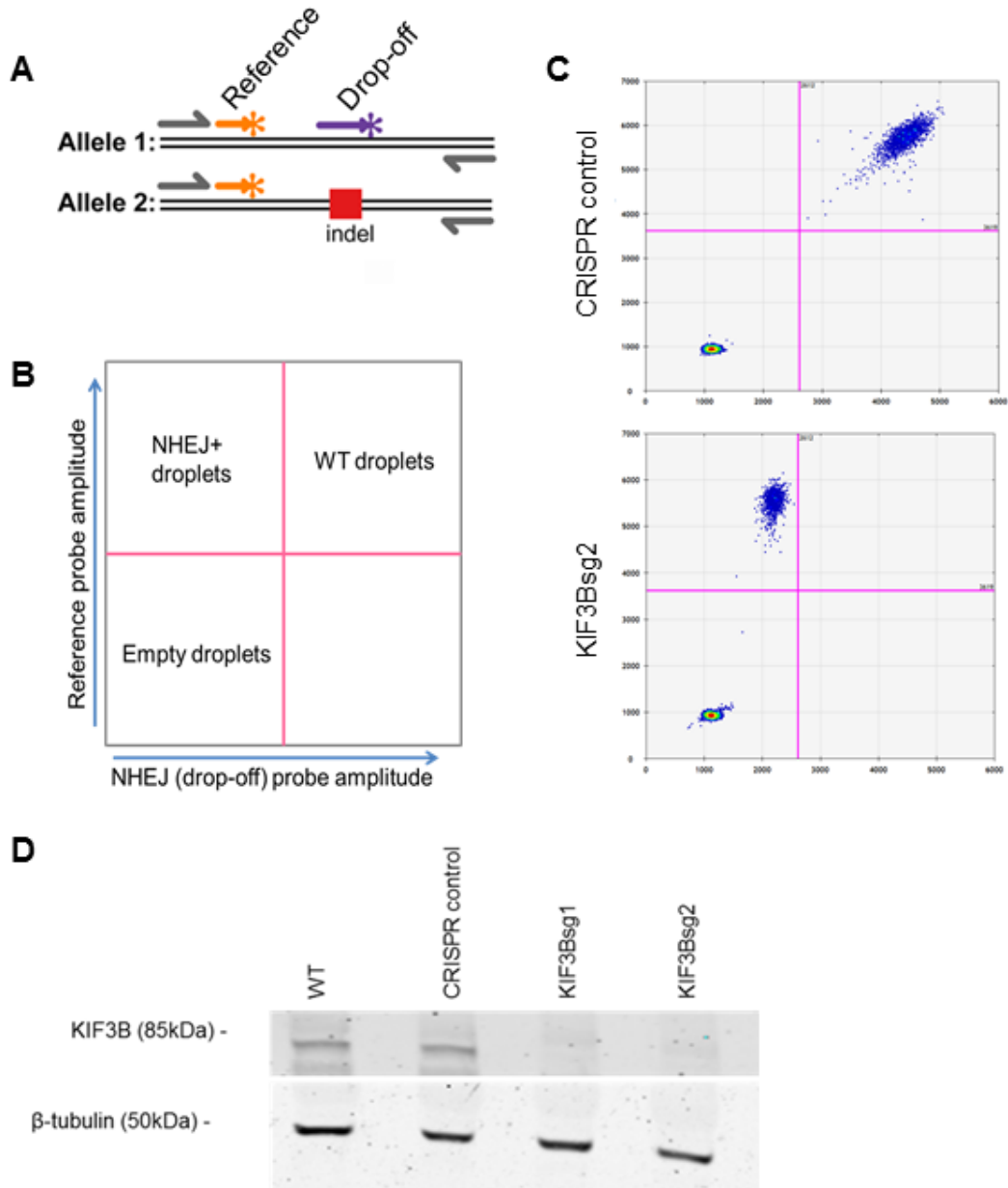
Figure 3-6. Generation of KIF3B knockout in HT1080 cells using CRISPR-Cas9
(A) Two probes were used in droplet digital PCR (ddPCR) to quantify amplification of the KIF3B locus (reference probe) and CRISPR-Cas9 editing events (drop-off probe). Figure adapted from Findlay, Vincent et al. (2016) *PLOS ONE.* (B) ddPCR plots are obtained by plotting probe amplitudes in two dimensions. Droplets containing genomic DNA successfully edited by CRISPR-Cas9 would be positive for reference probe fluorescence (Y-axis) and negative for drop-off probe fluorescence (X-axis). (C) ddPCR plots indicate that CRISPR-Cas9-editing occurred in all droplets of genomic DNA from pKIF3Bsg2-transfected cells. (D) Western blot shows no detectable KIF3B at the protein level in KIF3Bsg1 and KIF3Bsg2 cell populations.

3.7 KIF3B knockout blocks HT080 cell motility *in vivo*

After attaining KIF3B knockout in HT1080 cells using CRISPR-Cas9, we asked if KIF3B knockout reduces cancer cell motility *in vivo.* The HT1080 KIF3B CRISPR knockouts were infected with a lentiviral RFP-vector (pRBOW/FLuc_TagRFP) and selected with blasticidin to produce RFP-positive cells. A metastatic colony formation assay was then performed with the resultant cells. 25,000 cells were injected intravenously into day 10 avian embryos. 5 days post-injection intravital imaging was performed on the embryos (Figure 3-7A). Each embryo was injected with fluorescent lectin to label the vasculature, 5 minutes before imaging. Using confocal microscopy, 30μm Z-stacks were acquired. 3 embryos were imaged per group and 30 colonies per group were analyzed using Compactness Index software. Statistical testing (two-tailed T-test) indicates that the colonies formed by the KIF3B knockouts are significantly more compact than those formed by the control HT1080 cells (Figure 3-7B).
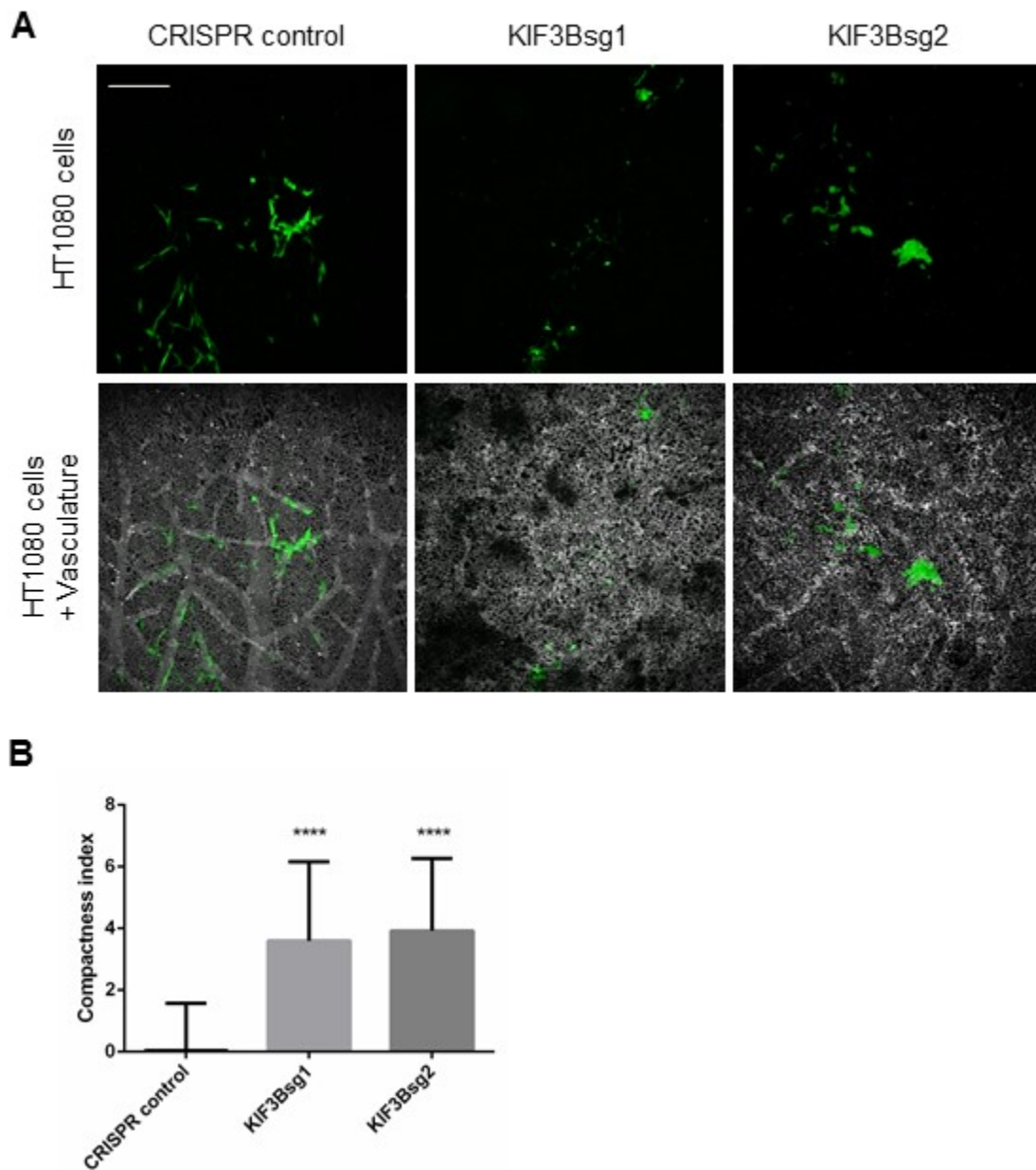
Figure 3-7. KIF3B knockout blocks HT080 cell motility *in vivo*
(A) Developmental day 10 avian embryos were intravenously injected with HT1080
KIF3B CRISPR knockouts and intravitally imaged 5 days post-injection. Shown are
representative confocal micrographs (maximum intensity projections) of metastatic
colonies formed on day 5 post-injection. HT1080 tdTomato cells are false-coloured
green and the lectin-labelled vasculature is white. Scale bar represents 100μm. (B)
Compactness Index quantifications show that compared to CRISPR control, KIF3B
knockout cells form significantly more compact metastatic colonies. Data are from one
experiment. 3 embryos per group, N=30 colonies per group. ****p<0.0001, one way
ANOVA of mean±SD and Dunnett's post-test.

3.8 KIF3B knockout reduces MT1-MMP cell surface localization

Flow cytometry was performed to determine if the compact colony phenotype of the
HT1080 KIF3B CRISPR knockouts can be attributed to altered levels of cell surface
MT1-MMP. MT1-MMP flow cytometry was performed as described above. By one-way
ANOVA and Dunnett's Multiple Comparison Test, a statistically significant difference
($p < 0.05$) was found between the CRISPR control and one of the KIF3B knockouts
(KIF3Bsg1) (Figure 3-8).

Figure 3-8. KIF3B knockout reduces MT1-MMP cell surface localization
Without permeabilization, HT1080 KIF3B knockouts were stained for MT1-MMP and analyzed on a flow cytometer. 10,000 single cell events were recorded per group. (A-C) Gating for single cells was completed using unstained cells and PMT voltage was determined using cells stained with isotype control antibody. (D) Histogram of counts versus fluorescence intensity for MT1-MMP staining. (E) A statistically significant difference was found between the CRISPR control and one of the KIF3B knockouts (KIF3Bsg1) for the median fluorescence intensity of cell surface MT1-MMP staining. Data are from one experiment. N=3 replicates per group. *p<0.05, ***p<0.001, one way ANOVA of mean±SD and Dunnett's post-test.

3.9 Testing panel of custom siRNAs for KIF3B protein silencing

To investigate the targeting of KIF3B to block metastasis, I selected a panel of custom KIF3B siRNAs using online softwares. Only siDirect, BLOCK-iT RNAi designer and RNA wizard softwares provided siRNA sequences before purchase. The top siRNAs generated by RNA wizard had significant homology to off-target mRNAs and were thus eliminated. The top 10 siRNAs generated by BLOCK-iT that were given 5 star ratings for on-target effects by ThermoFisher were then analyzed by BLAST. 4 of these siRNAs were filtered out because they had significant homology to other mRNA sequences. The siRNAs generated by siDirect were ranked into tiers based on the siRNA seed duplex T_m. Three siRNAs were present in the top tier and had seed duplex T_m that were less than 10 °C. Two of these siRNAs were filtered out because by BLAST it was found they had significant homology to other mRNA sequences. Ultimately, 3 custom KIF3B siRNAs that were predicted to have high on-target effects, no off-target effects (by nucleotide BLAST), and targeted 3 different exons in the KIF3B transcript were selected for purchase (Figure 3-9A). 3 additional siRNAs were purchased as positive controls for KIF3B protein knockdown.

To test the potency of the custom KIF3B siRNAs, HT1080 cells were transfected with the respective siRNAs at a final concentration of 80nM. 48 hours post-transfection cell lysates were collected and Western blots were run (Figure 3-9B). By densitometry quantifications, Thermo#1 was determined to be the most potent custom KIF3B siRNA at 80nM (Figure 3-9C).

A

siRNA name	Exon targeted
siKIF3B Thermo #1	2
siKIF3B Thermo #6	5
siKIF3B siDirect #26	6
siKIF3B Wiesner	2
siKIF3B shRNA screen	9

B

C
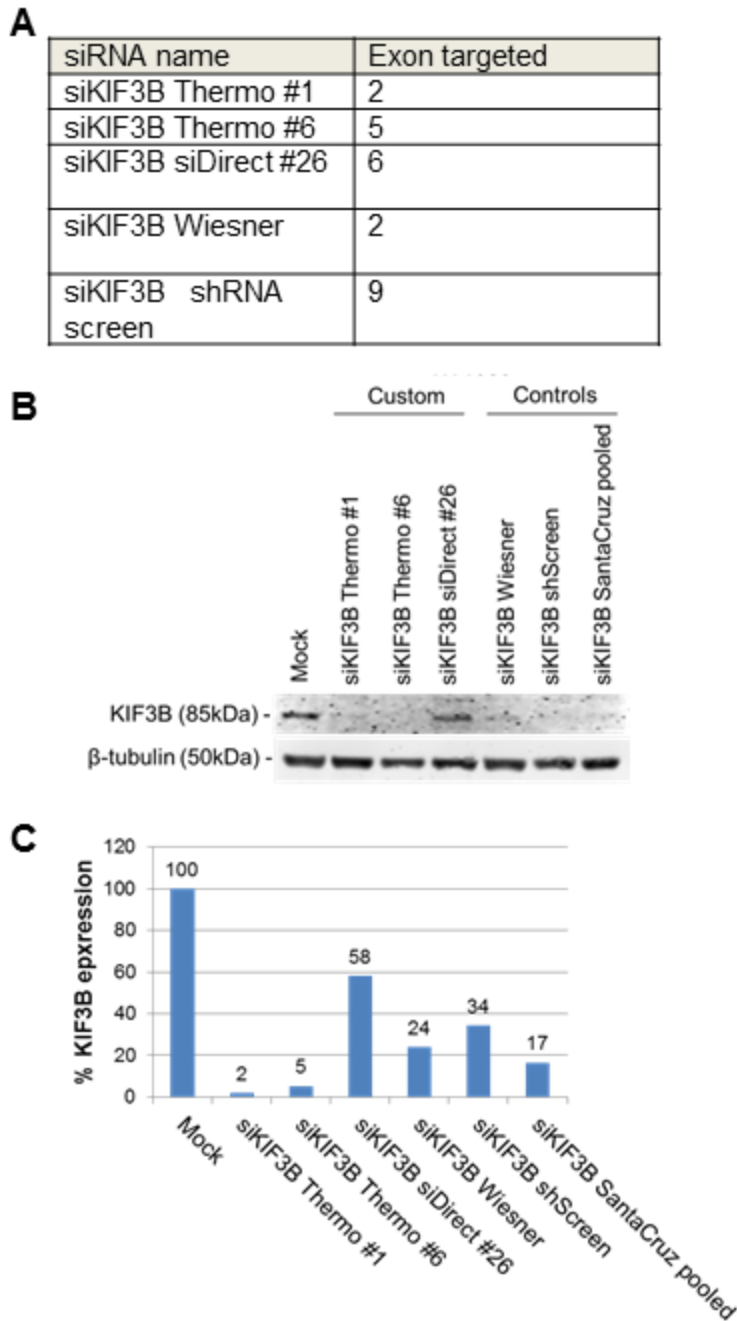
Figure 3-9. Testing panel of custom siRNAs for KIF3B protein silencing
(A) Exons in KIF3B mRNA targeted by custom KIF3B siRNAs. (B) Western blot of KIF3B expression 48 hours after HT1080 cells were transfected with 80nM of the custom-designed KIF3B siRNAs. Three siRNAs were used as positive controls for KIF3B knockdown: 1) KIF3B siRNA used by Wiesner et al. in (139), 2) KIF3B siRNA corresponding to KIF3B shRNA used in *in vivo* motility screen, 3) pool of three KIF3B siRNAs from Santa Cruz used in earlier experiments. (C) Densitometry quantifications of KIF3B knockdown show that siKIF3B Thermo#1 at 80nM is the most potent custom-designed KIF3B siRNA. Data are from one experiment.

3.10 KIF3B knockdown by siRNA is sufficient to block HEp3 cancer cell motility *in vivo*

Thermo#1 was demonstrated to be the most potent KIF3B siRNA *in vitro*. To determine if RNA interference by KIF3B siRNA is sufficient to block cancer cell motility *in vivo,* HEp3 cells were transfected with 80nM siKIF3B Thermo#1 to perform a metastatic colony formation assay (Figure 3-10A). 25,000 KIF3B knockdown cells were injected into developmental day 10 avian embryos, 48 hours-post transfection. Intravital imaging was performed 5 days post-injection (Figure 3-10B). 3 embryos were imaged per group and a total of 30 colonies per group were analyzed using our Compactness Index software. By two-tailed T-test it was found that KIF3B knockdown by siKIF3B Thermo#1 produced significantly more compact colonies than those formed by mock transfected cells (p<0.0001) (Figure 3-10C).
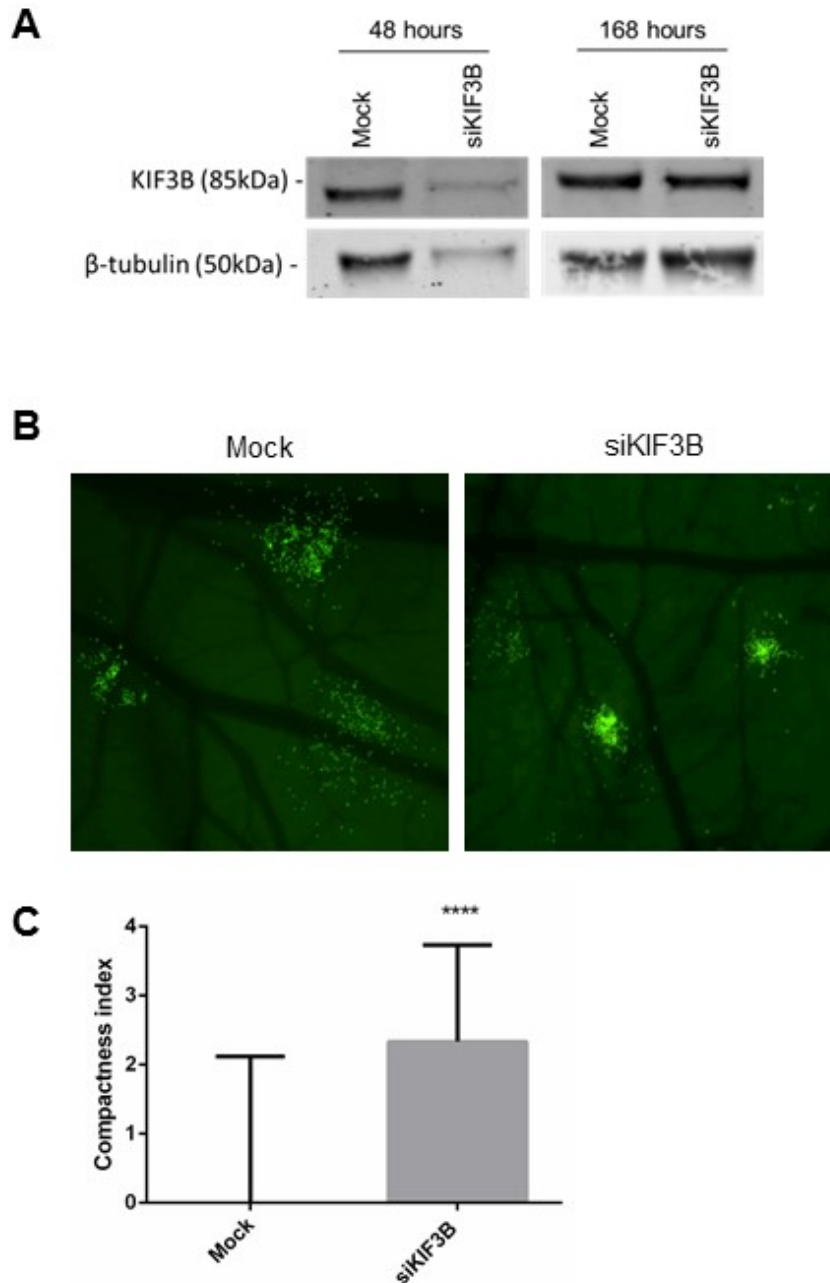
Figure 3-10. KIF3B knockdown by siRNA is sufficient to block HEp3 cancer cell motility *in vivo*

(A) Western blot of KIF3B knockdown in HEp3 cells used for the assay, 48 hours post-transfection (day of injection) and 168 hours post-transfection (day of intravital imaging). (B) Developmental day 10 avian embryos were intravenously injected with HEp3 siKIF3B cells and intravitally imaged 5 days post-injection. Shown are representative images of metastatic colonies formed on day 5 post-injection. (C) Compactness Index quantifications show that compared to mock transfected cells, HEp3 siKIF3B cells form significantly more compact metastatic colonies. Data are from one experiment. 3 embryos per group, N=30 colonies per group. ****p<0.0001, two-tailed t-test of mean±SD.

4   Chapter Four – Discussion

Metastasis is the leading cause of cancer-related deaths and is therefore of special clinical interest (1). Treatments that inhibit growth of the primary tumour do not necessarily block the metastatic spread of cancer, suggesting the biology of these processes is markedly different (175). Currently, therapies that specifically target metastasis are lacking because the complete set of genes controlling this multi-step process are unknown. To this end, our group recently completed a whole human genome cancer cell motility screen using a novel avian embryo intravital imaging platform (7, 13-22). We identified 9 novel genes whose independent knockdown led to an inhibition of cancer cell motility in the avian embryo chorioallantoic membrane (CAM). Quantitative analysis of screen hits showed that shRNA knockdown of KIF3B produced the most potent inhibition of cancer cell motility *in vivo.*

To validate that the inhibition of cancer cell motility was due to specific depletion of KIF3B and not an off-target effect of lentiviral transduction, we created a new HEp3 stable KIF3B knockdown cell line using an independent shRNA. Using high-resolution time-lapse microscopy we showed that KIF3B is required for productive migration of cancer cells in metastatic colonies and is required for migration out of the primary tumour in the avian embryo CAM. Furthermore, in a xenograft murine model, KIF3B knockdown reduced HEp3 metastasis to the lung by over 99%. Using publically available patient datasets, we found that KIF3B is significantly upregulated in the invasive zone of primary tumours and is significantly upregulated in metastases compared to primary tumours in patient-matched samples of several cancer types. These clinical data show that KIF3B expression correlates with invasive and metastatic behavior of cancers and that KIF3B is relevant in human cancer metastasis.

In our current study, we investigated the molecular mechanisms of KIF3B in cancer cell migration and metastasis, and the targeting of KIF3B to block metastasis. Using shRNA knockdown, we showed that KIF3B is required for the motility of HT1080 cancer cells in the avian embryo CAM, demonstrating that KIF3B is required for migration of different types of human cancer cell lines.

To test our hypothesis that KIF3B transports key molecules necessary for focal assembly, we performed vinculin immunostaining in HT1080 cells. The size of focal adhesions is related to migration speed by a Gaussian distribution (94). We found that KIF3B depletion by siRNA did not reduce the average size (mock $1.5\pm0.1\mu m^2$ versus siKIF3B $1.3\pm0.1\mu m^2$) or number (mock 13.9 ± 0.7 vs siKIF3B 13.9 ± 0.8) of focal adhesions per cell. The average size of focal adhesions in our experiment was comparable to the average size of focal adhesions in wild-type HT1080 cells ($1.1\mu m^2$) in a study by Kim and Wirtz (94). As stiffness of the underlying substrate is known to influence the size of focal adhesions, this may explain the difference in average size of focal adhesions between the studies (91). In our study we grew HT1080 cells on fibronectin-coated glass coverslips whereas Kim and Wirtz grew them on a soft polyacrylamide substrate.

A limitation of our experiment is that the size of focal adhesions was not studied in the context of cell migration. Our group has already shown that KIF3B is required for the migration of HEp3, PC3, and MDA-MB-231 cell *in vitro.* While the size of focal adhesions may not have differed at the population level in our experiment with HT1080 siKIF3B cells, it is possible that the size of focal adhesions may be altered in the polarized, migrating sub-population of cells. Because KIF3B is a molecular motor, it is relevant to examine if the dynamics (assembly, maturation, disassembly) at focal adhesions are altered in KIF3B knockdown cells by performing fluorescence recovery after photobleaching (FRAP) experiments on fluorescent fusions of focal adhesion proteins.

As the related kinesin KIF1C has been shown to transport α5β1 integrin which binds fibronectin, the dynamics of β1 integrin trafficking in KIF3B knockdown cells should be explored (100, 189).

We investigated the role of KIF3B in invadopodia using two functional assays. The high resolution of the FITC-gelatin degradation assay permits the visualization of matrix degradation by sub-cellular structures (invadopodia) as opposed to the invasive behavior of whole cells assessed using other invasion assays (190). The extravasation assay evaluates the ability of cells to transmigrate through the vasculature of the CAM into the stroma by degradation of the sub-endothelial basement membrane (120, 191). In the FITC-gelatin degradation assay, we found that KIF3B knockdown by siRNA did not reduce the area of degraded gelatin as a function of cell area per imaged field. Optimization of cell incubation time on the FITC-gelatin was critical. Even for the highly invasive HT1080 cancer cell line, 12 hours of incubation was required to degrade our preparation of the matrix. Our group recently showed that invadopodia are required for extravasation and that extravasation is a rate-limiting step in the metastatic cascade (120). As our group previously showed that KIF3B is required for spontaneous metastasis in mice, we asked if KIF3B regulates the extravasation step of metastasis via invadopodium formation. I completed four independent extravasation assays, performing intravital imaging 5 hours or 8 hour post-injection, using day 15 avian embryos or day 14 embryos, which are more permissive to extravasating cells. In all cases, I found that KIF3B knockdown did not reduce the fraction of cells that were found in the extravascular stroma.

As we found that KIF3B did not regulate the function of MT1-MMP in invadopodia, we examined if KIF3B is required for the direct trafficking of MT1-MMP to the plasma membrane. We performed flow cytometry against cell surface MT1-MMP in HEp3 and

HT1080 cells detached with TrypLE Express or ethylenediaminetetraacetic acid (EDTA).
TrypLE Express is an enzyme-based cell-dissociating reagent that is marketed as a
gentler dissociating agent than porcine trypsin for preserving cell surface epitopes (192).
We observed in both HEp3 cells and HT1080 cells detached with TrypLE express that
KIF3B knockdown by siRNA did not reduce the cell surface localization of MT1-MMP.
However, to account for the possibility that MT1-MMP was cleaved off the cell surface by
TrypLE express, we repeated the flow cytometry assay by detaching the cells with
10mM EDTA and found no statistically significant difference in the cell surface
localization of MT1-MMP in mock- and siKIF3B-transfected cells.

To increase depletion of KIF3B, we created two KIF3B CRISPR knockouts in the
HT1080 cell line. We showed through the metastatic colony formation assay that KIF3B
knockout is sufficient to inhibit HT1080 cancer cell motility *in vivo*. Interestingly, when we
performed MT1-MMP flow cytometry on the KIF3B knockout cell lines detached with
EDTA, we observed a statistically significant difference in cell surface localization of
MT1-MMP in one of the KIF3B knockouts compared to the CRISPR control. MT1-MMP
flow cytometry with the KIF3B knockouts must be repeated to confirm this finding.

An MT1-MMP siRNA-treated group was added as a control for MT1-MMP flow cytometry
of the KIF3B knockouts. The median fluorescence intensity (MFI) value of the CRISPR
control group was 1021 and was 810 for the siMT1-MMP group. A 20% difference in MFI
between the groups with highest and lowest expected MT1-MMP cell surface expression
suggests a small dynamic range for the assay. Level of MT1-MMP knockdown must be
determined to confirm this assertion. However, the similarly small change in MT1-MMP
cell surface localization observed in earlier experiments using MT1-MMP-RFP
overexpressing cells as a control adds support to the assertion. A small dynamic range

in the flow assay may mean biological differences in MT1-MMP cell surface localization go undetected.

A potential explanation for the low dynamic range in the MT1-MMP flow cytometry assay is the accumulation of dead cells. Dead cells become permeable and can bind non-specifically to antibodies, leading to false positive results (193). Chemical fixation of cells before immunostaining can preserve the integrity of the plasma membrane while potentially altering epitopes of cell surface proteins (194). For this reason, we chose to perform flow cytometry analysis without fixing cells. However, this may have resulted in the accumulation of dead cells. We used the same anti-MT1-MMP antibody (LEM-2/15.8) as Wiesner et al. who without fixing cells showed that KIF3B knockdown alters cell surface localization of MT1-MMP in primary human macrophages (139). In contrast, Eisenach et al. successfully studied the trafficking of MT1-MMP by fixing MCF-7 cancer cells with 4% paraformaldehyde in 5mM EDTA/PBS before staining with LEM-2/15.8 (195). Ultimately the decision to fix cells or not may be dictated by technical considerations (number of samples to prepare or time to access flow cytometer) or the lability of the cell type.

In our flow cytometry studies, a statistically significant reduction of cell surface MT1-MMP was seen with a KIF3B knockout cell line but not when KIF3B was transiently knocked down with siRNA. This raises the possibility that level of KIF3B knockdown was a limitation in our study. Two independent KIF3B shRNAs were used to knockdown KIF3B in our motility screen, achieving knockdown of >70%. For our study on the molecular mechanisms of KIF3B in cell migration and metastasis, we used a pooled siRNA to knockdown KIF3B as new stable knockdown cell lines created with the original shRNAs had no greater than 50% knockdown. Using siRNA to knockdown KIF3B, we typically saw 50-60% protein knockdown in cells used for experiments but have seen

knockdown greater than 90% as was seen while testing the panel of custom KIF3B siRNAs. The variability in KIF3B knockdown by siRNA may be attributed to small changes in cell confluency or temperature of media at time of transfection as all other variables were controlled between experiments (using low passage (<10) cells, same concentration of siRNA, preparing transfection complexes in the same way). To achieve >80% knockdown of KIF3B in their study, Wiesner et al. transfected primary human macrophages twice with siRNA, at 0 and 48 hours then used the cells for experiments 18 hours later (139). This approach can be adopted in future studies using KIF3B siRNAs.

In a proof of concept experiment, we demonstrated that KIF3B knockdown by siRNA blocks HEp3 cancer cell motility in the avian embryo chorioallantoic membrane. This finding is exciting as it is the first demonstration that genes identified in our shRNA motility screen can be targeted with exogenous molecules to inhibit cancer cell motility *in vivo*. While the level of KIF3B knockdown was low in the targeting experiment (<50%), the inhibition of cell motility validates that siRNAs are a satisfactory means of studying KIF3B function in cancer cells. However, in this experiment the colonies that formed in the HEp3 siKIF3B group were visually less compact than those that formed in HEp3 shKIF3B cells in the motility screen. The Compactness Index values corroborate these differences in the phenotype of HEp3 siKIF3B (C.I.=2.4) and HEp3 shKIF3B colonies (C.I.=12.4). Western blots show by 168 hours post-transfection when embryos were intravitally imaged, the level of KIF3B knockdown had fallen compared to 48 hours post-transfection. This may explain why siKIF3B colonies were not as compact as shKIF3B colonies.

Several experiments must be conducted to further characterize the custom KIF3B siRNAs we selected. We tested the custom KIF3B siRNAs at 80nM, the same

concentration we used in previous experiments with the pooled KIF3B siRNAs. The custom KIF3B siRNAs should be tested at lower concentrations in multiple cell lines to determine the minimum effective concentration of KIF3B siRNA that yields >70% knockdown of KIF3B at the protein level. These studies may differentiate the three custom KIF3B siRNAs based on potency at concentrations lower than 80nM. We have shown that different cancer cell lines express different baseline levels of KIF3B (Appendix D) which may affect the minimum effective concentration of KIF3B siRNA. The objective to create a biocompatible lipid nanoparticle to deliver KIF3B siRNAs can be pursued after the lead KIF3B siRNA has been determined. This objective is feasible as our group has extensive experience with the encapsulation of other nucleic acids (plasmid DNA) for systemic delivery in murine models of cancer and has shown these treatments are well tolerated.

While metastasis is known to be the leading cause of cancer-related death, no study has directly investigated if the prevention of metastasis can prolong survival. A future goal would be to address this question using a xenograft murine model of spontaneous metastasis to the lungs. After a primary tumour is palpable, it can be surgically resected and mice can be given adjuvant chemotherapy and intravenous injections of siKIF3B LNPs. Luciferase imaging would be performed to determine if subsequent metastasis to the lungs is blocked. The cohort of mice would be followed to determine if this proposed anti-metastatic therapy provides a survival benefit when compared to mice treated with chemotherapy alone following surgical resection of the primary tumour.

While the focus of our study has been on the role of KIF3B in cell migration and metastasis, it is likely that KIF3A is also required for these processes. KIF3A was present as a hit in our shRNA screen suggesting it may be required for *in vivo* motility but was present within a clone containing multiple shRNAs and therefore was not

investigated further. In Wiesner et al.'s study, they showed that knockdown of either KIF3A or KIF3B blocked cell surface localization of MT1-MMP and matrix degradation in primary human macrophages (139). In 1998 Nonaka et al. showed that KIF3B is required for nodal flow of extraembryonic fluid in mice. In a follow-up to their study, Takeda et al. also showed that KIF3A is required for nodal flow (74, 196). Therefore, it is likely that knockdown of either of the motor subunits of the KIF3 motor is sufficient to inhibit cancer cell motility *in vivo*.

Future directions

Taken together, our findings from experiments using different methods to deplete KIF3B suggest that the level of KIF3B knockdown affects the metastatic colony phenotype *in vivo.* Low levels of KIF3B protein knockdown (<50%) with siRNA in HEp3 cells produced partially compact metastatic colonies and moderate levels of KIF3B knockdown (>70%) by shRNA in HEp3 cells produced colonies that were highly compact. Therefore, it will be important to establish the level of KIF3B knockdown that is required to produce a phenotype in mechanism studies. This level of knockdown could then be set as the standard required in all future studies on KIF3B. siRNA knockdown will remain the preferred model to study the therapeutic targeting of KIF3B whereas from a technical standpoint shRNA knockdown or CRISPR knockouts are the preferred models to study the molecular mechanisms of KIF3B because they produce stable gene depletion.

Given Wiesner et al.'s findings on KIF3B in primary human macrophages, it was surprising that KIF3B knockdown in HT1080 cells did not reduce invadopodia-mediated matrix degradation or extravasation (139). Assuming that the level of KIF3B knockdown was sufficient to produce a phenotype in these experiments, it suggests that KIF3B does not regulate protease-dependent cell migration in cancer cells. To explain the compact

colony phenotype produced in HEp3 and HT1080 shKIF3B cells, it is possible that KIF3B regulates protease-independent cell migration. Keil et al. have shown that KIF3B knockdown reduced RhoA activation in cells undergoing cytokinesis (197). RhoA, a Rho GTPase, mediates membrane protrusion and contraction to facilitate cell migration (198). Recently, Robertson demonstrated that RhoA depletion reduced the productive migration of individual cells in micrometastases formed by HEp3 cells in the avian embryo CAM (199). Therefore, KIF3B-regulation of RhoA to promote cancer cell motility is an attractive hypothesis to explore. RhoA activity can be assessed in several ways. Level of active GTP-bound RhoA can be directly measured by Western blot or indirectly through pulldown of the RhoA effector proteins ROCK1 and ROCK2 .The function of RhoA in actin stress fiber assembly can also be assessed through fluorescence microscopy.

The role of KIF3B in the Wnt pathway is another possible mechanism to explore. Extensively researched in the context of cancer, the Wnt pathway is classically associated with maintenance of cancer stemness but has also been shown to be involved in cell migration via EMT (200, 201). Two reports describe conflicting roles for the KIF3 motor in Wnt-mediated cell migration. Through KAP3, KIF3A/B has been shown to transport APC to membrane protrusions in MDCK cells. Cells transfected with a dominant negative version of KAP3 had increased cell migration, suggesting the KIF3 motor suppresses migration in this context (202). Conversely, Liu et al. reported that KIF3A expression is increased in patient samples of advanced prostate cancer and that KIF3A is required for invasion of LNCaP prostate cancer cells through Matrigel-coated Transwell filters (203). It will be interesting to resolve the role of KIF3B in Wnt signalling in the context of our motility studies using HEp3 and HT1080 cell lines. A reporter for the TCF/LEF family of transcription factors can be transfected into control and KIF3B

knockdown cells to obtain a readout for the activity of the Wnt pathway in these cells (204).

Lastly, an unbiased approach may provide new insights on the molecular mechanisms of KIF3B in cell migration and metastasis. The report that KIF3B directs endocytosed proteins to recycling endosomes suggests that KIF3B regulates the trafficking of proteins to the plasma membrane (70). To identify proteins transported by KIF3B to the plasma membrane, a biotinylation assay can be performed (205): Cell surface proteins are conjugated with biotin, a peptide that binds to lysine residues. Cells are then lysed and biotinylated proteins are purified through strong interactions with avidin. Mass spectrometry can then be used to identify proteins that are absent in the plasma membrane of cells depleted of KIF3B.

Through our study, we have developed novel tools and optimized assays to study the role of KIF3B in cancer cell migration and metastasis. We have also demonstrated that KIF3B can be targeted with siRNA to block cancer cell motility *in vivo*. Ultimately, continuation of this study may identify the molecular mechanisms of KIF3B in cancer cell migration and metastasis and lead to the development of specific anti-metastatic therapies.

References

1. Mehlen P, Puisieux A. Metastasis: a question of life or death. Nat Rev Cancer. 2006 Jun;6(6):449-58.

2. Valastyan S, Weinberg RA. Tumor Metastasis: Molecular Insights and Evolving Paradigms. Cell. 2011 -10-14;147(2):275-92.

3. Chambers AF, Groom AC, MacDonald IC. Dissemination and growth of cancer cells in metastatic sites. Nat Rev Cancer. 2002 Aug;2(8):563-72.

4. Ambrus JL, Ambrus CM, Mink IB, Pickren JW. Causes of death in cancer patients. J Med. 1975;6(1):61-4.

5. Entschladen F, Thyssen DA, Drell DW. Re-Use of Established Drugs for Anti-Metastatic Indications. Cells. 2016 -1-12;5(1).

6. Eccles SA, Welch DR. Metastasis: recent discoveries and novel treatment strategies. Lancet. 2007 19 May;369(9574):1742.

7. Kain KH, Miller JWI, Jones-Paris CR, Thomason RT, Lewis JD, Bader DM, et al. The chick embryo as an expanding experimental model for cancer and cardiovascular research. Dev Dyn. 2014 -2;243(2):216-28.

8. Deryugina EI, Quigley JP. Chick embryo chorioallantoic membrane model systems to study and visualize human tumor cell metastasis. Histochem Cell Biol. 2008 -12;130(6):1119-30.

9. Zijlstra A, Lewis JD. Visualization and Quantification of De Novo Angiogenesis in Ex Ovo Chicken Embryos. In: Zudaire E, Cuttitta F, editors. The Textbook of Angiogenesis and Lymphangiogenesis: Methods and Applications. Springer Netherlands; 2012. p. 217-40.

10. Price JE. Spontaneous and experimental metastasis models: nude mice. Methods Mol Biol. 2014;1070:223-33.

11. Khanna C, Hunter K. Modeling metastasis in vivo. Carcinogenesis. 2005 Mar;26(3):513-23.

12. Fidler IJ. Models for spontaneous metastasis. Cancer Res. 2006 Oct 01,;66(19):9787.

13. Leong HS, Chambers AF, Lewis JD. Assessing cancer cell migration and metastatic growth in vivo in the chick embryo using fluorescence intravital imaging. Methods Mol Biol. 2012;872:1-14.

14. Arpaia E, Blaser H, Quintela-Fandino M, Duncan G, Leong HS, Ablack A, et al. The interaction between caveolin-1 and Rho-GTPases promotes metastasis by controlling

the expression of alpha5-integrin and the activation of Src, Ras and Erk. Oncogene. 2012 Feb 16,;31(7):884-96.

15. Goulet B, Kennette W, Ablack A, Postenka CO, Hague MN, Mymryk JS, et al. Nuclear localization of maspin is essential for its inhibition of tumor growth and metastasis. Lab Invest. 2011 Aug;91(8):1181-7.

16. Pink DBS, Schulte W, Parseghian MH, Zijlstra A, Lewis JD. Real-time visualization and quantitation of vascular permeability in vivo: implications for drug delivery. PLoS ONE. 2012;7(3):e33760.

17. Steinmetz NF, Ablack AL, Hickey JL, Ablack J, Manocha B, Mymryk JS, et al. Intravital imaging of human prostate cancer using viral nanoparticles targeted to gastrin-releasing Peptide receptors. Small. 2011 Jun 20,;7(12):1664-72.

18. Leong HS, Steinmetz NF, Ablack A, Destito G, Zijlstra A, Stuhlmann H, et al. Intravital imaging of embryonic and tumor neovasculature using viral nanoparticles. Nat Protoc. 2010 Aug;5(8):1406-17.

19. Cho C, Ablack A, Leong H, Zijlstra A, Lewis J. Evaluation of nanoparticle uptake in tumors in real time using intravital imaging. J Vis Exp. 2011 Jun 21,(52).

20. Lewis JD, Destito G, Zijlstra A, Gonzalez MJ, Quigley JP, Manchester M, et al. Viral nanoparticles as tools for intravital vascular imaging. Nat Med. 2006 Mar;12(3):354-60.

21. Zhang Y, Schulte W, Pink D, Phipps K, Zijlstra A, Lewis JD, et al. Sensitivity of cancer cells to truncated diphtheria toxin. PLoS ONE. 2010 May 05,;5(5):e10498.

22. Cho C, Shukla S, Simpson EJ, Steinmetz NF, Luyt LG, Lewis JD. Molecular targeted viral nanoparticles as tools for imaging cancer. Methods Mol Biol. 2014;1108:211-30.

23. Testa JE, Brooks PC, Lin JM, Quigley JP. Eukaryotic expression cloning with an antimetastatic monoclonal antibody identifies a tetraspanin (PETA-3/CD151) as an effector of human tumor cell migration and metastasis. Cancer Res. 1999 Aug 01,;59(15):3812-20.

24. Zijlstra A, Lewis J, Degryse B, Stuhlmann H, Quigley JP. The inhibition of tumor cell intravasation and subsequent metastasis via regulation of in vivo tumor cell motility by the tetraspanin CD151. Cancer Cell. 2008 March;13(3):221-34.

25. Zijlstra A, Mellor R, Panzarella G, Aimes RT, Hooper JD, Marchenko ND, et al. A quantitative analysis of rate-limiting steps in the metastatic cascade using human-specific real-time polymerase chain reaction. Cancer Res. 2002 Dec 01,;62(23):7083-92.

26. Ashby WJ, Wikswo JP, Zijlstra A. Magnetically attachable stencils and the non-destructive analysis of the contribution made by the underlying matrix to cell migration. Biomaterials. 2012 Nov;33(33):8189-203.

27. Cellular Organization [Internet]. [cited 2017 March 7]. Available from: http://medcell.med.yale.edu/lectures/cellular_organization.php.

28. Vale RD. Intracellular transport using microtubule-based motors. Annu Rev Cell Biol. 1987;3:347-78.

29. Gelfand VI, Bershadsky AD. Microtubule dynamics: mechanism, regulation, and function. Annu Rev Cell Biol. 1991;7:93-116.

30. Valiron O, Caudron N, Job D. Microtubule dynamics. Cell Mol Life Sci. 2001 Dec;58(14):2069-84.

31. van der Vaart B, Akhmanova A, Straube A. Regulation of microtubule dynamic instability. Biochem Soc Trans. 2009 Oct;37(Pt 5):1007-13.

32. Holy TE, Leibler S. Dynamic instability of microtubules as an efficient way to search in space. Proc Natl Acad Sci U S A. 1994 Jun 07,;91(12):5682-5.

33. Burbank KS, Mitchison TJ. Microtubule dynamic instability. Curr Biol. 2006 Jul 25,;16(14):516.

34. Becker W. The World of the Cell. 7th ed. San Francisco: Benjamin Cummings; 2008.

35. Lüders J, Stearns T. Microtubule-organizing centres: a re-evaluation. Nat Rev Mol Cell Biol. 2007 Feb;8(2):161-7.

36. Khodjakov A, Cole RW, Oakley BR, Rieder CL. Centrosome-independent mitotic spindle formation in vertebrates. Curr Biol. 2000 Jan 27,;10(2):59-67.

37. Oakley BR, Oakley CE, Yoon Y, Jung MK. Gamma-tubulin is a component of the spindle pole body that is essential for microtubule function in Aspergillus nidulans. Cell. 1990 Jun 29,;61(7):1289-301.

38. Ross JL, Shuman H, Holzbaur ELF, Goldman YE. Kinesin and dynein-dynactin at intersecting microtubules: motor density affects dynein function. Biophys J. 2008 Apr 15,;94(8):3115-25.

39. Verhey KJ, Kaul N, Soppina V. Kinesin assembly and movement in cells. Annu Rev Biophys. 2011;40:267-88.

40. Hirokawa N. Kinesin and dynein superfamily proteins and the mechanism of organelle transport. Science. 1998 Jan 23,;279(5350):519-26.

41. Hirokawa N, Noda Y, Tanaka Y, Niwa S. Kinesin superfamily motor proteins and intracellular transport. Nat Rev Mol Cell Biol. 2009 Oct;10(10):682-96.

42. Miki H, Okada Y, Hirokawa N. Analysis of the kinesin superfamily: insights into structure and function. Trends Cell Biol. 2005 Sep;15(9):467-76.

43. Rice S, Lin AW, Safer D, Hart CL, Naber N, Carragher BO, et al. A structural change in the kinesin motor protein that drives motility. Nature. 1999 Dec 16,;402(6763):778-84.

44. Vale RD, Milligan RA. The way things move: looking under the hood of molecular motor proteins. Science. 2000 Apr 07,;288(5463):88-95.

45. Hirokawa N, Noda Y. Intracellular transport and kinesin superfamily proteins, KIFs: structure, function, and dynamics. Physiol Rev. 2008 Jul;88(3):1089-118.

46. Wang X, Schwarz TL. The mechanism of Ca2+ -dependent regulation of kinesin-mediated mitochondrial motility. Cell. 2009 Jan 09,;136(1):163-74.

47. Niwa S, Tanaka Y, Hirokawa N. KIF1Bbeta- and KIF1A-mediated axonal transport of presynaptic regulator Rab3 occurs in a GTP-dependent manner through DENN/MADD. Nat Cell Biol. 2008 Nov;10(11):1269-79.

48. Stock MF, Guerrero J, Cobb B, Eggers CT, Huang TG, Li X, et al. Formation of the compact conformer of kinesin requires a COOH-terminal heavy chain domain and inhibits microtubule-stimulated ATPase activity. J Biol Chem. 1999 May 21,;274(21):14617-23.

49. Muresan V, Godek CP, Reese TS, Schnapp BJ. Plus-end motors override minus-end motors during transport of squid axon vesicles on microtubules. J Cell Biol. 1996 Oct;135(2):383-97.

50. Levi V, Serpinskaya AS, Gratton E, Gelfand V. Organelle transport along microtubules in Xenopus melanophores: evidence for cooperation between multiple motors. Biophys J. 2006 Jan 01,;90(1):318-27.

51. Blasius TL, Reed N, Slepchenko BM, Verhey KJ. Recycling of Kinesin-1 Motors by Diffusion after Transport. PLOS ONE. 2013 Sep 30,;8(9):e76081.

52. Lawrence CJ, Dawe RK, Christie KR, Cleveland DW, Dawson SC, Endow SA, et al. A standardized kinesin nomenclature. The Journal of Cell Biology. 2004 11 October;167(1):19.

53. Wong-Riley MTT, Besharse JC. The kinesin superfamily protein KIF17: one protein with many functions. Biomol Concepts. 2012 -6-1;3(3):267-82.

54. Muresan V, Abramson T, Lyass A, Winter D, Porro E, Hong F, et al. KIF3C and KIF3A form a novel neuronal heteromeric kinesin that associates with membrane vesicles. Mol Biol Cell. 1998 Mar;9(3):637-52.

55. Yamazaki H, Nakata T, Okada Y, Hirokawa N. KIF3A/B: a heterodimeric kinesin superfamily protein that works as a microtubule plus end-directed motor for membrane organelle transport. J Cell Biol. 1995 September;130(6):1387-99.

56. Yamazaki H, Nakata T, Okada Y, Hirokawa N. Cloning and characterization of KAP3: a novel kinesin superfamily-associated protein of KIF3A/3B. Proc Natl Acad Sci U S A. 1996 Aug 06,;93(16):8443-8.

57. Telikicherla D, Maharudraiah J, Pawar H, Marimuthu A, Kashyap MK, Ramachandra YL, et al. Overexpression of Kinesin Associated Protein 3 (KIFAP3) in Breast Cancer. Journal of proteomics & bioinformatics. 2012 May;5(5):122.

58. Shimizu K, Shirataki H, Honda T, Minami S, Takai Y. Complex formation of SMAP/KAP3, a KIF3A/B ATPase motor-associated protein, with a human chromosome-associated polypeptide. J Biol Chem. 1998 Mar 20,;273(12):6591-4.

59. Tewari R, Bailes E, Bunting KA, Coates JC. Armadillo-repeat protein functions: questions for little creatures. Trends Cell Biol. 2010 Aug;20(8):470-81.

60. Zhang Y, Hancock WO. The two motor domains of KIF3A/B coordinate for processive motility and move at different speeds. Biophys J. 2004 Sep;87(3):1795-804.

61. Vashishtha M, Walther Z, Hall JL. The kinesin-homologous protein encoded by the Chlamydomonas FLA10 gene is associated with basal bodies and centrioles. J Cell Sci. 1996 Mar;109 (Pt 3):541-9.

62. Henson JH, Cole DG, Terasaki M, Rashid D, Scholey JM. Immunolocalization of the heterotrimeric kinesin-related protein KRP(85/95) in the mitotic apparatus of sea urchin embryos. Dev Biol. 1995 Sep;171(1):182-94.

63. Haraguchi K, Hayashi T, Jimbo T, Yamamoto T, Akiyama T. Role of the kinesin-2 family protein, KIF3, during mitosis. J Biol Chem. 2006 February 17,;281(7):4094-9.

64. Grant BD, Donaldson JG. Pathways and mechanisms of endocytic recycling. Nature reviews. Molecular cell biology. 2009 September;10(9):597.

65. Maxfield FR, McGraw TE. Endocytic recycling. Nat Rev Mol Cell Biol. 2004 Feb;5(2):121-32.

66. Huotari J, Helenius A. Endosome maturation. EMBO J. 2011 Aug 31,;30(17):3481-500.

67. Imamura T, Huang J, Usui I, Satoh H, Bever J, Olefsky JM. Insulin-induced GLUT4 translocation involves protein kinase C-lambda-mediated functional coupling between Rab4 and the motor protein kinesin. Mol Cell Biol. 2003 Jul;23(14):4892-900.

68. Stenmark H, Olkkonen VM. The Rab GTPase family. Genome Biol. 2001;2(5):reviews3007.7.

69. Brown CL, Maier KC, Stauber T, Ginkel LM, Wordeman L, Vernos I, et al. Kinesin-2 is a motor for late endosomes and lysosomes. Traffic. 2005 Dec;6(12):1114-24.

70. Schonteich E, Wilson GM, Burden J, Hopkins CR, Anderson K, Goldenring JR, et al. The Rip11/Rab11-FIP5 and kinesin II complex regulates endocytic protein recycling. J Cell Sci. 2008 Nov 15,;121(Pt 22):3824-33.

71. Stauber T, Simpson JC, Pepperkok R, Vernos I. A role for kinesin-2 in COPI-dependent recycling between the ER and the Golgi complex. Curr Biol. 2006 Nov 21,;16(22):2245-51.

72. Ou G, Blacque OE, Snow JJ, Leroux MR, Scholey JM. Functional coordination of intraflagellar transport motors. Nature. 2005 Jul 28,;436(7050):583-7.

73. Cole DG, Diener DR, Himelblau AL, Beech PL, Fuster JC, Rosenbaum JL. Chlamydomonas kinesin-II-dependent intraflagellar transport (IFT): IFT particles contain proteins required for ciliary assembly in Caenorhabditis elegans sensory neurons. J Cell Biol. 1998 May 18,;141(4):993-1008.

74. Nonaka S, Tanaka Y, Okada Y, Takeda S, Harada A, Kanai Y, et al. Randomization of Left–Right Asymmetry due to Loss of Nodal Cilia Generating Leftward Flow of Extraembryonic Fluid in Mice Lacking KIF3B Motor Protein. Cell. 1998 December 11,;95(6):829-37.

75. Hirokawa N, Tanaka Y, Okada Y, Takeda S. Nodal flow and the generation of left-right asymmetry. Cell. 2006 Apr 07,;125(1):33-45.

76. Kurosaka S, Kashina A. Cell Biology of Embryonic Migration. Birth Defects Res C Embryo Today. 2008 -6;84(2):102-22.

77. Alwes F, Hinchen B, Extavour CG. Patterns of cell lineage, movement, and migration from germ layer specification to gastrulation in the amphipod crustacean Parhyale hawaiensis. Dev Biol. 2011 Nov 01,;359(1):110-23.

78. Shah JMY, Omar E, Pai DR, Sood S. Cellular events and biomarkers of wound healing. Indian J Plast Surg. 2012 May;45(2):220-8.

79. Luster AD, Alon R, von Andrian UH. Immune cell migration in inflammation: present and future therapeutic targets. Nat Immunol. 2005 Dec;6(12):1182-90.

80. Friedl P, Wolf K. Tumour-cell invasion and migration: diversity and escape mechanisms. Nat Rev Cancer. 2003 May;3(5):362-74.

81. Thiery JP. Epithelial-mesenchymal transitions in tumour progression. Nat Rev Cancer. 2002 Jun;2(6):442-54.

82. Ota I, Li X, Hu Y, Weiss SJ. Induction of a MT1-MMP and MT2-MMP-dependent basement membrane transmigration program in cancer cells by Snail1. Proc Natl Acad Sci U S A. 2009 Dec 01,;106(48):20318-23.

83. Thiery JP, Sleeman JP. Complex networks orchestrate epithelial-mesenchymal transitions. Nat Rev Mol Cell Biol. 2006 Feb;7(2):131-42.

84. Nabeshima K, Inoue T, Shimao Y, Sameshima T. Matrix metalloproteinases in tumor invasion: role for cell migration. Pathol Int. 2002 Apr;52(4):255-64.

85. Paňková K, Rösel D, Novotný M, Brábek J. The molecular mechanisms of transition between mesenchymal and amoeboid invasiveness in tumor cells. Cell Mol Life Sci. 2010 -1;67(1):63-71.

86. Wolf K, Mazo I, Leung H, Engelke K, von Andrian UH, Deryugina EI, et al. Compensation mechanism in tumor cell migration: mesenchymal-amoeboid transition after blocking of pericellular proteolysis. J Cell Biol. 2003 Jan 20,;160(2):267-77.

87. Sabeh F, Shimizu-Hirota R, Weiss SJ. Protease-dependent versus -independent cancer cell invasion programs: three-dimensional amoeboid movement revisited. J Cell Biol. 2009 Apr 06,;185(1):11-9.

88. Hynes RO. Integrins: bidirectional, allosteric signaling machines. Cell. 2002 Sep 20,;110(6):673-87.

89. Plow EF, Haas TA, Zhang L, Loftus J, Smith JW. Ligand binding to integrins. J Biol Chem. 2000 Jul 21,;275(29):21785-8.

90. Geiger B, Spatz JP, Bershadsky AD. Environmental sensing through focal adhesions. Nat Rev Mol Cell Biol. 2009 Jan;10(1):21-33.

91. Parsons JT, Horwitz AR, Schwartz MA. Cell adhesion: integrating cytoskeletal dynamics and cellular tension. Nat Rev Mol Cell Biol. 2010 Sep;11(9):633-43.

92. Hotulainen P, Lappalainen P. Stress fibers are generated by two distinct actin assembly mechanisms in motile cells. J Cell Biol. 2006 May 08,;173(3):383-94.

93. Ridley AJ, Schwartz MA, Burridge K, Firtel RA, Ginsberg MH, Borisy G, et al. Cell migration: integrating signals from front to back. Science. 2003 Dec 05,;302(5651):1704-9.

94. Kim D, Wirtz D. Focal adhesion size uniquely predicts cell migration. FASEB J. 2013 April;27(4):1351-61.

95. Zaidel-Bar R, Geiger B. The switchable integrin adhesome. J Cell Sci. 2010 May 01,;123(Pt 9):1385-8.

96. Ezzell RM, Goldmann WH, Wang N, Parashurama N, Parasharama N, Ingber DE. Vinculin promotes cell spreading by mechanically coupling integrins to the cytoskeleton. Exp Cell Res. 1997 Feb 25,;231(1):14-26.

97. Critchley DR, Gingras AR. Talin at a glance. J Cell Sci. 2008 May 01,;121(Pt 9):1345-7.

98. Mierke CT, Kollmannsberger P, Zitterbart DP, Diez G, Koch TM, Marg S, et al. Vinculin facilitates cell invasion into three-dimensional collagen matrices. J Biol Chem. 2010 Apr 23,;285(17):13121-30.

99. Humphries JD, Wang P, Streuli C, Geiger B, Humphries MJ, Ballestrem C. Vinculin controls focal adhesion formation by direct interactions with talin and actin. J Cell Biol. 2007 -12-3;179(5):1043-57.

100. Theisen U, Straube E, Straube A. Directional persistence of migrating cells requires Kif1C-mediated stabilization of trailing adhesions. Dev Cell. 2012 Dec 11,;23(6):1153-66.

101. Rid R, Schiefermeier N, Grigoriev I, Small JV, Kaverina I. The last but not the least: the origin and significance of trailing adhesions in fibroblastic cells. Cell Motil Cytoskeleton. 2005 Jul;61(3):161-71.

102. Murphy DA, Courtneidge SA. The 'ins' and 'outs' of podosomes and invadopodia: characteristics, formation and function. Nat Rev Mol Cell Biol. 2011 Jun 23,;12(7):413-26.

103. Gimona M, Buccione R, Courtneidge SA, Linder S. Assembly and biological role of podosomes and invadopodia. Curr Opin Cell Biol. 2008 Apr;20(2):235-41.

104. Linder S, Hüfner K, Wintergerst U, Aepfelbacher M. Microtubule-dependent formation of podosomal adhesion structures in primary human macrophages. J Cell Sci. 2000 Dec;113 Pt 23:4165-76.

105. Linder S, Aepfelbacher M. Podosomes: adhesion hot-spots of invasive cells. Trends Cell Biol. 2003 Jul;13(7):376-85.

106. Weaver AM. Invadopodia. Curr Biol. 2008 May 06,;18(9):362.

107. Hoshino D, Branch KM, Weaver AM. Signaling inputs to invadopodia and podosomes. J Cell Sci. 2013 Jul 15,;126(Pt 14):2979-89.

108. Lock P, Abram CL, Gibson T, Courtneidge SA. A new method for isolating tyrosine kinase substrates used to identify fish, an SH3 and PX domain-containing protein, and Src substrate. EMBO J. 1998 Aug 03,;17(15):4346-57.

109. Crimaldi L, Courtneidge SA, Gimona M. Tks5 recruits AFAP-110, p190RhoGAP, and cortactin for podosome formation. Exp Cell Res. 2009 Sep 10,;315(15):2581-92.

110. Tehrani S, Tomasevic N, Weed S, Sakowicz R, Cooper JA. Src phosphorylation of cortactin enhances actin assembly. Proc Natl Acad Sci U S A. 2007 Jul 17,;104(29):11933-8.

111. Oser M, Yamaguchi H, Mader CC, Bravo-Cordero JJ, Arias M, Chen X, et al. Cortactin regulates cofilin and N-WASp activities to control the stages of invadopodium assembly and maturation. The Journal of Cell Biology. 2009 24 August;186(4):571.

112. Millard TH, Sharp SJ, Machesky LM. Signalling to actin assembly via the WASP (Wiskott-Aldrich syndrome protein)-family proteins and the Arp2/3 complex. Biochem J. 2004 May 15,;380(Pt 1):1-17.

113. Buschman MD, Bromann PA, Cejudo-Martin P, Wen F, Pass I, Courtneidge SA. The novel adaptor protein Tks4 (SH3PXD2B) is required for functional podosome formation. Mol Biol Cell. 2009 Mar;20(5):1302-11.

114. Zaidel-Bar R, Ballestrem C, Kam Z, Geiger B. Early molecular events in the assembly of matrix adhesions at the leading edge of migrating cells. J Cell Sci. 2003 Nov 15,;116(Pt 22):4605-13.

115. Abram CL, Seals DF, Pass I, Salinsky D, Maurer L, Roth TM, et al. The adaptor protein fish associates with members of the ADAMs family and localizes to podosomes of Src-transformed cells. J Biol Chem. 2003 May 09,;278(19):16844-51.

116. Seals DF, Azucena EF, Pass I, Tesfay L, Gordon R, Woodrow M, et al. The adaptor protein Tks5/Fish is required for podosome formation and function, and for the protease-driven invasion of cancer cells. Cancer Cell. 2005 Feb;7(2):155-65.

117. Chen WT. Proteolytic activity of specialized surface protrusions formed at rosette contact sites of transformed cells. J Exp Zool. 1989 Aug;251(2):167-85.

118. Lohmer LL, Kelley LC, Hagedorn EJ, Sherwood DR. Invadopodia and basement membrane invasion in vivo. Cell Adh Migr. 2014 -5-01;8(3):246-55.

119. Gligorijevic B, Wyckoff J, Yamaguchi H, Wang Y, Roussos ET, Condeelis J. N-WASP-mediated invadopodium formation is involved in intravasation and lung metastasis of mammary tumors. J Cell Sci. 2012 Feb 01,;125(Pt 3):724-34.

120. Leong HS, Robertson AE, Stoletov K, Leith SJ, Chin CA, Chien AE, et al. Invadopodia are required for cancer cell extravasation and are a therapeutic target for metastasis. Cell Rep. 2014 September 11,;8(5):1558-70.

121. Oda K. New families of carboxyl peptidases: serine-carboxyl peptidases and glutamic peptidases. J Biochem. 2012 01/01/;151(1):13-25.

122. Rawlings ND, Barrett AJ. Evolutionary families of metallopeptidases. In: Enzymology, BT - Methods in, editor. Academic Press; 1995. p. 183-228.

123. Contents EC 3.4 to EC 3.12 [Internet].; 2016 [cited 2016 Nov 27]. Available from: http://www.chem.qmul.ac.uk/iubmb/enzyme/EC3/cont3bb.html.

124. Fanjul-Fernández M, Folgueras AR, Cabrera S, López-Otín C. Matrix metalloproteinases: Evolution, gene regulation and functional analysis in mouse models. Biochimica et Biophysica Acta (BBA) - Molecular Cell Research. 2010 January;1803(1):3-19.

125. Jacob A, Prekeris R. The regulation of MMP targeting to invadopodia during cancer metastasis. Front Cell Dev Biol. 2015 -2-02;3.

126. Poincloux R, Lizárraga F, Chavrier P. Matrix invasion by tumour cells: a focus on MT1-MMP trafficking to invadopodia. J Cell Sci. 2009 Sep 01,;122(Pt 17):3015-24.

127. Hotary K, Li X, Allen E, Stevens SL, Weiss SJ. A cancer cell metalloprotease triad regulates the basement membrane transmigration program. Genes Dev. 2006 10/01/;20(19):2673-86.

128. Overall CM, Dean RA. Degradomics: systems biology of the protease web. Pleiotropic roles of MMPs in cancer. Cancer Metastasis Rev. 2006 Mar;25(1):69-75.

129. Butler GS, Butler MJ, Atkinson SJ, Will H, Tamura T, Westrum SSv, et al. The TIMP2 Membrane Type 1 Metalloproteinase "Receptor" Regulates the Concentration and Efficient Activation of Progelatinase A A KINETIC STUDY. J Biol Chem. 1998 01/09/;273(2):871-80.

130. Toth M, Chvyrkova I, Bernardo MM, Hernandez-Barrantes S, Fridman R. Pro-MMP-9 activation by the MT1-MMP/MMP-2 axis and MMP-3: role of TIMP-2 and plasma membranes. Biochem Biophys Res Commun. 2003 Aug 22,;308(2):386-95.

131. Remacle A, Murphy G, Roghi C. Membrane type I-matrix metalloproteinase (MT1-MMP) is internalised by two different pathways and is recycled to the cell surface. J Cell Sci. 2003 Oct 01,;116(Pt 19):3905-16.

132. Lafleur MA, Mercuri FA, Ruangpanit N, Seiki M, Sato H, Thompson EW. Type I collagen abrogates the clathrin-mediated internalization of membrane type 1 matrix metalloproteinase (MT1-MMP) via the MT1-MMP hemopexin domain. J Biol Chem. 2006 Mar 10,;281(10):6826-40.

133. Alexander NR, Branch KM, Parekh A, Clark ES, Iwueke IC, Guelcher SA, et al. Extracellular matrix rigidity promotes invadopodia activity. Curr Biol. 2008 Sep 09,;18(17):1295-9.

134. Annabi B, Lachambre M, Bousquet-Gagnon N, Pagé M, Gingras D, Béliveau R. Localization of membrane-type 1 matrix metalloproteinase in caveolae membrane domains. Biochem J. 2001 Feb 01,;353(Pt 3):547-53.

135. Bravo-Cordero JJ, Marrero-Diaz R, Megías D, Genís L, García-Grande A, García MA, et al. MT1-MMP proinvasive activity is regulated by a novel Rab8-dependent exocytic pathway. EMBO J. 2007 Mar 21,;26(6):1499-510.

136. Wang X, Ma D, Keski-Oja J, Pei D. Co-recycling of MT1-MMP and MT3-MMP through the trans-Golgi network. Identification of DKV582 as a recycling signal. J Biol Chem. 2004 Mar 05,;279(10):9331-6.

137. Sakurai-Yageta M, Recchi C, Le Dez G, Sibarita J, Daviet L, Camonis J, et al. The interaction of IQGAP1 with the exocyst complex is required for tumor cell invasion downstream of Cdc42 and RhoA. J Cell Biol. 2008 Jun 16,;181(6):985-98.

138. Steffen A, Le Dez G, Poincloux R, Recchi C, Nassoy P, Rottner K, et al. MT1-MMP-dependent invasion is regulated by TI-VAMP/VAMP7. Curr Biol. 2008 Jun 24,;18(12):926-31.

139. Wiesner C, Faix J, Himmel M, Bentzien F, Linder S. KIF5B and KIF3A/KIF3B kinesins drive MT1-MMP surface exposure, CD44 shedding, and extracellular matrix degradation in primary macrophages. Blood. 2010 Sep 02,;116(9):1559-69.

140. Whitehead KA, Langer R, Anderson DG. Knocking down barriers: advances in siRNA delivery. Nat Rev Drug Discov. 2009 February;8(2):129-38.

141. Esteller M. Non-coding RNAs in human disease. Nat Rev Genet. 2011 Nov 18,;12(12):861-74.

142. Winter J, Jung S, Keller S, Gregory RI, Diederichs S. Many roads to maturity: microRNA biogenesis pathways and their regulation. Nat Cell Biol. 2009 Mar;11(3):228-34.

143. Lee Y, Kim M, Han J, Yeom K, Lee S, Baek SH, et al. MicroRNA genes are transcribed by RNA polymerase II. EMBO J. 2004 Oct 13,;23(20):4051-60.

144. Borchert GM, Lanier W, Davidson BL. RNA polymerase III transcribes human microRNAs. Nat Struct Mol Biol. 2006 Dec;13(12):1097-101.

145. Denli AM, Tops BBJ, Plasterk RHA, Ketting RF, Hannon GJ. Processing of primary microRNAs by the Microprocessor complex. Nature. 2004 Nov 11,;432(7014):231-5.

146. Yi R, Qin Y, Macara IG, Cullen BR. Exportin-5 mediates the nuclear export of pre-microRNAs and short hairpin RNAs. Genes Dev. 2003 Dec 15,;17(24):3011-6.

147. Haase AD, Jaskiewicz L, Zhang H, Lainé S, Sack R, Gatignol A, et al. TRBP, a regulator of cellular PKR and HIV-1 virus expression, interacts with Dicer and functions in RNA silencing. EMBO Rep. 2005 Oct;6(10):961-7.

148. Hutvágner G, McLachlan J, Pasquinelli AE, Bálint E, Tuschl T, Zamore PD. A cellular function for the RNA-interference enzyme Dicer in the maturation of the let-7 small temporal RNA. Science. 2001 Aug 03,;293(5531):834-8.

149. Matranga C, Tomari Y, Shin C, Bartel DP, Zamore PD. Passenger-strand cleavage facilitates assembly of siRNA into Ago2-containing RNAi enzyme complexes. Cell. 2005 Nov 18,;123(4):607-20.

150. Schwarz DS, Hutvágner G, Du T, Xu Z, Aronin N, Zamore PD. Asymmetry in the assembly of the RNAi enzyme complex. Cell. 2003 Oct 17,;115(2):199-208.

151. Fakhr E, Zare F, Teimoori-Toolabi L. Precise and efficient siRNA design: a key point in competent gene silencing. Cancer Gene Ther. 2016 Apr;23(4):73-82.

152. Lam JKW, Chow MYT, Zhang Y, Leung SWS. siRNA Versus miRNA as Therapeutics for Gene Silencing. Mol Ther Nucleic Acids. 2015 Sep 15,;4:e252.

153. Elbashir SM, Lendeckel W, Tuschl T. RNA interference is mediated by 21- and 22-nucleotide RNAs. Genes Dev. 2001 Jan 15,;15(2):188-200.

154. Valencia-Sanchez MA, Liu J, Hannon GJ, Parker R. Control of translation and mRNA degradation by miRNAs and siRNAs. Genes Dev. 2006 Mar 01,;20(5):515-24.

155. Lewis BP, Shih I-, Jones-Rhoades MW, Bartel DP, Burge CB. Prediction of mammalian microRNA targets. Cell. 2003 Dec 26,;115(7):787-98.

156. Huntzinger E, Izaurralde E. Gene silencing by microRNAs: contributions of translational repression and mRNA decay. Nat Rev Genet. 2011 Feb;12(2):99-110.

157. Kim VN, Han J, Siomi MC. Biogenesis of small RNAs in animals. Nat Rev Mol Cell Biol. 2009 Feb;10(2):126-39.

158. Pasquinelli AE. MicroRNAs and their targets: recognition, regulation and an emerging reciprocal relationship. Nat Rev Genet. 2012 Mar 13,;13(4):271-82.

159. Daka A, Peer D. RNAi-based nanomedicines for targeted personalized therapy. Adv Drug Deliv Rev. 2012 Oct;64(13):1508-21.

160. Xu C, Wang J. Delivery systems for siRNA drug development in cancer therapy. Asian Journal of Pharmaceutical Sciences. 2015 February;10(1):1-12.

161. Kanasty R, Dorkin JR, Vegas A, Anderson D. Delivery materials for siRNA therapeutics. Nat Mater. 2013 November;12(11):967-77.

162. Couto LB, High KA. Viral vector-mediated RNA interference. Curr Opin Pharmacol. 2010 Oct;10(5):534-42.

163. Höbel S, Aigner A. Polyethylenimines for siRNA and miRNA delivery in vivo. Wiley Interdiscip Rev Nanomed Nanobiotechnol. 2013 Sep-Oct;5(5):484-501.

164. Makadia HK, Siegel SJ. Poly Lactic-co-Glycolic Acid (PLGA) as Biodegradable Controlled Drug Delivery Carrier. Polymers (Basel). 2011 -9-1;3(3):1377-97.

165. Yin H, Kanasty RL, Eltoukhy AA, Vegas AJ, Dorkin JR, Anderson DG. Non-viral vectors for gene-based therapy. Nat Rev Genet. 2014 Aug;15(8):541-55.

166. Corcoran JA, Duncan R. Reptilian reovirus utilizes a small type III protein with an external myristylated amino terminus to mediate cell-cell fusion. J Virol. 2004 Apr;78(8):4342-51.

167. Top D, de Antueno R, Salsman J, Corcoran J, Mader J, Hoskin D, et al. Liposome reconstitution of a minimal protein-mediated membrane fusion machine. EMBO J. 2005 Sep 07,;24(17):2980-8.

168. Ciechonska M, Duncan R. Reovirus FAST proteins: virus-encoded cellular fusogens. Trends Microbiol. 2014 Dec;22(12):715-24.

169. Markwalder R, Reubi JC. Gastrin-releasing peptide receptors in the human prostate: relation to neoplastic transformation. Cancer Res. 1999 Mar 01,;59(5):1152-9.

170. Scherman D, Rousseau A, Bigey P, Escriou V. Genetic pharmacology: progresses in siRNA delivery and therapeutic applications. Gene Ther. 2017 Feb 16,.

171. Hicklin DJ, Ellis LM. Role of the vascular endothelial growth factor pathway in tumor growth and angiogenesis. J Clin Oncol. 2005 Feb 10,;23(5):1011-27.

172. Tao W, South VJ, Zhang Y, Davide JP, Farrell L, Kohl NE, et al. Induction of apoptosis by an inhibitor of the mitotic kinesin KSP requires both activation of the spindle assembly checkpoint and mitotic slippage. Cancer Cell. 2005 Jul;8(1):49-59.

173. Tabernero J, Shapiro GI, LoRusso PM, Cervantes A, Schwartz GK, Weiss GJ, et al. First-in-humans trial of an RNA interference therapeutic targeting VEGF and KSP in cancer patients with liver involvement. Cancer Discov. 2013 Apr;3(4):406-17.

174. Schultheis B, Strumberg D, Santel A, Vank C, Gebhardt F, Keil O, et al. First-in-human phase I study of the liposomal RNA interference therapeutic Atu027 in patients with advanced solid tumors. J Clin Oncol. 2014 Dec 20,;32(36):4141-8.

175. Stoletov K, Bond D, Hebron K, Raha S, Zijlstra A, Lewis JD. Metastasis as a therapeutic target in prostate cancer: a conceptual framework. Am J Clin Exp Urol. 2014 Apr;2(1):45-56.

176. Immunofluorescence General Protocol [Internet]. [cited 2014 Oct 21]. Available from: https://www.cellsignal.com/contents/resources-protocols/immunofluorescence-general-protocol/if.

177. Introduction to sample preparation: immunofluorescence [Internet]. [cited 2014 Oct 21]. Available from: http://microscopy.duke.edu/sampleprep/if.html.

178. Artym VV, Yamada KM, Mueller SC. ECM degradation assays for analyzing local cell invasion. Methods Mol Biol. 2009;522:211-9.

179. Kim YJ. Computational siRNA design considering alternative splicing. Methods Mol Biol. 2010;623:81-92.

180. Shalem O, Sanjana NE, Hartenian E, Shi X, Scott DA, Mikkelsen TS, et al. Genome-scale CRISPR-Cas9 knockout screening in human cells. Science. 2014 Jan 3,;343(6166):84-7.

181. Doench JG, Fusi N, Sullender M, Hegde M, Vaimberg EW, Donovan KF, et al. Optimized sgRNA design to maximize activity and minimize off-target effects of CRISPR-Cas9. Nat Biotechnol. 2016 Feb;34(2):184-91.

182. Ran FA, Hsu PD, Wright J, Agarwala V, Scott DA, Zhang F. Genome engineering using the CRISPR-Cas9 system. Nat Protoc. 2013 November;8(11):2281-308.

183. Friedl P, Wolf K. Tumour-cell invasion and migration: diversity and escape mechanisms. Nat Rev Cancer. 2003 May;3(5):362-74.

184. Chao W, Kunz J. Focal adhesion disassembly requires clathrin-dependent endocytosis of integrins. FEBS Lett. 2009 April 17,;583(8):1337-43.

185. Sabeh F, Shimizu-Hirota R, Weiss SJ. Protease-dependent versus -independent cancer cell invasion programs: three-dimensional amoeboid movement revisited. J Cell Biol. 2009 April 6,;185(1):11-9.

186. d'Ortho MP, Stanton H, Butler M, Atkinson SJ, Murphy G, Hembry RM. MT1-MMP on the cell surface causes focal degradation of gelatin films. FEBS Lett. 1998 Jan 9,;421(2):159-64.

187. Droplet Digital PCR applications guide [Internet]. [cited 2016 May]. Available from: http://www.bio-rad.com/webroot/web/pdf/lsr/literature/Bulletin_6407.pdf.

188. Baker M. Digital PCR hits its stride. Nat Meth. 2012 June;9(6):541-4.

189. Schaffner F, Ray AM, Dontenwill M. Integrin α5β1, the Fibronectin Receptor, as a Pertinent Therapeutic Target in Solid Tumors. Cancers (Basel). 2013 -1-15;5(1):27-47.

190. Kramer N, Walzl A, Unger C, Rosner M, Krupitza G, Hengstschläger M, et al. In vitro cell migration and invasion assays. Mutat Res. 2013 Jan-Mar;752(1):10-24.

191. Chen MB, Lamar JM, Li R, Hynes RO, Kamm RD. Elucidation of the Roles of Tumor Integrin β1 in the Extravasation Stage of the Metastasis Cascade. Cancer Res. 2016 May 01,;76(9):2513-24.

192. TrypLE Reagents [Internet]. [cited Mar 2017]. Available from: https://www.thermofisher.com/ca/en/home/life-science/cell-culture/mammalian-cell-culture/reagents/trypsin/tryple-express.html.

193. Kuonen F, Touvrey C, Laurent J, Ruegg C. Fc block treatment, dead cells exclusion, and cell aggregates discrimination concur to prevent phenotypical artifacts in the analysis of subpopulations of tumor-infiltrating CD11b(+) myelomonocytic cells. Cytometry A. 2010 Nov;77(11):1082-90.

194. Caldwell CW. Preservation of B-cell-associated surface antigens by chemical fixation. Cytometry. 1994 Jul 01,;16(3):243-9.

195. Eisenach PA, de Sampaio PC, Murphy G, Roghi C. Membrane Type 1 Matrix Metalloproteinase (MT1-MMP) Ubiquitination at Lys581 Increases Cellular Invasion through Type I Collagen. J Biol Chem. 2012 -3-30;287(14):11533-45.

196. Takeda S, Yonekawa Y, Tanaka Y, Okada Y, Nonaka S, Hirokawa N. Left-right asymmetry and kinesin superfamily protein KIF3A: new insights in determination of laterality and mesoderm induction by kif3A-/- mice analysis. J Cell Biol. 1999 May 17,;145(4):825-36.

197. Keil R, Kiessling C, Hatzfeld M. Targeting of p0071 to the midbody depends on KIF3. J Cell Sci. 2009 Apr 15,;122(Pt 8):1174-83.

198. O'Connor K, Chen M. Dynamic functions of RhoA in tumor cell migration and invasion. Small GTPases. 2013 -7-01;4(3):141-7.

199. Robertson AE. Elucidation of key mediators of tumour cell migration using an in vivo inhibitory RNA screen [dissertation]. University of Western Ontario; 2011.

200. Chien AJ, Conrad WH, Moon RT. A Wnt survival guide: from flies to human disease. J Invest Dermatol. 2009 Jul;129(7):1614-27.

201. Jiang Y, Luo Y, He D, Li X, Zhang L, Peng T, et al. Role of Wnt/beta-catenin signaling pathway in epithelial-mesenchymal transition of human prostate cancer induced by hypoxia-inducible factor-1alpha. Int J Urol. 2007 Nov;14(11):1034-9.

202. Jimbo T, Kawasaki Y, Koyama R, Sato R, Takada S, Haraguchi K, et al. Identification of a link between the tumour suppressor APC and the kinesin superfamily. Nat Cell Biol. 2002 Apr;4(4):323-7.

203. Liu Z, Rebowe RE, Wang Z, Li Y, Wang Z, DePaolo JS, et al. KIF3a promotes proliferation and invasion via Wnt signaling in advanced prostate cancer. Mol Cancer Res. 2014 Apr;12(4):491-503.

204. Barolo S. Transgenic Wnt/TCF pathway reporters: all you need is Lef? Oncogene. 2006 Dec 04,;25(57):7505-11.

205. Elia G. Biotinylation reagents for the study of cell surface proteins. Proteomics. 2008 Oct;8(19):4012-24.

Appendices
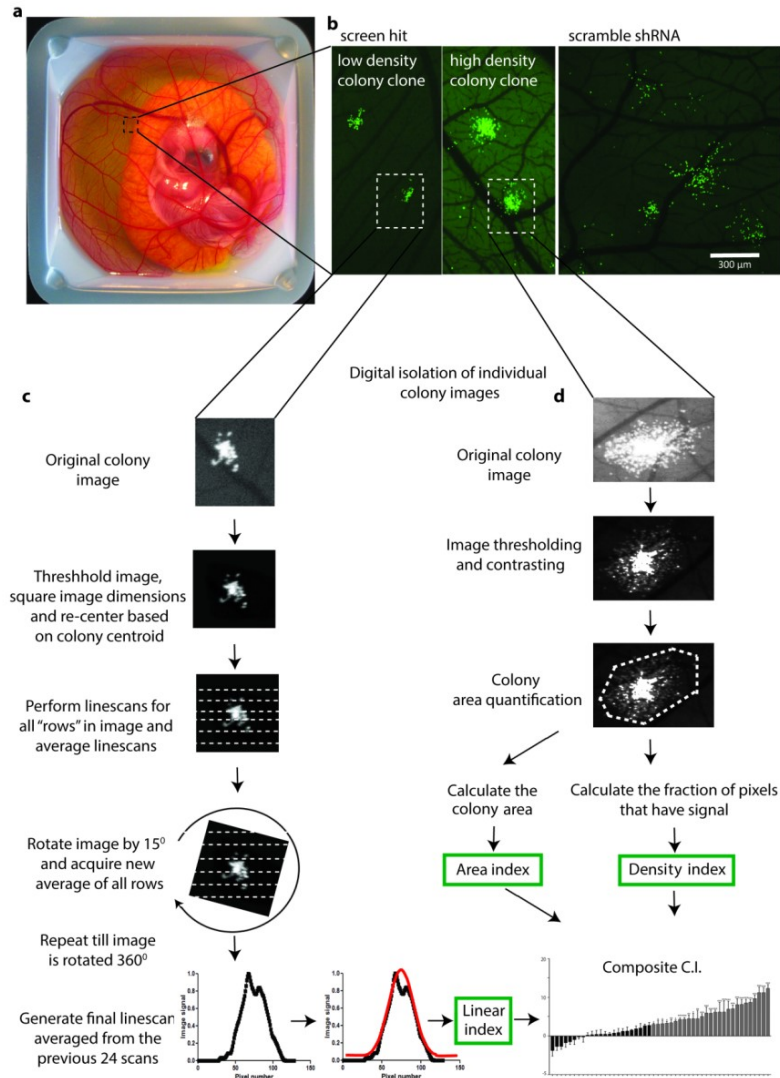
Appendix A. Quantitative avian embryo *in vivo* screening platform
(A) Avian embryo, 16 days post fertilization, in *ex ovo* culture. (B) Representative images of metastatic colonies arising from single cancer cells, 6 days after intravenous injection. Left panel shows a colony derived from one of the screen hits (shSRPK1), right panel shows control, scramble shRNA transduced HEp3 colonies. (C) Schematic of the Linear Index metastatic colony compactness quantification approach. (D) Schematic of the Area and Density Index metastatic colony compactness quantification approaches. These three measures are combined for each screen hit to generate a composite compactness Index (C.I.).

Appendix B. Primers and probes for droplet digital PCR analysis of CRISPR-Cas9 editing by pKIF3Bsg2

Forward primer	5'- GAA CCA TTT TTG CCT ATG G -3'
Reverse primer	5'- CCT CCT GGT AGA TCT CTA AG -3'
Drop-off	5'- /5HEX/AAG GAA TCC /ZEN/ GTG GTG AC/3IABkFQ/ -3'
Reference probe	5'- /56-FAM/ATT GTT GAT /ZEN/TCT GGG ATC GAG A/3IABkFQ/ -3'
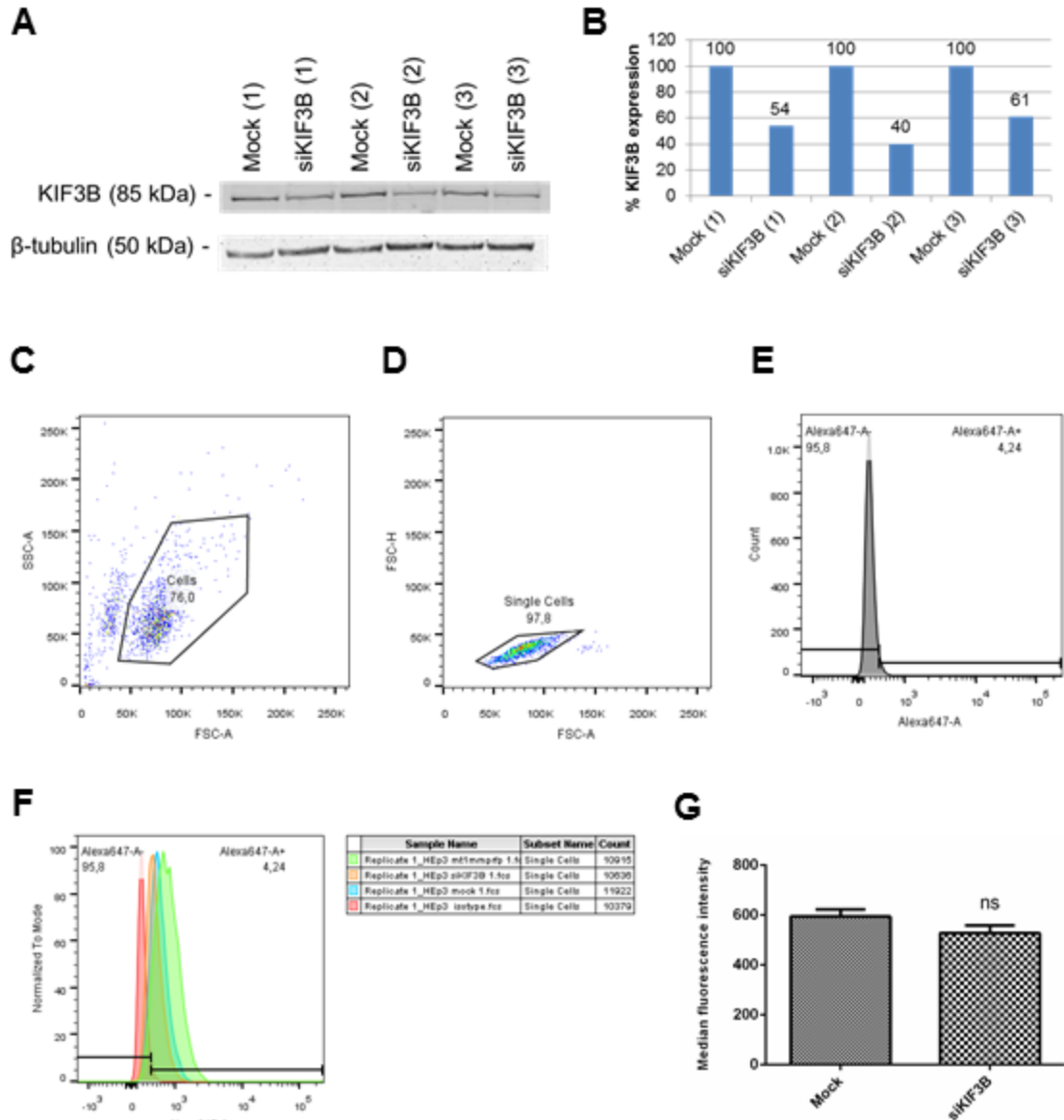
Appendix C. KIF3B knockdown by siRNA does not reduce cell surface localization of MT1-MMP in HEp3 cells

(A, B) Western blot and quantifications of KIF3B knockdown in HEp3 cells used for the assay. (C-E) Gating for single cells was completed using unstained cells and PMT voltage was determined using cells stained with isotype control antibody. 10,000 single cell events were recorded per group. (F) Histogram of counts versus fluorescence intensity for MT1-MMP staining. (G) Compared to mock transfected cells, KIF3B knockdown did not reduce the median fluorescence intensity for MT1-MMP staining. p>0.05, two-tailed t-test of mean±SD. 2 independent experiments were completed with data from a single representative experiment shown.
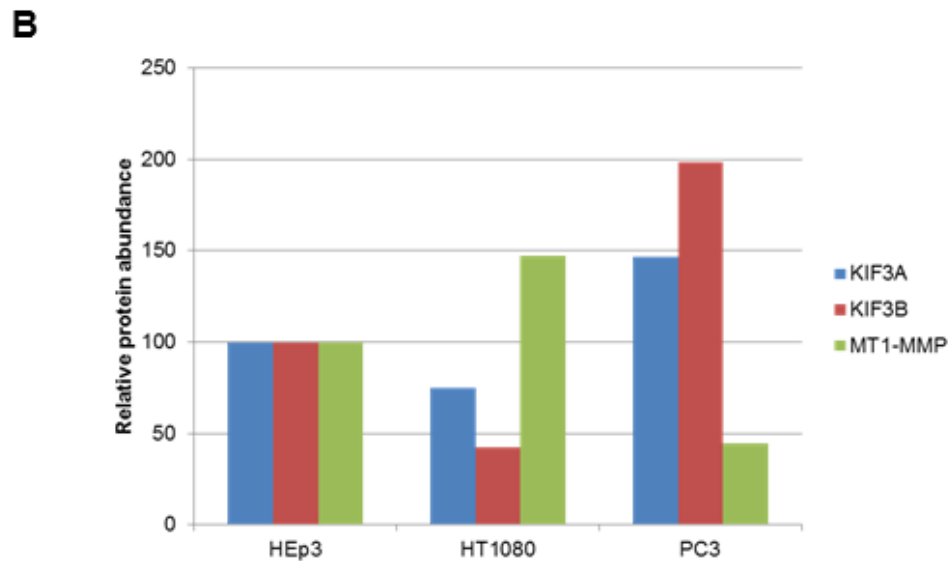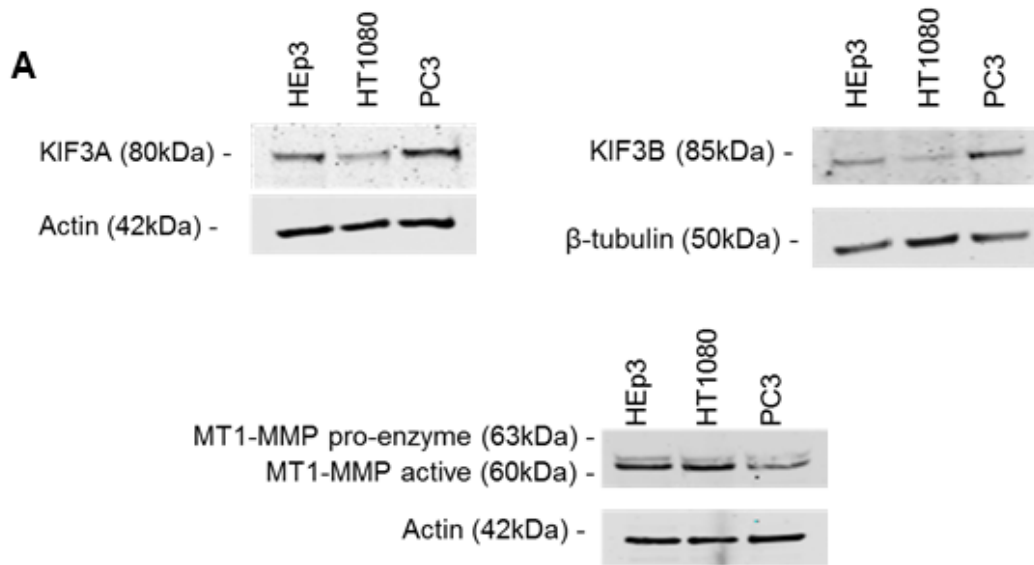
Appendix D. Relative expression of KIF3A, KIF3B, and MT1-MMP in HEp3, HT1080 and PC3 cancer cell lines
(A) The expression of KIF3A, KIF3B and MT1-MMP was tested in HEp3 human epidermoid carcinoma, HT1080 human fibrosarcoma, and PC3 human prostate adenocarcinoma cell lines. Protein lysates were collected from cells in the exponential phase of growth and 10µg of protein were electrophoresed per cell line. (B) Relative expression of KIF3A, KIF3B, and MT1-MMP are normalized to expression levels in HEp3 cells. The relative expression of MT1-MMP was quantified from the combination of the pro-enzyme and active enzyme bands. Data are from one experiment.